

FABRICATION AND CHARACTERIZATION OF NANOMETER-SIZED METAL AND
SEMICONDUCTOR PARTICLES AND NANOMETER-SIZED COMPOSITES

By

TUO LI

A DISSERTATION PRESENTED TO THE GRADUATE SCHOOL
OF THE UNIVERSITY OF FLORIDA IN PARTIAL FULFILLMENT
OF THE REQUIREMENTS FOR THE DEGREE OF
DOCTOR OF PHILOSOPHY

UNIVERSITY OF FLORIDA

1996

Dedicated to:

my family

in appreciation of their patience, support and encouragement

ACKNOWLEDGMENTS

First of all, I would like to express the most sincere thanks to my advisor, Dr. James H. Adair, for his guidance, encouragement, and constructive criticism throughout my research, and making me become a hands-on engineer. The experience of working with him has been rewarding in many ways. Secondly, I would like to express my gratitude to Drs. Rolf Hummel, Stephen Pearton, and Brij Moudgil of the Department of Materials Science and Engineering, and Dr. David Reitze of the Department of Physics for serving on my committee. I would further like to thank Dr Robert Park for willingness to serve as committee member substitute with short notice. Special thanks are directed to Drs. Matthias Ludwig, Joseph H. Simmons and Li Wang for their help with experiments and useful discussions.

I thank all of my colleagues in the Adair Research Group at the Department of Materials Science and Engineering. This work wouldn't be possible without their help. Special thanks are directed to Jooho Moon and Craig Habeger for research assistance. I sincerely acknowledge the help from Paul Demkowicz, Robert Sabia, Craig Habeger, and Henrik Krarup for the review of this manuscript. I am grateful to Drs. Stanley Bates and Augusto Morrone, the staff of the Major Analytical Instrumentation Center at the University of Florida, for their technical help and analytical support in the characterization of the specimens. I also would like to take this opportunity to thank Pam Howell for her administrative support and assistance in my research and Andrew Bender for assistance in operating the computer system. I would like to acknowledge NASA for partial financial support of this work (NASA Grant Number: NAG8-1244).

Finally, I want to thank my parents, my wife, and my daughter for their love, support, patience, and encouragement, which has always been a source of inspiration.

TABLE OF CONTENTS

ACKNOWLEDGMENTS	iii
LIST OF TABLES.....	vi
LIST OF FIGURES.....	vii
ABSTRACT.....	xiii
CHAPTERS	
1 INTRODUCTION	1
2 INTRODUCTION TO QUANTUM DOTS AND THEIR APPLICATIONS IN MICROELECTRONICS AND PHOTONICS	6
2.1. Overview	6
2.2. Applications and Potential Impacts	12
2.2.1. Examples in Microelectronics	12
2.2.2. Examples in Photonics.....	17
2.3. Quantum Structures and Atom Assemblies.....	24
2.3.1. Physical Approaching to Nanometer-Sized Structures.....	25
2.3.2. Chemical Approaching to Nanometer-sized Structures	27
2.3.2.1. Synthesis of nanosized clusters in organic and inorganic 3- dimensional hosts	29
2.3.2.2. Synthesis of nanometer-sized clusters on layer hosts.....	32
2.3.2.3. Synthesis of nanometer-sized clusters in open-frameworks.....	35
2.4. Future Development and Outlook	41
3 PREPARATION OF NANOMETER-SIZE ANISOTROPIC PARTICLES USING SELF-ASSEMBLY MOLECULES AS TEMPLATES.....	43
3.1. Introduction	43
3.2. Synthesis of CdS Platelets from Lamellar-Bilayer Templates.....	49
3.3. Results and Discussion	53
3.3.1. Characteristics of the CdS Platelets	53
3.3.2. Template Effects	62
3.3.3. Influence of the Metal Salt and Concentration on the Particle Formation and Morphology.....	66
3.3.4. Influence of the Other Processing Parameter on the Particle Foramtion	71
3.4. Conclusions	71

4	PREPARATION OF NANOMETER-SIZED CdS/OXIDE COMPOSITE PARTICLES USING REVERSE MICELLES IN CONJUNCTION WITH METAL ALKOXIDE HYDROLYSIS AND CONDENSATION	74
4.1.	Introduction	74
4.2.	Background	75
4.2.1.	General Remark	75
4.2.2.	Reverse Micelles as Microreactors.....	78
4.3.	Preparation of CdS/Oxides Spherical Nano-Composites	82
4.3.1.	Synthesis of CdS/SiO ₂ Nano-Composites	82
4.3.2.	Synthesis of CdS/TiO ₂ Nano-Composites	85
4.4.	Results and Discussion	88
4.4.1.	Nucleation and Growth of the Nanosize CdS Clusters	88
4.4.2.	Characteristics of the Resulting Particles	91
4.4.3.	Formation of the Nano-composites in Microemulsion Matrix.....	95
4.4.3.1.	Influence of the processing parameters	95
4.4.3.2.	Mechanism of the nano-composites formation	97
4.4.3.3.	Chemical modification of titanium alkoxide	102
4.4.5.	Optical Characterization and Size-Quantization Effects	104
4.5.	Conclusions	114
5	SYNTHESIS OF Ag/SiO ₂ NANOMETER-SIZED COMPOSITE PARTICLES	117
5.1.	Introduction	117
5.2.	Materials and Experiment	120
5.3.	Results and Discussion	123
5.3.1.	Formation of Ag colloids	123
5.3.1.1.	Effect of ratio of the water to surfactant on particle size.	123
5.3.1.2.	Effect of the reagent	124
5.3.1.3.	Effect of the solvent	128
5.3.2.	Formation of the Nano-composites.....	129
5.3.2.1.	Particle characteristics.....	129
5.3.2.2.	Mechanism of the nano-composite formation	136
5.4.	Conclusions	139
6	OPTICAL PROPERTIES OF NANO-COMPOSITE Ag/SiO ₂ PARTICLES	140
6.1.	Introduction	140
6.2.	General Treatment	141
6.3.	Linear and Nonlinear Optical Effects in Metal Clusters	145
6.3.1.	Surface Plasmon Mode and Linear Optical Properties	145
6.3.2.	Linear Absorption Optical Spectra of Ag and Ag/SiO ₂ Clusters	152
6.3.3.	Nonlinear Optical Properties of Ag/SiO ₂ Nano-Composites	155
6.3.3.1.	Local field enhancement and effective dielectric constant	156
6.3.3.2.	Degenerate four-wave mixing (DFWM).....	169
6.3.3.3.	Degenerate-four-wave mixing experiment	162
6.4.	Results and Discussions	166
6.5.	Conclusions	174

7 CONCLUSIONS AND SUGGESTIONS FOR FUTURE WORK	175
7.1. Overall Conclusions.....	175
7.2. Future Work.....	177
LIST OF REFERENCES.....	180
BIOGRAPHICAL SKETCH.....	187

LIST OF TABLES

<u>Table</u>	<u>page</u>
2-1. Approximate exciton binding energies, Bohr radii and other physical parameters for some selected bulk semiconductors.....	11
4-1. Comparison of size and excitonic transition energy	95
4-2. Product obtained according to the relative rates of hydrolysis and condensation..	103
6-1. Comparison of the experimental results with the theoretical calculations	173

LIST OF FIGURES

<u>Figure</u>	<u>page</u>
2-1. Quantum confinement in the ideal systems, evolution of the energy via density of states from bulk to zero dimension.	8
2-2. Band diagram of the InGaAs-In(AlGa)As resonant-tunneling hot-electron transistors (RHET).	13
2-3. Quantum Cascade lasers differ in a fundamental way from diode lasers . In quantum cascade laser, the wavelength, entirely determined by quantum confinement, can be tailored from the mid-infrared to the submillimeter wave region in the same heterostructure materials.	14
2-4. Illustration of possible operating principle of a quantum dots data register.....	17
2-5. Examples of anisotropic nonlinear filter serving as all-optical switching, directional coupler controlled by the optical Kerr effect.....	20
2-6. Quantum confinement effects on optical absorption. As the photon intensity I is increased, a small blue shift ($\lambda_1 \rightarrow \lambda_2$) is first observed that is due to photoinduced changes in the carrier concentrations . At saturation, only photons with wavelength λ_2 are absorbed	22
2-7. Nanophysics fabrication of a GaAs quantum dot array.....	26
2-8. Illustration of the interaction of the stabilizing media with Q-CdS clusters. (a) reverse micelle/hexametaphosphate-stabilized Q-CdS (b) p-[(Dimethylamino)methyl]-calix[6]arene-stabilized Q-CdS.....	28
2-9. The hyperlattice arrangement of CdS Clusters in adjacent solalite units of the zeolite Y. (hatched=Cd; open=S)	31
2-10. Use of Langmuir film containing functional groups to cause and control nucleation and growth of inorganic materials	34
2-11. The deal amphiphilic aggregates formed in amphiphilic system containing amphiphilic molecules-oil-water	36
2-12. Synthesis of nanoscale particles in reverse micelles; (a) Two microemulsions; (b) Microemulsion plus trigger; (c) Microemulsion plus second reactant	38
3-1. Phase structures for an ideal self-assembly system	47
3-2. Phase diagrams of lamellar bilayer structure: (a) partial pseudoternary phase diagram of SDS/AA-toluene-water ternary systems; and (b) octylamine-water binary system.....	51

3-3. Processing procedure used to synthesize CdS platelets in lamellar bilayer phase ..	52
3-4. Schematically illustrated amphiphilic bilayers acting as a template in the formation of anisotropically-shaped nanoscale inorganic particles	50
3-5. Micrographs of the neat phase bilayer (L2) phase in the SDS/AA-toluene-water system: (a) optical photomicrograph of the system under cross Polarizer; and (b) SEM micrograph of partially dried SA system.	54
3-6. TEM micrographs of CdS platelets prepared through lamellar bilayer phase: (a) CdS particles obtained from SDS/AA-toluene-aqueous system; and (b) CdS particles prepared from octylamine-aqueous system	55
3-7. TEM micrographs of CdS particles obtained from (a) conventional co-precipitation and (b) high salt concentration (0.1M)	57
3-8. Differential absorption spectra of CdS platelets as a function of weight ratio of water to surfactant, W. (a) W=0.8; (b) W=1.0; (c) W=1.2.....	59
3-9. XRD patterns of the precipitates: (a) before post treatment; (b) after post treatment; (c) conventional coprecipitation	60
3-10. TEM micrograph and diffraction pattern of CdS platelets.....	61
3-11. CdS particles resulting from the ternary system of SDS/AA-toluene-water, templating effect from organic ligand of amphiphilic molecule.....	64
3-12. Scheme of platelet formation inside lamellar bilayer structure	65
3-13. The effect of the starting materials on the formation of CdS particles: (a) CdS particles synthesized with CdCl ₂ as a starting materials in SDS/AA-toluene-water system; (b) CdS particles synthesized with CdCl ₂ as a starting materials in octylamine-water system.....	67
3-14. Concentration effects on the formation of platelet CdS in lamellar bilayer phase: (a) 0.02 M; (b) 0.05 M; (c) 0.005 M	69
3-15. Schematic illustration of the change of solution behavior of surfactant with the hydrophile and lipophile balance in water-surfactant-hydrocarbon system.	70
3-16. The effects of equilibration time of lamellar bilayer phase and aging time on the formation of CdS platelets: (a) the effect of phase equilibration time; and (b) the effect of aging time	72
4-1. Shape of surfactant molecules forming reverse micelles	78
4-2. (a) The ternary diagram for Aerosol OT-isooctane-water, T= 15 °, (b) quaternary diagram for sodium dodecylamine-toluene-water system	80
4-3. The dynamic process of microemulsion.....	81
4-4. Schematic diagram of the synthesis procedures used to prepare CdS/SiO ₂ nanocomposites	84

4-5. Schematic diagram of the synthesis procedure used to prepare CdS/TiO ₂ nano-composite and transparent monolithic gel.....	86
4-6. Schematic diagram of the modification procedure used for titanium isopropoxide.	87
4-7. Absorption spectra of CdS clusters prepared through two different synthesis routs in microemulsion matrix. (a) from temporal nucleation and growth; (b) from corprecipitation at ambient temperature.....	90
4-8. X-ray diffraction patterns of the CdS clusters, the revolution of the crystallinity as increase the cluster size.....	92
4-9. TEM micrograph and diffraction pattern of the CdS cluster prepared from microemulsion matrix.	93
4-10. A gallery of high resolution TEM (HRTEM) images of the CdS clusters having different size.....	94
4-11. (a) CdS/SiO ₂ nano-composites synthesized from nonionic surfactant system with R=4, H=100, and X=1. (b) XPS spectra of the nano-composites.....	96
4-12. Mechanisms of the particle formation in microemulsion reaction matrix: particle formation in reverse micelles	98
4-13. Scheme of the composite particle formation in microemulsion matrix.....	99
4-14. TEM microphotograph of the CdS/TiO ₂ nano-composite synthesized from Igepal-cyclohexane-water system with modified titanium isopropoxide precursors (R=5, H=200, X=1)	105
4-15. (a) Absorption spectra of CdS clusters having different sizes, and (b) Comparison of absorption spectra between CdS clusters and its nano-composites.....	106
4-16. (a) Schematic correlation diagram relating cluster states to bulk crystal states.(b) E(k) diagram: curve 1, case for parabolic band; curve 2, true energy band which is parabolic only near k=0; (●), two eigenvalues for the first excited state.	110
4-17. Partial band structure diagram of cubic crystalline CdS. The line labeled L(111) and X(100) refer to different dirctions within the unit cell.....	111
4-18. Size dependence of the first excitonic transition, compared the experimental results with the theoretical calculations.	113
4-19. Photoluminescence spectra of the CdS cluster and its nano-composites. (a) PL spectra as a function of the size, and (b) PL spectra at different temperature.....	115
5-1. Schematic diagram of the prodecude used to prepare nano-composite Ag/SiO ₂ ...122	
5-2. Absorption spectra of Ag clusters as a function of ratio of the water to surfactant, R.	125

5-3. TEM micrographs of Ag clusters synthesized through reverse micelles; (a) TEM micrographs of Ag clusters with $R=2$; and (b) diffraction pattern taken from the same sample	126
5-4. Absorption spectra of the Ag clusters: (a) at various Ag salt concentration, and (b) at various organic solvent.....	127
5-5. TEM micrographs of Ag/SiO ₂ nano-composites formed in Igepal-cyclohexane-water system at $R=4$, $X=1$, and various H ratios: (a) $H=100$; (b) $H=200$; and (c) $H=300$	130
5-6. Histogram of the Ag/SiO ₂ nano-composites synthesized at $R=4$, $X=1$, and different H: (a) $H=100$; (b) $H=200$; and (c) $H=300$	131
5-7. TEM micrographs of Ag/SiO ₂ nano-composites at the constant of $R=6$ and $X=0.75$, and different H: thickness: (a) $H=100$; (b) $H=200$; (c) $H=300$; (d) Diffraction pattern of the nano-composites.....	132
5-8. TEM micrographs of Ag/SiO ₂ nano-composites synthesized at the constant of $X=1$ and $H=100$, and different water content: (a) $R=2$; (b) $R=4$; (c) $R=6$; (d) $R=10$..	134
5-9. Variations of the size and thickness of Ag/SiO ₂ nano-composites as a function of R and H.....	135
5-10. Absorption spectra of Ag/SiO ₂ nano-composites synthesized at the constant of $X=1$ and $H=100$, and different R. (a) $R=4$; and (b) $R=8$; (c) relative rate hydrolysis at different R.	138
6-1. Linear absorption spectra of Ag clusters and their nano-composites: (a) Linear absorption spectra of Ag colloids, and (b) comparison of the Ag clusters with Ag/SiO ₂ nano-composites.	153
6-2. Ionic spheres with dielectric function embedded in a nonabsorbing medium with dielectric constant ϵ_i . The electric fields inside the spheres and in the nonabsorbing medium are denoted by E_i and E_m respectively.....	157
6-3. Wavevector diagrams of the mixing process $\omega_1+\omega_2\rightarrow\omega_3+\omega_4$; (a) nondegenerate case with phase-matching $\Delta k=0$ adjustable in the off-axis geometry (2); (b) partially degenerate four-wave mixing with automatic phase-matching in the one-beam (1) and two-beam (2) experiments, whereas in the four-beam geometry, $\Delta k=0$ has to be adjusted; (c) fully degenerate case, DFWM, with automatic phase-matching with pairwise counterpropagating (1) or co-propagating beams (2) for arbitrary beam intersection angle. Broken lines indicate the k-vectors of several induced (non-propagating) phase and/or amplitude gratings (from ref 151).....	161
6-4. Changes of surface-plasmon resonance frequency with the ratio of r_1/r_2	164
6-5. DFWM in the coarse-grating configuration. The symbols ● and - indicate vertical and horizontal polarization, respectively. A: analyzers; M: mirrors; BS: beam splitters; CL: collimator; L: lense; CH: chopper; T: telescope; CE: sample cell; E_1 and E_2 : counterpropagating pump beams; E_p : probe beam; E_c : conjugate beam. .	166

- 6-6. Schematic diagram for DFWM geometries: a, coarse and fine orthogonal spatial grating configuration; b, coarse-grating configuration; c, fine-grating configuration. The symbols • and - indicate vertical and horizontal polarization, respectively ...166
- 6-7. Intensity I_c versus pump intensity for the coarse-grating configuration. Sample (a): $y=4.0696 \times 10^{-7} x^3$; (b): $y=4.4803 \times 10^{-7} x^3$; (c): $y=4.4367 \times 10^{-7} x^3$. Solid lines represent the best fit to Eq.31167
- 6-8. Intensity I_c versus pump intensity for the fine-grating configuration. Sample (a): $y=7.9238 \times 10^{-7} x^3$; (b): $y=1.1726 \times 10^{-6} x^3$; (c): $y=1.6544 \times 10^{-6} x^3$. Solid lines represent the best fit to Eq.31168
- 6-9. Simplified diagram of nano-composite particle embedded in a homogeneous medium is subjected to an electromagnetic field.....169

Abstract of Dissertation Presented to the Graduate School
of the University of Florida in Partial Fulfillment of the
Requirements for the Degree of Doctor of Philosophy

FABRICATION AND CHARACTERIZATION OF NANOMETER-SIZED METAL AND
SEMICONDUCTOR PARTICLES AND NANOMETER-SIZED COMPOSITES

BY

TUO LI

December, 1996

Chairman: Dr. James H. Adair
Major Department: Materials Science and Engineering

A novel technique to prepare nanometer-sized anisotropic inorganic particles has been developed. By using self-assembly molecules as a template, nanometer-sized platelike metal oxide and semiconductor particles can be obtained by confined growth inside the lamellar bilayers of microemulsion systems. It was found that a strong chemical affinity between the metal salt and the polar head group of amphiphilic molecules and the anisotropic structure of microemulsion systems play a premier role in the anisotropic growth.

Nanometer-sized composite particles (nano-composites) with core-shell structure have been prepared by arrested precipitation of metal or semiconductor clusters in reverse micelles, followed by hydrolysis and condensation of organometallic precursors in the microemulsion matrices. Temporally discrete nucleation and growth at elevated temperature (70°C) give the resulting particles a narrow size distribution and defined crystallinity. Both the size of the core particles and the thickness of the coating layers can be varied by controlling processing parameters such as the ratio of water to surfactant and

the ratio of water to organometallic precursors. Nucleation and growth of the core particles and the formation mechanism of the coating layer are investigated. Furthermore, by controlling the pH conditions and aging temperatures a transparent gel composing the nanometer-sized inorganic clusters has been obtained.

Optical properties of nanometer-sized composite particles have been investigated. Quantum confinement effects on the cadmium sulfide nanosize clusters and nano-composites have been studied. For the silver metal clusters and nano-composites the shift of the absorption peak at the surface-plasmon resonance frequency due to classical limited mean-free path of the conduction electrons or quantum size effects has been observed. The enhanced third-order nonlinear susceptibility of the silver nano-composites results from the local field enhancement and size-effects, which has been experimentally demonstrated by optical phase conjugation technique.

CHAPTER I INTRODUCTION

Nanometer-sized metal and semiconductor particles, often called quantum-dots [QDs], and their nanometer-sized composites have attracted world wide attention arising from the fundamental scientific interest in understanding the transition of material properties from the bulk to molecular-like clusters and the potential applications. Due to the confinement of charge carriers to the restricted volume of small particles, quantum mechanical phenomena are observable. The energy band spectrum is considerably altered by the quantum confinement of the extended electronic states. The energy levels are no longer band-like and become discrete. The enhancement of oscillator strength and shift of the onset of absorption spectra towards the high energy end (the so-called blue shift) can be observed as particle size decreases. As particle size approaches this regime, a large percentage of the atoms are on or near the surface. The existence of such a vast interface between the cluster and the surrounding medium can have a profound influence on the physical and chemical properties of the cluster [1]. Areas of application that can be foreseen to benefit from the size-effects of such small particles include quantum electronics, nonlinear optics, photonics, chemically selective sensing, photochemical processing, and information storage.

Over the past ten years extensive research has been carried out in the fields of fabrication of nanometer-sized particles. Great effort has been made in the preparation and characterization of II-VI compound semiconductor quantum dots as well as the novel metal clusters such as Ag, Cu, Pt, and Au. Recently, it has proven possible to prepare III-V semiconductor clusters [2], and even the elemental IV-IV semiconductor quantum dots in solution as well as in the gas phase [3]. Landmarks on this road are the polyphosphate

preparation of CdS [4], size fraction via exclusion chromatography [5], gel electrophoresis [6], reverse micelle preparation [7], and recently, size-selective precipitation of 1-thioglycerol [8].

Although considerable progress has been made in the controlled synthesis of nanometer-sized quantum dots, key problems in these investigations are polydispersities in size and shape, surface electronic defects, and poor crystallinity, which make very difficult the interpretation of physical properties of these quantum dots. Moreover, designing nanometer sized structures and controlling their shape to yield new materials with novel electronic, optical, magnetic, transport, photochemical, electrochemical and mechanical properties are rarely found and present potentially rewarding challenge.

The aim of this work is to exploit the feasibility of using a microemulsion technique to synthesize nanometer-sized quantum structures with desirable size, shape, and size distribution. Moreover, it is expected that the resulting quantum-sized particles and their composites can be applied to the study of the size-dependent effects on material properties as well as to explore their potential use in microelectronic and photonic devices.

Microemulsion systems, reverse micelles and lamellar bilayers were used as microreaction matrices to form nanometer-sized spherical as well as anisotropic platelike metaloxide and semiconductor particles. A lamellar bilayer phase composed of alternating layers of amphiphilic molecules and a polar solvent was used as a template for growing these particles. The critical criteria for the formation of anisotropically-shaped particles were identified. It is essential that the amphiphilic molecules employed in the microemulsion system have a strong chemical affinity to at least one of constituents of the reagents to template particles in the lamellar structure to promote anisotropic growth. The two microemulsion systems employed to prepare platelike particles were sodium dodecylsulfate/amyamine-toluene-water and octylamine-water both of these self-assembly systems can be used to prepare highly anisotropic particles having a narrow size distribution. It was found that the preparation sequence, the equilibration time of the

microemulsion, the ionic concentration and pH of the aqueous phase each influence the characteristics of the resulting particles differently, these processing parameters were subjected to intense study. Anisotropically-shaped semiconductor (CdS) and metal oxide ($\text{Cr}(\text{OH})_3$) particles having potential applications in the fields of magnetic and optical recording media and optical displays have been successfully synthesized using this unique technique.

To meet the demand for the materials having large nonlinear optical response for use in photonic devices and all-optical communication, the nanometer-sized composite particles having core-shell structure were designed on the basis of theoretical predictions and synthesized in reverse micelles through two steps. First, spherical nanometer-sized clusters of a metal such as Ag or Cu, and the semiconductor CdS having various diameters were prepared in reverse micelles. Second, after the formation of nanometer-sized clusters, the fabrication of nanometer-sized composite particles of Ag/SiO_2 , Cu/SiO_2 , and CdS/SiO_2 and CdS/TiO_2 were fabricated by hydrolysis and condensation of the organometallic precursors such as tetraethoxysilane (TEOS) in the microemulsion matrix. The microemulsions used as reaction chambers to synthesize nanometer-sized composite particles were Igepal CO-520 (poly oxyethylene nonylphenyl ether)-isooctane-water and aerosol-OT (AOT)-isooctane-water. The formation mechanism of the nanometer-sized composites and the chemical conditions of metal alkoxide hydrolysis and condensation in reverse micelles were investigated. As a result, it was determined that the size and crystallinity of the particles as well as the thickness of the coating layer can be controlled by varying processing parameters such as the molar ratio of aqueous to amphiphilic molecules, reaction temperature, and the concentration of the metal alkoxide precursors. Different metal alkoxide precursors were used to examine the feasibility of this novel method. For instance, titanium isopropoxide was chemically modified with chelating ligands such as acetylacetone through an exothermic reaction to stabilize the metal alkoxide precursors against fast hydrolysis.

In addition, the gelation of the metal alkoxide in the microreaction matrix was also investigated. A clear, transparent organic gel containing nanometer-sized metal or semiconductor particles was obtained by controlling the pH of the aqueous solution, the aging temperature and by modifying the metal alkoxide precursor, which may have potential to be used in photochemistry processes.

Studies of the optical properties of nanometer-sized particles and their composites were carried out by both linear and nonlinear optical spectroscopies. Photoluminescence (PL) measurements were performed on thin films less than 400 angstroms thick composed of these nanometer-sized CdS composite particles which were spin coated onto silicon substrates and sintered at different temperatures. Absorption measurements were performed on the suspension of nanometer-sized composites. Both the absorption and luminescence spectra of these particles clearly indicate size-quantized effects. For metal clusters and metal/oxide nanocomposites, peak shifting and broadening at the surface plasmon resonance were observed from the absorption spectra as a result of either classical or quantum size-effects. The most important of these studies was the investigation of the enhanced third-order nonlinear susceptibility of metal/oxide nano-composites using the degenerate four-wave-mixing (DFWM) technique. The experimental results were compared with the theoretical results from semi-classical and quantum mechanical models. This is the first experimental proof of the superior performance of size-quantized effects and local field confinement of an electrical field resulting from the nano-composite structures. The scientific significance to the investigation of electronic and optical properties of multi-layered quantum dots and the potential impact on the nanotechnology for electro-optic and photonic applications can be anticipated from these results.

The dissertation is composed of seven chapters. Chapter 2 provides a fundamental review of the quantum size effects on the material properties, the applications and potential benefits of nanometer-sized materials, and the techniques used to fabricate these nanosize structures. The progress on the preparation of the nanosize structures with an emphasis on

the chemical approaches is presented in the later part of this chapter. Chapter 3 demonstrates a novel method, the lamellar bilayer technique, to synthesize anisotropically-shaped and nanometer-sized metal oxide (or hydroxide) and semiconductor particles. The work presented in this chapter is primarily focused on the preparation of nanometer-sized platelike cadmium sulfide particles. Designing and fabricating nanometer-sized composite particles (nano-composites) with core-shell structures are the work in Chapter 4 and Chapter 5. The formation mechanism of the nano-composites and the unique optical properties associated with these structures of semiconductor-oxide and metal-oxide nano-composites are discussed. Chapter 6 presents experimental and theoretical studies of the nonlinear optical properties of the silver-silicon dioxide (Ag/SiO_2) nano-composites. Finally, the conclusions and suggestions for the future are presented in Chapter 7.

CHAPTER 2

INTRODUCTION TO QUANTUM DOTS AND THEIR APPLICATIONS IN MICROELECTRONICS AND PHOTONICS

2.1. Overview

Between the well established and conventional domain of atomic and molecular physics and that of the condensed matter physics, there is an intermediate region dealing with the properties of small aggregates, clusters, or small particles, that are neither quite microscopic nor quite macroscopic. The study of systems of matter in this intermediate region is rather important from a technological point of view for the understanding of problems related to catalysis, chemisorption, aerosols, powder metallurgy, ferrofluids, etc. In addition, it is to be expected that the next level of miniaturization of microelectronic and photonic devices will rely on the systems belonging to this intermediate region. From a more fundamental point of view, the study of this state of matter, intermediate between that of a molecule and a solid, seems to be crucial and should be very interesting because it touches on some rather basic subjects of physical and chemical principles that are usually concealed if one deals with infinitely large systems.

It is this intermediate size regime in which solids gradually lose their bulk properties, approaching more and more molecular-like behavior. One of the most important features, due to the confinement of charge carriers to the restricted volume of the small particles, is quantum size effects, which are providing a rich field for both scientific study and foresee potential in the future in a variety of applications. Some of the scientific issues which have been addressed in the literature, concerning quantum confinement effects in a such matter include the following:

(1) As the dimensions of the materials approach the electron wavelength, the energy band spectrum of the materials is considerably altered; the energy levels are no longer band-like and become discrete (Figure 2-1). In particular, by virtue of its size and potential energy distribution, a quantum dot structure confines carriers in three dimensions, allowing zero dimensions in their degree of freedom and creating atomic-like levels with discrete densities of states.

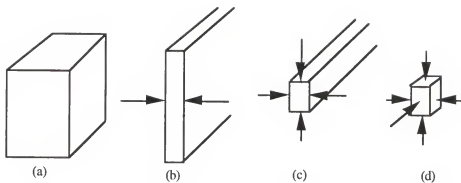
(2) There is an enhanced volume-normalized oscillator strength of exciton features as the radius of the clusters is reduced. This arises because the oscillator strength becomes concentrated over sharp electron-hole transitions, rather than being distributed over a continuum of states as for the case of bulk semiconductors [9].

(3) There is an enhanced excitation nonlinearity and reduction in optical power required for optical saturation relative to the bulk semiconductor. Cooperation among quantum dots for optical nonlinear effects is also an important practical factor [10]

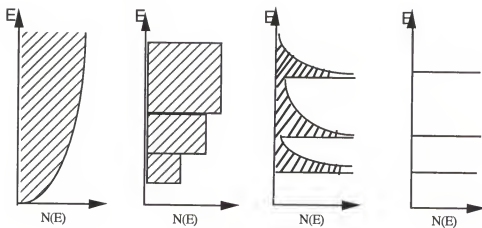
(4) Metal-insulator transitions will occur when both valence and conduction bands break up into subbands, owing to the quantization effects. The transition will occur when the density of states near the Fermi level (E_F) becomes too small for metallic conduction and the conduction band now break up as expected into discrete levels [11].

(5) Surface effects will have a profound influence on the optical, electronic, electrochemical, and photochemical properties of matter due to a diminishing of the difference between the number of surface atoms and bulk atoms as the cluster approach to nanosized region (small quantum dots may have one-third to one-half of their atoms at the surface) [12].

(6) The shape of the quantum dots can influence the energy structures, and therefore, the electronic, optical, and magnetic properties. Unlike that of a bulk crystal, in which the surface is such a small perturbation on the bulk properties, one also has to account for the possible reduction of the symmetry in such a small region [13].



Illustrations representing system dimensionality : (a) bulk semiconductors, 3D; (b) thin films, layer structures, quantum well, 2D; (c) linear chain structures, quantum wires, 1D; (d) clusters, colloids, microcrystallites, quantum dots, 0D.



Density $N(E)$ of states for (a) 3D, (b) 2D, (c) 1D, and (d) 0D systems (corresponding to ideal cases)

Figure 2-1. Quantum confinement in the ideal systems, evolution of the energy via density of states from bulk to zero dimension [14].

Over the past decade, intensive research on quantum dots has been carried out and the study has been spurred on by questions regarding such issues as the effect of confinement of electrons to a small volume on the optical, electronic and magnetic properties of matter; metal-insulator transitions in semimetals and size effects; the physics and chemistry of the photographic process; the influence of particle size on the chemistry and catalysis that occurs on the cluster surface; the spectroscopic, chemical, and physical consequences of embedding a chromophore (or an electron) within a "solvent" droplet of finite size; the role of clusters in the homogeneous nucleation; the possible structural modifications of crystals as a function of decreasing size; and the evolution of phase transitions and other thermodynamic properties as a function of system size. "At the atomic level, we have new kinds of forces and new kinds of effects, and new kinds of possibilities", said Richard Feynman in a visionary lecture over 36 years ago [15 p1].

As an example, electronic and optical properties of semiconductor microcrystallites is one of the subjects under intense investigation. The finite size of the clusters comparable to, or smaller than, the diameter of the bulk exciton, should transform the continuous bands of the bulk crystal into a series of discrete states and shift the lowest allowed optical absorption to higher energies levels. It was found that quantum confinement effects can appear in three different size regions, depending on the average crystallite radius \bar{R} compared to its bulk, electron, and hole Bohr radius. These can be identified as follows:

(1) $\bar{R} \gg a_B$, that is $\bar{R} \gg a_h$ and $\bar{R} \gg a_e$, where a_B is the exciton Bohr radius of the bulk semiconductor, and $a_B = a_e + a_h$, where a_e and a_h are the electron and hole Bohr radii, respectively. This is the regime of weak confinement and the dominant energy is the Coulomb term, and there occurs a size quantization of the motion of the exciton. The shift of the lowest energy state to higher energies by confinement is proportional to $1/R^2$. The shift ΔE in energy of the ground-state exciton is given approximately by

$$\Delta E = \frac{\hbar^2 \pi^2}{2MR^2} \quad (\text{weak confinement}) \quad [2-1]$$

where M , the mass of the exciton, is given by $M = m_e^* + m_h^*$, with m_e^* and m_h^* being the effective masses of the electron and hole respectively; h is Plank's constant.

(2) The second region to consider is $\bar{R} \ll a_e$ and $\bar{R} \ll a_h$ and this is the regime of strong confinement. The Coulomb term now turns out to be small and can be ignored or treated as a perturbation. The electron and hole can be thought of as confined, independent particles, and separate size quantization of electron and hole is the dominant factor. Consequently, the optical spectra should then consists of a series of line due to transitions between subbands. The simple model gives the shift in energy as a function of crystallite size as

$$\Delta E = \frac{\hbar^2 \pi^2}{2\mu R^2} \quad (\text{strong confinement}) \quad [2-2]$$

in which the exciton mass M is replaced by the reduced mass μ where

$$\frac{1}{\mu} = \frac{1}{m_e^*} + \frac{1}{m_h^*}$$

(3) The third region with the condition of $\bar{R} \ll a_e$ but $\bar{R} >> a_h$ is considered to be the moderate-confinement regime and is the usual situation for small crystallites because of the large difference between the effective mass of the electron and the much heavier hole. It is electron motion which is now quantized and the hole interacts with it through the Coulomb potential.

Table 2-1 presents the exciton binding energies and other physical parameters for some selected semiconductors. Experimental studies for region 1 are most readily carried out in semiconductors such as CuCl for which the exciton Bohr radius a_b is small, about 7Å. For region 2, with $R < a_e$, a_h , the II-VI semiconductors such as CdS and CdSe are suitable systems, as well as some of the III-V semiconductors such as GaAs, since these have relatively large values for a_b . The shift to higher energies of the exciton levels and the optical absorption edge, the "blue shift," which results from quantum confinement effects, has been treated theoretically by a variety of well established methods such as effective-mass approximation (EMA) [16], empirical tight-binding method (ETBM) [17],

Table 2-1. Approximate exciton binding energies, Bohr radii and other physical parameters for some selected bulk semiconductors.[14]

Semiconductor	Energy gap E_g (eV)		Exciton binding energy E_b (meV)	Relative dielectric constant ϵ	Exciton Bohr radius (calculated) a_B (Å)
	4K	300K			
CuCl	3.35		~152(189.231)	3.7	7.5, 6.8
CuBr	3.07		104	5.2	12.5
CuI	3.12		(62)		(15)
ZnO	3.38	3.2	67(59)	8.6(8.1)	13
ZnS (hexagonal)	3.87		40	8.3	22
ZnS (cubic)	3.84	3.68	3.6	8.6(5.2)	
2H-PbI ₂		2.32	~24(30)		~20
CdS(hexagonal)	2.58	2.42	27 (A)	8.6	30(20)
TiBr		3.1	23	35	
ZnSe (hexagonal)	2.85		22	8.8	38
ZnSe (cubic)	2.82	2.67	18-20		
GaP	2.35	2.25	(20.5)	11	
AgBr	2.7		16.3	10.6	42
CdSe (hexagonal)	1.82	1.75	14-16	9.4	54(46)
Si	1.12	1.17	14.3 (19.6)	11.4	43
TiCi		3.56	11		~28
ZnTe (cubic)	2.38	2.25	11	9.7	67
CdTe (cubic)	1.60	1.45	10	10.3	75
InP	1.42	1.35		(12)	
GaAs	1.52	1.43	4.2(5.3)	12.4	124(95)
Ge	0.75	0.67	4.15(2.5)	15.4	115
InSb	0.24	0.18	0.6(0.5)		600
PbS	0.41	0.29		(17)	

effective pseudo-potential method (EPM) [18], etc., with each of these methods having certain advantages as well as limitations. A comprehensive review of these theoretical treatments on quantum confinement effects is given by Yoffe [14].

Similar to semiconductor microcrystallites, metallic clusters have also been widely investigated. The central question is, "How does metallic behavior develop with increasing particle size starting from the atomic state?". Answers to this question have been pursued from a wide range of experimental and theoretical directions including magnetic susceptibility, superconductivity, nuclear magnetic resonance (NMR), electron-spin resonance (ESR), heat capacity, linear and nonlinear optical responses, etc. Size effects have been found in these studies either from the classical point of view or from the quantum mechanical point of view. However, each result depends on which physical properties are under investigation. For instance, the optical properties of the metallic clusters are very sensitive to surface plasmon resonance modes that depend on both quantum size effects (or classical limited mean-free path effects) and collective interaction between individual particles and the matrix that supports them. On the other hand, magnetic susceptibility and superconductivity measurements show that the parity of electron number and electron-phonon coupling at the surface states are crucial. Even though size effects have been observed in most of the experiments, the theoretical interpretation related to quantum size effects are often not obvious.

2.2. Applications and Potential Impact

2.2.1. Examples in Microelectronics

In addition to the exciting science they portend, quantum confinement structures, a modern alchemy, promise physical properties that can be harnessed for practical and future electronic and optical applications. To meet the demand for high speed device applications, the development of devices having 2D quantum structures has been substantial. It has been

shown that devices utilizing quantum structures, including high electron mobility transistors (HEMTs), heterojunction bipolar transistor (HBTs), resonance-tunneling hot-electron transistor (RHETs), quantum well lasers, etc., lead to improved performance in many instances over their non-quantum structure counter parts. As an example, resonance-tunneling hot-electron transistors (RHETs) are unipolar transistors which use semiconductor heterojunctions. Their very hot carrier transient time and low forward-bias emitter capacitance allow the possibility of using the device as an ultimate high-speed device (Figure 2-2). Unipolar transistors also can lower power consumption more than bipolar transistors, due to decreased supply voltage. Besides functioning as a hot-electron transistor, the RHETs exhibit a negative transconductance region, which enables them to be used as a new functional device, reducing the number of transistors in the circuit.

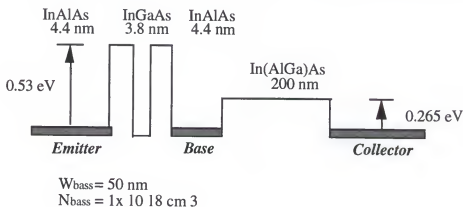


Figure 2-2. Band diagram of the InGaAs-In(AlGa)As resonant-tunneling hot-electron transistors (RHET). (from Ref 19)

The quantum well lasers, for example, a quantum cascade lasers (Figure 2-3), was truly the first band-structure engineered device. A standard double-heterojunction laser simultaneously serves two purposes:

(1) The large index of refraction of the inner layer guides the optical wave between the two outer layers, resulting in a compression of the optical wave compared with its natural extension in an unbounded active medium. This is known as optical confinement.

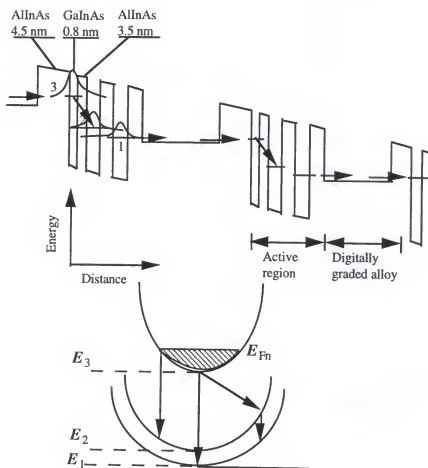


Figure 2-3 Quantum Cascade lasers differ in a fundamental way from diode lasers. In quantum cascade laser, the wavelength, entirely determined by quantum confinement, can be tailored from the mid-infrared to the submillimeter wave region in the same heterostructure materials (Ref.20)

(2) The band discontinuities in the conduction and valance bands confine the electrons and holes (carrier confinement) within the active layer, resulting in a higher concentration of carriers compared with the usual homojunction lasers in which carriers diffuse over distances on the order of microns. This thinner active volume in the heterojunction laser has then a smaller number of states to be inverted to reach gain.

These two effects, optical and carrier confinement, result in a structure that has a more efficient stimulated light emission, since it is easier to reach inversion of carrier population with a given injection current and since the concentrated light will more easily induce stimulated radiative transition. Decreasing the active layer thickness such as single quantum well (SQW) and multiple quantum well (MQW) devices has resulted in further advantages:

(1) Energy levels in the conduction and valance band become quantized. Therefore, lasing will occur at energies determined by the band gap and the quantized energies

(2) Due to wave function and energy quantizations, the density of states becomes 2D. The carriers are more efficient than in 3D since excess carriers will contribute to gain at its peak, whereas in 3D added carriers move the peak gain away from the bottom of the band, making all carriers at energies below gain maximum useless.

Miniaturization in microelectronics has reached the point where conventional techniques have to be changed and new materials and new processing techniques have to be developed. For example, the operation of conventional transistors is based on one of two principles. For bipolar transistors, the basic mechanism is minority carrier injection: the injection of negatively charged electrons from an emitter electrode into and beyond a region where the current is conducted primarily by positively charged holes, or vice versa. Field-effect transistors (FET), on the other hand, are based on the opening and closing of a conducting channel by the influence of an electric field from a voltage on the gate electrode. Discovery of those two effects launched the microelectronics revolution. Although many silicon integrated circuit (IC) applications continue to evolve, it is clear that the current very

large-scale/very high-speed integrated-circuit (VLSI/VHSIC) technologies will eventually reach their limit. As technology drives semiconductor geometries ever deeper into the nanometer domain, the phenomena of classical physics go into retreat and quantum effects become very important, even at room temperature, which restrict the scaling down of device dimensions [21].

First, if the electron is confined to a region smaller than 5 nm, the spacing of the allowed energy level becomes much greater than the thermal energy of the electron. Thus, the electron, if it recombines with a hole, will emit a shorter wavelength of light than if it were free in the crystal.

Second, if the oxide "wall" (potential barrier) confining the electrons becomes thinner than 5 nm, then electrons can tunnel through the oxide; that is, the electrons start "leaking out" of their potential-barrier.

Third, in either case, the electron begins to exhibit interference effects analogous to those in optics: an electron wave can reflect from obstacles, can be "split" and take two or more paths, and can interfere with itself constructively and destructively. Moreover, the single discrete charge comes to be felt, changing the well-known macroscopic nature of resistance, capacitance, and inductance to more a more exotic microscopic one. Therefore, the conventional silicon technology--the mainstay of existing microelectronics--will reach its quantum limit. To go any further, new materials, new technology, and new operating principles need to be invented and established.

One of the promising answers to this problem relies on the development of functional quantum electronic devices based on quantum mechanical principles. By taking advantage of the electron's quantum nature, scientists have found that they can design switches and wires using quantum dots which are far smaller and faster than present ones. In the new computing principle, an individual electron is trapped inside a quantum dot. The electron wave function in a quantum dot can be forced to occupy a specific energy state, narrowing the wave and holding it tight. If a pair of electrons are trapped in an array

of dots laid out at corners of a square (Figure 2-4), the electron mutual repulsion (uncertainty principle) would force them to burrow into opposite corners of the pattern. The two possible configurations could represent a 0 or a 1, creating a simple data register.

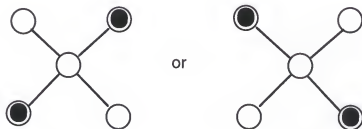


Figure 2-4. Illustration of possible operating principle of a quantum dots data register [21].

Even better, when the pair of electrons have the same orientation, the mutual repulsion between electrons in adjacent arrays, or cells, is lowest, a signal from a control cell would quickly cascade down a long row of cell. In a kind of domino effect, the electron pairs would all align themselves with the first one, transferring data (a 0 or a 1) without any heat-producing flow of current. Therefore, instead of the simple binary, or "on-off", electronic switch now used in computers, microelectronic engineers could fabricate multiple-switch devices using quantum dots and arrange them to function in parallel as an "atomic memory" device. These could lead to more powerful forms of computing logic and become new building blocks that are dramatically smaller and 10,000 times faster than today's best silicon device.

2.2.2. Examples in Photonics

The evolution of information transport media towards the nanosize regime has revolutionized device development in terms of response times and transport efficiency. As an example, consider electrooptic and optical switching. Because photons travel three orders of magnitude faster than electrons in media, they have obvious advantages for signal

transmission. The speed of devices which combine electronics and photonics (e.g., that have been used in optical signal processing and particularly optical switches) can be dramatically improved if the slowest member of the chain, that is, the electric signal used to induce refractive index changes necessary for optical switching, is eliminated [22]. Recent theoretical and experimental results indicate a dramatic change in linear and nonlinear optical response as the dimension of semiconductor and metal clusters reach that at which quantum confinement occurs [23]. The enhanced nonlinear response associated with quantized-effects provides a means to effect optical switching with photons alone at correspondingly faster response times [24].

In an all-optical (or opto-optic) switch, light controls light with the help of a nonlinear optical materials. Nonlinear optical effects may be direct or indirect. Direct effects occur at the atomic or molecular level when the presence of light alters the atomic susceptibility or the photon absorption rates of the medium. The optical Kerr effect and saturable absorption are examples of direct nonlinear optical effects.

The optical Kerr effect [25] is a third-order nonlinear optical process. Similar to the electro-optic Kerr effect for which Δn , the change or nonlinear portion of the refractive index, is induced by an electric field and proportional to the square of the field intensity, the optical Kerr effect is a self-induced effect in which the phase velocity of the wave depends on the wave's own intensity with.

$$\Delta n = \frac{3\eta}{\epsilon_0 n} \chi^{(3)} I = n_2 I \quad [2-3]$$

$$n(I) = n + n_2 I \quad [2-4]$$

$$n_2 = \frac{3\eta}{\epsilon_0 n} \chi^{(3)} I \quad [2-5]$$

Where the η is quantum efficiency, $\chi^{(3)}$ is the third-order nonlinear susceptibility of the optical nonlinear medium, ϵ_0 is the static dielectric constant, I is the intensity of the optical wave, and n_2 is nonlinear refractive index

Indirect nonlinear optical effects involve an intermediate process in which electric charges and/or electric fields play a role, as illustrated by the following two examples.

(1) In photorefractive materials, absorbed nonuniform light creates mobile charges that diffuse away from regions of high concentration and are trapped elsewhere creating an internal space-charge electric field that modifies the optical properties of the medium by virtue of the electro-optic effect [26].

(2) In an optically-addressed liquid-crystal spatial light modulator, the control light is absorbed by a photoconductive layer and generated electric charges create an electric field that modifies the molecular orientation and therefore the indices of refraction of the material, thereby controlling the transmission of light [27].

Nonlinear optical effects (direct and indirect) can be used to make all-optical switches. The optical phase modulation in a Kerr medium, for example, may be converted into intensity modulation by placing the medium in one leg of an interferometer so that as control light is turned on and off, the transmittance of the interferometer is switched between 1 and 0, as illustrated in Figure 2-5(a).

The retardation between two polarizations in an anisotropic nonlinear medium may also be used for switching by placing the material between two crossed polarizers. Figure 2-5(b) illustrates an example of an all-optical switch using an anisotropic optical fiber exhibiting the optical Kerr effect.

It is not necessary that the controlled light be distinct. A single beam of light may control its own transmission. Consider, for example, the directional coupler illustrated in Figure 2-5(c). The refractive indices and dimensions may be selected so that when the input optical power is low, it is channeled into the other waveguide; when it is high the refractive indices are altered by virtue of the optical Kerr effect and power remains in the same waveguide. The device serves as a self-controlled switch. It can be used to sift a sequence of weak and strong pulses, separating them into the two output ports of the coupler.

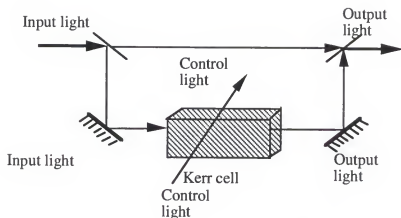


Figure 2-5(a). An all-optical on-off switch using a Mach-Zehnder interferometer and a material exhibiting the optical Kerr effect [26].

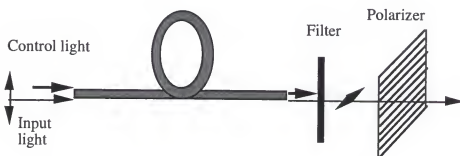


Figure 2-5(b). An anisotropic nonlinear optical fiber serving as an all-optical switch. In the presence of the control light, the fiber introduces a phase retardation π , so that the polarization of the linearly polarized input light is rotated 90° and transmitted through the output polarizer. In the absence of the control light, the fiber introduces no retardation and the light is blocked by the polarizer. The filter is used to transmit the signal light and block the control light, which has a different wavelength [26].

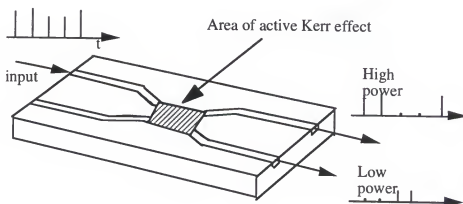


Figure 2-5(c). A directional coupler controlled by the optical Kerr effect. An input beam of low power entering one waveguide is channeled into the other waveguide; a beam of high power remains in the same waveguide [26].

Composites made from small semiconductor or metal clusters isolated in a variety of insulating materials have provided materials in which a wide variety of nonlinear processes may be observed. Many nonlinear phenomena associated with size-quantized effects such as exciton bleaching, enhanced optical susceptibility from super-radiant exciton recombinations mediated by the quantum size confinement, electro-absorption, and quantum Stark effect and second harmonic generation have been observed. However, the mechanism that governs the nonlinear optical processing of semiconductor clusters in the resonance region mainly result from the band-filling (or state filling) process (Figure 2-6). As the intensity of the excitation light increased, the absorption edge at first changes slightly with filling of the lowest energy states. This in itself is a nonlinear process with corresponding change in the refractive index. Upon saturation of the transition, when the rate of filling is equal to the rate of depletion of the lowest energy excited state, any additional photons absorbed must have higher energy in order to promote electrons into the next available state. Photons with lower energy are then transmitted so that the intensity selectivity in Figure 2-6 is achieved. In short, when saturation conditions as a function of the laser intensity are obtained, the interferometer become transparent for longer wavelength and optical switching takes place.

The first experimental study of nonlinear optical properties of such metal colloids was reported by Ricard et al. [28] in 1985. They observed that optical phase conjugation in these media is strongly resonantly enhanced near the surface-plasma resonance frequency. Since composite materials are macroscopically isotropic, their nonlinear response is mainly a third order Kerr effect, is well suited to study optical nonlinearities, and, furthermore, is closely related to important applications such as real-time holographic and bistable memory devices, optical correlator, phase-conjugator devices, optical polarizer, and thresholding devices.

Nonlinear optical responses of metallic clusters appear to be attributed from three essential elements: surface plasmon resonance; quantum size effects; and nonequilibrium

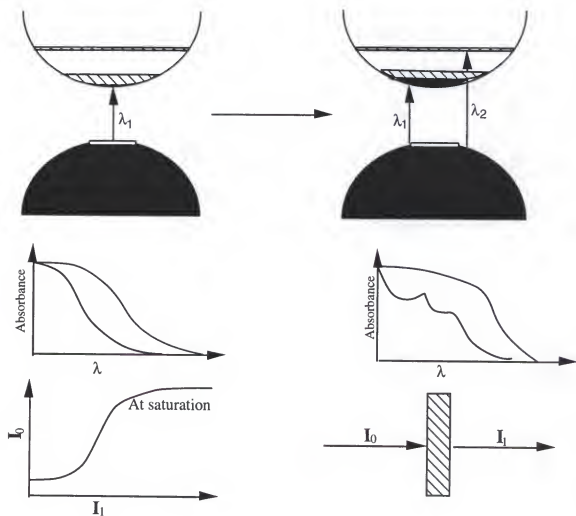


Figure 2-6. Quantum confinement effects on optical absorption. As the photon intensity I is increased, a small blue shift ($\lambda_1 \rightarrow \lambda_2$) is first observed that is due to photo-induced changes in the carrier concentrations. At saturation, only photons with wavelength λ_2 are absorbed [32].

electron heating. At the surface plasmon resonance, large enhancement of the local field inside and in the vicinity of the particles can be realized. In the quasi-static limit the local field of a spherical particle, E_L , is related to the applied field, E_0 , by

$$E_L = \frac{3\varepsilon_d(\omega)}{\varepsilon_m(\omega) + 2\varepsilon_d(\omega)} E_0 = f(\omega) E_0 \quad [2-6]$$

where $\varepsilon_m = \varepsilon_m' + \varepsilon_m''$ is the complex dielectric response of the metal, ε_d is the dielectric function of the host material, and $f(\omega)$ is defined as the local-field factor. The local field enhancement is well known from electro-magnetic theory [29]. The denominator in Eq. [2-6] is the surface plasmon resonance condition for a sphere. The nonlinear source polarization can be written as [28]

$$P_{NL}^{(3)} = 3[pf(\omega)^2 |f(\omega)|^2 \chi_m^{(3)}] E_f E_p * E_b = 3\chi^{(3)} E_f E_p * E_b \quad [2-7]$$

where E_f , E_p , and E_b are the electric fields of the three incident beams in the degenerate four-wave mixing (DFWM) experiment and p is the volume fraction of metal particles in the composite material. A significant feature of the model is the strong size dependence of $\chi^{(3)}$, which is proportional to $1/r^3$, where r is the radius of the metal particle. On the contrary, the Fermi smearing or hot-electron contribution, which has been incorporated by Hache et al., is independent of particle size. In the past few years, several authors including Neeves, Flytzanis and Haus [30-31] have proposed theoretical calculations of the nonlinear-optical behavior based on the model of composite nanospheres with a metallic core (i.e. Ag and Au) (i.e. CdS) and nonlinear shell (i.e., CdS) or with a nonlinear core and metallic shell suspended in a nonlinear medium. Optical phase conjugation is shown to be enhanced from each nonlinear region because the optical field can be concentrated in both the interior and the exterior neighborhoods of the particle and magnified at the surface-mediated plasma resonance.

The ability to generate nano-structure quantum structures confined materials atom by atom in the context of recent scientific developments in nonlinear phenomena is both an intriguing and potentially rewarding challenge.

2.3. Quantum Structures and Atom Assemblies

The basic principle behind quantum structures such as quantum wells (2D), quantum wires (1D), and quantum dots (0D) is the same: In these nano-structures, the dimensions of the wave function of an electron-hole pair (exciton) in the lowest excited state in nano-structures are comparable to the physical dimension of the structures. This quantum confinement of the exciton means that the continuum band of energy becomes more molecular in character having narrow ranges of energy and line structure in the optical spectra. Less delocalization means less energy stabilization; a reflection of this is that the absorption band for direct transitions of nanosized semiconductor clusters is shifted to higher energy states than in the extended bulk parent materials. As a result, photo-induced electrons will be highly concentrated into a narrow conduction state having a small effective density of states. This changes the band gap and modifies the band structures through the so-called "band renormalization process" [33]. In addition to nonlinear optical (NLO) applications, this phenomena can be used to carry out electron-transfer processes that are otherwise inaccessible in bulk semiconductors

One of the most important features of quantum structures is that strong nonlinear responses are observed near exciton resonance, a feature not available in comparable materials with no quantum confinement [34]. In quantum structures the number of states that are available in the relatively small energy band can be very limited, so that adding or removing only a few carriers can substantially change the absorption edge and thus the optical coefficients (such as the index of refraction). Conversely, perturbation of quantum clusters by light can modify the optical coefficients and absorption edge. Small changes in the dielectric properties of the confining structure (including the matrix where the quantum cluster was embedded) or the surface states of the cluster can also introduce large changes in optical and electronic properties which have potential to be used in a variety of applications such as photonic-chemistry and high efficient catalyzes. Quantum confinement can, therefore, be used to change the position and nature of the resonance absorption, as

well as to make the NLO response particularly susceptible to modification by optical and low-frequency electric fields. An additional and equally important property of quantum-confined materials is that ultrafast response times become possible because of the increased importance of surface states.

Experimentally, the architecture of quantum confinement can be achieved in a variety of ways with very different anticipated electrooptic and electronic consequence. An important goal of all approaches is that the synthesis results in a monosize configuration with a single geometrical arrangement of atoms. The desirable size of quantum confinement structures for optimum NLO response depends on the exciton diameter; the effective separation of hole and electron in the first excited state of semiconductor. For large band gap semiconductors such as zinc sulfide (ZnS , $E_g=3.6$ eV) or cadmium sulfide (CdS , $E_g=2.58$ eV), strong confinement will not take place until the size of the cluster reaches their exciton Bohr radius (the exciton Bohr radius are 22 and 30 angstrom, respectively). On the other hand, for small band gap semiconductors such as indium antimonide (InSb , $E_g=0.23$ eV) the exciton will be delocalized over 106 atoms with a diameter of 140 nm.

2.3.1. Physical Approach to Nanometer-Sized Structures

The approach to the realm of the nanosized world has been taken in different ways by physicist and chemists. Engineering of less than three-dimensional semiconductors began in the early 1970's when research groups at AT&T Bell Laboratories and IBM made the first two-dimensional "quantum well" by thin film techniques that can be controlled to build up one atomic layer at a time. In these structures, electrons are confined in a low band gap layer of gallium arsenide sandwiched between higher band gap layer of aluminum gallium arsenide. The first real quantum well device, a resonance tunneling diode, was built using this sandwich structure. Since then, tremendous progress has been made, quantum wells have now become commonplace as the basis of laser diodes which can be

found in compact-disc players and sensitive microwave receivers. Using a combination of sophisticated metal organic chemical vapor deposition (MOCVD) or molecular beam epitaxy (MBE) and nanolithography using X-ray, ion and electron beam techniques, nanophysics can produce one-(quantum wire) or zero-(quantum dots) dimensional quantum structures (Figure 2-7). Furthermore, by using scanning tunneling microscopy, a recent breakthrough in the manipulation and imaging of atomic scale objects utilizing the nanotips of scanning probe microscopes, one can transfer a single atom from site to site on the different substrate.

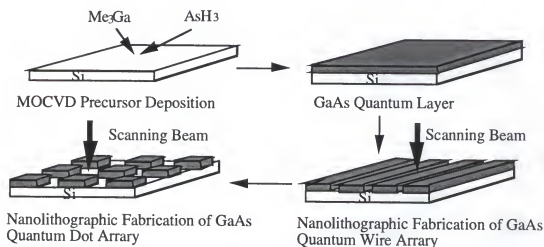


Figure 2-7. Nanophysics fabrication of a GaAs quantum dot array [35].

Although remarkable progress has been made by nanophysics, there are formidable obstacles to overcome. Compared to the growth of its 2D counterpart, the fabrication of quantum wire and quantum dots represents an additional level of difficulty. The known methods of lithography can not be extended to 1-nm feature sizes, but even if this can be overcome by design ingenuity, interfacial impurities and surface damage, which can occur during processing, limit the performance of these quantum structures. The scanning tunneling microscope, which can fabricate such features in such size region, is not known for its speed. Indeed, it may be necessary to develop novel materials and synthesis techniques that blend conventional semiconductor technology with alternative approaches.

2.3.2. Chemical Approaching to Nanometer-Sized Structures

Instead of painstakingly carving out quantum dots from "top to bottom", another approach to this goal is to build the quantum dots from "bottom to top", "atom-by-atom". Building and organizing nanoscale objects under mild and controlled conditions one atom at a time instead of manipulating the bulk, should in principle provide a reproducible method of producing materials that are perfect in size and shape down to atomic dimensions

Over the past ten years extensive research has been carried out in the field of synthesizing nanometer-sized semiconductor particles through nanochemistry. Enormous progress has been made in the preparation and characterization of almost all II-VI semiconductors and various metal clusters through either colloidal chemistry (precipitation in solution) or host-guest inclusion chemistry (growth and positioning of the cluster in/on the organic/inorganic hosts) [36]. Recently, it was proved possible to prepare III-V semiconductor colloids [37]. Even the elemental IV semiconductors have been synthesized in solution as well as in the gas phase [38].

The synthesis of nanometer-sized clusters is often plagued by the tendency of extremely small particles to rapidly agglomerate and precipitate out of solution or to grow to diameters which are well outside the regime of quantum confinement. Although solution chemistry can be a practical route to synthesize both submicrometer and nonsocial particles of many materials, issues such as the control of particle size distribution, morphology and crystallinity, particle agglomeration during and after synthesis and processing of these particles need further investigation. Thus, to have the desirable size and size distribution, conventional precipitation has to be modified and particle growth has to be kinetically controlled, and resulting nanometer-sized particles further stabilized to prevent agglomeration. For these reasons, the synthesis of nanoscale clusters necessitates the use of terminating or stabilizing agents. Many stabilizers which are commonly employed in the synthesis include reverse micelles, polymers [39], glasses [40], zeolites [41], thiols [42], and Langmuir-Blodgett films [43]. These macromolecular stabilizers intimately interacting

with the cluster surface possess extensive positive or negative charge emanating toward the surrounding medium. For example, Figure 2-8(a) illustrates an anionic environment composed of SO_3^- and PO_3^- ions surrounding quantum sized particles in a reverse micelle/hexametaphosphate (HMP) stabilizer. In contrast to HMP, aminocalixarene gives an example of a stabilizer which gives rise to a cationic charge layer at the solution-stabilizer interface. These aminocalixarene molecules are macrocyclic "baskets" with positively charged amino groups on their upper rim. A schematic of quantum size particles stabilized by aminocalixarene molecules is depicted in Figure 2-8(b).

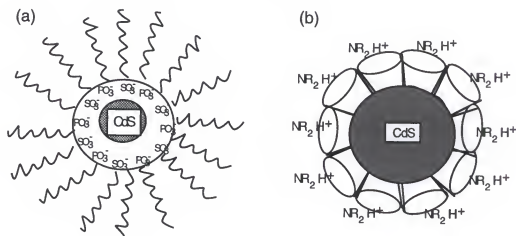


Figure 2-8 Illustration of the interaction of the stabilizing media with Q-CdS clusters. (a) reverse micelle/hexametaphosphate-stabilized Q-CdS (b) p-[(Dimethylamino)methyl]-calix[6]arene-stabilized Q-CdS. [44]

The growth of clusters is kinetically interrupted by these organic molecules physically/chemically capping on the surface of the clusters, and the clusters are "arrested" by these stabilizers apart from agglomeration. This is often referred as "arrested precipitation".

With respect to precipitation in solution, quantum size particles can be synthesized and stabilized inside the void of nano-porous host materials such as molecular sieves or zeolite hosts, which is often called "inclusion chemistry". This is not like arrested precipitation, since the reactions can go to thermodynamic completion within the constraints

of the surfaces that define the 'reaction chamber' topology. Thus, the inclusion chemistry that is used allows selective access to one atom or molecule at a time by ion exchange or gaseous diffusion to the cage or channels in which the self-assembly of quantum size particles is carried out. There now exists a huge range of hosts. They can be of an inorganic, organic or organometallic compositional type, with one-dimensional (1-D) tunnel, 2-D layer and 3-D framework structures. Hosts may be of insulating, semiconducting, metallic or superconducting materials, or may attain these properties following inclusion of the chosen guest. On surveying known host structures, one finds that channel, inter-lamellar and cavity dimensions vary widely in size, separation and perfection, spanning the size range from barely being able to accommodate the smallest ionic or molecular guests all the way to channel dimensions of about 5-10,000 Å, inter-lamellar spaces of 3-50 Å and cavity diameters of 6-10,000 Å. A comprehensive review is given in the volume *Nanochemistry: Synthesis in Diminishing Dimensions* by Geoffrey [44].

The chemistry methods used to fabricate nanometer size structures are generally categorized according to the use of the synthesizing and stabilizing media, which will be discussed in more detail in the following examples:

2.3.2.1. Synthesis of nanosized clusters in organic and inorganic 3-dimensional hosts.

A variety of 3-dimensional hosts is available as a framework for synthesis of nanoscale clusters, including inorganics such as zeolite, porous glass, and molecular sieves crystals of AIPO4-5, H-SAPO-5, Silicalite, and ZSM-5, and organics such as helical graphitic carbon nanotubes, surfactant vesicles, and polymer fibrils, cylinders and wires. These hosts possess ultrafine, periodic cages or channels having nanoscale dimensions. Representative examples of this class of the host include zeolites, porous glasses, black-copolymer nano-domains, and protein cages.

As an example, the zeolite Y occurs naturally as the mineral faujasite and consists of a porous network of aluminate and silicate tetrahedral linked through bridging oxygen

atoms (Figure 2-9). The structure consists of truncated octahedral called sodalite units arranged in a diamond net and linked through double six-rings. This gives two types of cavity within the structure (1) a sodalite cavity of 6.6 \AA free diameter with access through $\sim 2.3 \text{ \AA}$ windows and (2) a supercage of 13 \AA diameter with access through $\sim 7.5 \text{ \AA}$ windows. Whenever an aluminum atom occupies the framework, one negative charge is introduced into the zeolite skeleton which is compensated by loosely attached cations giving rise to the well known ion-exchange properties of zeolites. This inclusion chemistry allows selective access to one atom or molecule at a time by ion exchange or gaseous diffusion to the cages or channels in which the self-assembly of quantum dots is carried out. A variety of semiconductor quantum dots such as CdS and CdSe have been synthesized in zeolites [45]. The quantum confinement is not, however, determined solely by the cross-sectional dimensions of the host channels, since the barriers between the quantum dots are one or two insulating atomic layer thick. This means that resonance and indirect tunneling is also possible by phonon-assisted mechanisms through the overlap of wave functions of adjacent clusters.

Zeolites provide a novel host for the generation of semiconductor hyper lattices within their pore volume. The control of the connectivity between the clusters of semiconductor materials is unparalleled in any other host medium and so has allowed a detailed study of the optical consequences of such connectivity. However, from a practical standpoint, such materials have some severe drawbacks, most notably the lack of single crystals of sufficient size to produce viable optical devices such as optical transistors or spatial light modulators.

Porous glass can be prepared through a variety of synthetic approaches such as sol-gel derived silica. This material consist of macroscopic (centimeter dimensions) monoliths of optically clear silica glass, into the pores of which metals and semiconductors may be introduced using chemistry very similar to that which was used for zeolites. The pores of such glasses range in size from 10 \AA to as large as several hundred \AA controlled largely by

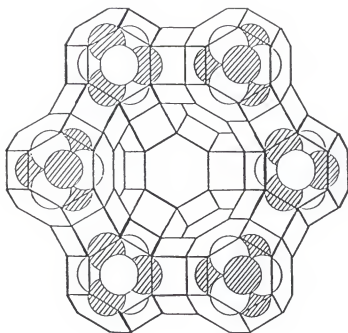


Figure 2-9. The hyperlattices arrangement of CdS clusters in adjacent solalite units of the zeolite Y (hatched=Cd; open=s) [45]

the pH of hydrolysis during synthesis. Unlike zeolites this pore structure is not part of a crystalline matrix and therefore has a distribution of sizes and connectivities. One has to compromise regularity of pore size and topology in favor of ultimate optical and device related properties.

The sol-gel process is a solution synthesis which provides a low temperature chemical route for the preparation of rigid, optical transparent matrix materials. One of the advantage using the sol-gel process is that a wide variety of organic and organometallic molecules can be homogeneously incorporated into SiO_2 , $\text{Al}_2\text{O}_3\text{-SiO}_2$ and organically modified silicate host matrices at the original fluid/sol stage and remain available for conversion to the final products after the rigid glass matrix has been formed. A typical preparation of porous glass through the sol-gel technique involves mixing a metal alkoxide precursor with water, casting a low viscosity liquid sol into a mold, gelation of the mixture through condensation to form a three dimensional network, drying the gel to remove liquid from the interconnecting pore network, and dehydration or chemical stabilization by removal of surface silanol (Si-OH) bonds from the pore network. Semiconductors or metals can be introduced into the porous structures by one of three different routes: First, a metal ion can be introduced into the original sol as a part of precursors of the glass synthesis; it can be converted to the appropriate final clusters by simple annealing of the glass in an atmosphere of reactive gas [46]. Second, the nanoscale clusters may be generated by an impregnation approach [47]. For example, CdS nanoscale clusters may be produced by first impregnating a disk with methanolic solution of cadmium nitrate, drying to 1000 °C in flowing air then exposure to 500 torr hydrogen sulfide. The third route is a variation of method 2, a metal or semiconductor can be introduced into the porous glass by using metal-organic vapor deposition (MOCVD) [48].

2.3.2.2. Synthesis of nanometer sized clusters on organic and inorganic layer hosts.

Growth of nanosized clusters on two-dimensional layers has been recently explored in a variety of layered hosts such as Langmuir-Blodgett film [43, 49], self-assembly multi-

layers [50], layered oxides [51], and inter-lamellar layers of self-assembly molecules [52]. The resulting materials are usually anisotropic and display novel chemical and physical properties that arise from both the nature of their constituents and how they are organized into 2-D arrays. The synthesis is carried out within 2-D regions intentionally built into Langmuir-Blodgett films or self-assembled multi-layers, or existing as an intrinsic part of the overall architecture of inorganic layer host materials. Nanolayer constituents of recently synthesized materials include aligned hyperpolarizable molecules and polymers, magnetically active cations, and quantum-confined semiconductors. Composite layered materials of this type often exhibit novel properties making them attractive, potential candidates in, for example, integrated electronics and optics, information processing and storage, solar energy conversion, electrochromic devices and electrode materials in advanced batteries.

The Langmuir-Blodgett (LB) monolayer transfer method provides a versatile technique for generating controlled-architecture, multilayer films on surfaces. In essence, film formation involves the coherent transfer of a compressed amphiphilic monolayer at an air/water interface onto a chosen substrate. In comparison with molecular beam epitaxy, in which the film material is deposited randomly onto the substrate by evaporation in a high vacuum and must then diffuse laterally to achieve a uniform layer, the formation of a uniform thin layer in LB film is separated into two steps. The first step is the formation of a single layer of molecules, or monolayer, on a water surface. A strong, anisotropic interaction of the molecules with water ensures that they are bound to the surface and have no tendency to form a layer any more than one molecule thick. This layer is initially quite loosely packed and inhomogeneous but by reducing the area of the water surface the molecules are forced together, thus eliminating voids. In the second step, the now uniform monolayer is deposited on the substrate. Precise control over the assembly and growth of large numbers of superimposed layers with accurately defined thicknesses, and different molecules layers can be achieved to build up a molecular superlattice structures (Fig. 2-10).

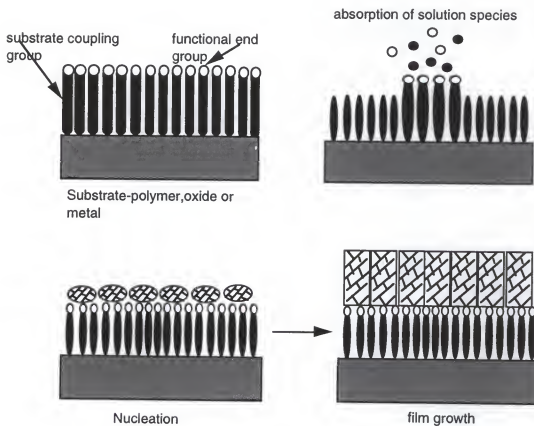


Figure 2-10. Use of Langmuir film containing functional groups to cause and control nucleation and growth of inorganic materials [49].

A number of groups have recently reported on the synthesis of quantum confined II-VI semiconductors, probably with 2-D features, in the hydrophilic interlayer of LB films of fatty acids. The material could be grown by repetition of the process without destroying the proposed layered structure. Manipulation of the layer dimension and composition of size-quantized II-VI semiconductors of this type allows one to fine-tune the optical band gap and redox levels of the conduction and valence bands as well as the linear and nonlinear optical properties of the materials.

2.3.2.3 Synthesis of nanometer sized clusters in organic and inorganic open-frameworks

One of the impediments to the practical utilization of the quantum dots centers around the synthetic challenge of fabricating organized arrays and narrow size distributions of the clusters. In the ideal case of a perfect semiconductor cluster crystal, deleterious inhomogeneous size and shape contributions to their electronic and optical properties are reduced to a minimum, thereby permitting optimum evaluation and exploitation of quantum confinement effects. Host-guest inclusion chemistry provides an attractive method for achieving the goal of monodispersion for these nanoscale cluster materials. The selection of open-framework hosts has encompassed organic, inorganic, polymeric, and biological materials. Here chemical protection and stabilization, together with spatial restrictions imposed by the host, allow one to nucleate, grow and arrest the crystallization of nanoscale clusters in the desirable quantum size regime.

Surfactant, amphiphilic molecules, can self-assemble into a variety of thermodynamically stabilized microstructures such as micelles, vesicles, liposomes, microtubules, and bilayers (Figure 2-11), that are physically, not chemically associated. The formation and evolution of the microstructures from one to another are essentially biological processes and very sensitive to the changes in pH of solution, ionic strength, and temperature. By providing size and geometrical constraints as well as chemical stabilization, these microstructures have been used as a microreactor to precipitated organic and inorganic nanoscale clusters.

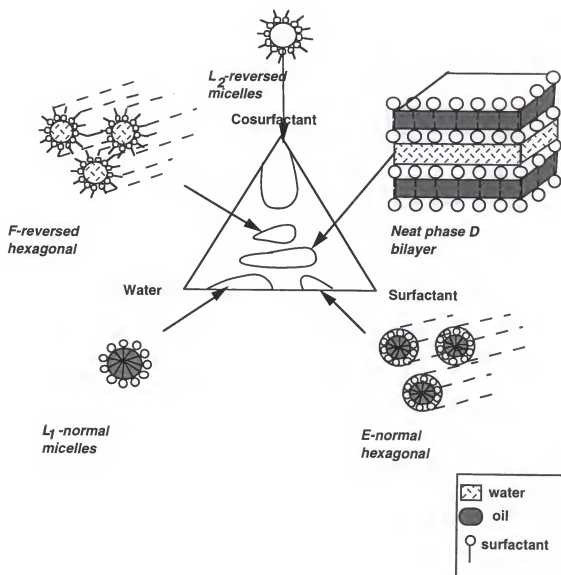


Figure 2-11. The deal amphiphilic aggregates formed in amphiphilic system containing amphiphilic molecules-oil-water [53].

In apolar solvents, amphiphilic molecules with distinct hydrophobic and hydrophilic moieties undergo spontaneous self-association provided an adequate balance exists between the hydrophobic and hydrophilic groups. Above a characteristic concentration [the critical micelle concentration [CMC], the amphiphilic molecules dynamically and spontaneously associate to the aggregates known as micelles. If there is water present, reverse micelles can form when the polar groups of amphiphilic molecules are turned inwards. Water molecules bind to the hydrophilic part of the amphiphilic molecules (polar heads) promoting further aggregation, so that reverse micelles containing immobilized water molecules are formed. Additional solubilization of water results in an aggregates containing free water pools; the system is now referred to as a water-in-oil (W/O) microemulsion. These microspheres of 3-6 nm in diameter, dispersed in the oil phase interact with one another through the two types dynamical processes of inter-micellar collision and intra-micellar exchange in the microsecond and millisecond time domain, respectively.

The water-in-oil microemulsion (reverse micelles) has been the most widely used type of microemulsion system for the preparation of spherical nanoscale clusters. The reagents dissolved inside the water-pools of reverse micelles can react via inter-micellar communication through the dynamic collision process. Nucleation and growth occur as the process proceeds. The particle synthesis methods which have been implemented can be classified into three main groups, that is, (a) microemulsion plus trigger, (b) two microemulsions, and (c) microemulsion plus a second reactant. Figure 2-12 shows how the synthesis reactions may be conducted in each case. It is apparent that a number of chemical reactions involving aqueous, organic and /or amphiphilic reagents may be accommodated in micellar systems through some of these methods or a combination of them. It is important to notice that in these processes the reverse micelles not only serve as a passive host, but also provide hydrophobic and electrostatic interactions between the micelles as well as between the micelle. The reagents used have a profound influence on

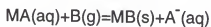
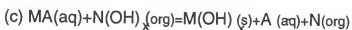
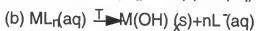
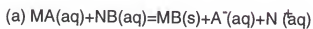
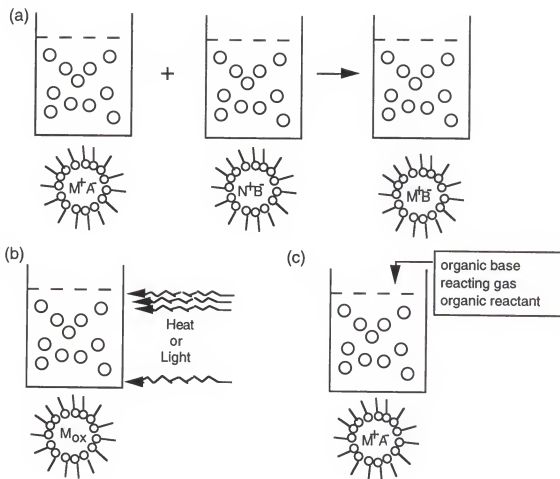


Figure 2-12. Synthesis of nanoscale particles in reverse micelles; (a) Two microemulsions; (b) Microemulsion plus trigger; (c) Microemulsion plus second reactant [56]

the chemical and physical properties of the resulting clusters. Comprehensive reviews of the synthesis on clusters in microemulsion can be found in Ref. [54-55].

A numbers of different inorganic and organic clusters have been prepared utilizing the reverse micelles as a microreactor, including metals [57], metal oxide [58], hydroxide [59], semiconductors [60], and zeolites [61]. To extend further, Steigerwald and Brus [62] have elegantly demonstrated how the II-VI semiconductor particles formed in the nanometer-sized water pools of reverse micelle media by the method of Fendler can be considered to be living polymers capable of further growth, surface functionalization, solubilization, and chemical passivation. They discovered that in the CdSe system, for example, the surface-attached surfactant ligand is labile and can be transiently displaced by sequential additions of Se^{2-} and Cd^{2+} . These grow on the encapsulated CdSe seed to make a larger CdSe crystallite. Moreover, by treating a Cd^{2+} -rich surface with a modified surface coupling agent, PhSeSiMe_3 , it is possible to isolate phenylate-capped (CdSe)-Ph semiconductor crystallites.

The reverse micelles have recently been used to synthesize nanometer metal and semiconductor composite particles [63]. Layered planar semiconductors such as multiple-layered quantum wells have been extensively studied but little is known structurally about such possible concentric inorganic composite microcrystallites. Interest in these materials arises from the investigation of quantum confinement of the charge carriers inside multiple spherical quantum-well but is motivated as well by the development of optical properties that mimic the superior performance characteristics of each individual material. Control over the coating thickness gives an additional engineering degree of freedom to elucidate the underlying physics of these structures. By changing the thickness of the shell and the particle radius, the overlap of the wave functions and the band gap can be changed. The physical parameters of such materials as well as the interface between the "heterostructures" will have a great influence on the optical properties.

Reverse micelles provide an unique way to approach multiple quantum dots structures. Kortan et al. [64] has demonstrated nucleation and growth of CdSe on ZnS quantum crystallite seeds, and vice versa, in reverse micelle media through a two step reaction. In combination with metal alkoxide hydrolysis and condensation inside the microreaction matrix-reverse micelles, metal/oxide and semiconductor/oxide nanocomposites have been successfully prepared in different microemulsion systems. The coating materials can function as a confining layer for quantum dots and in the meantime provide a optically transparent matrix. Furthermore, by controlling the processing parameters such as acidic or basic condition, and temperature and by manipulating the organometallic precursors, different final products such as a clear and transparent gel can be anticipated, which may be sintered into a dense composite body by taking further studies.

Another area newly developed is to synthesize nanometer size anisotropically-shaped particles utilizing anisotropic microstructures such as microtubules, bilayer membranes, and lamellar bilayers. Particles prepared from these microstructures have anisotropic shapes similar to the one where they were synthesized.

Particle morphology is of importance in many applications as well as in fundamental studies of the properties and reactions of solids. Anisotropically-shaped particles have potential over their equiaxed counterpart, which can be further enhanced when their size becomes smaller, especially of the order of submicron or even nanometer scale. Structural, electronic, magnetic, and optical properties of the materials can be greatly augmented by the fabrication of materials with anisotropic microstructures or by the processes of composites with anisotropic particles uniformly dispersed in an isotropic matrix. Examples include structural composites [65], magnetic and optical recording media [66], photographic film, and suspended particle displays [67].

Control of particle morphology is a complex process requiring a fundamental understanding of the interactions between solid state chemistry, interfacial reactions and

kinetics, and solution chemistry. Techniques have been developed that make it possible to produce a large number of inorganic materials of different particle shapes and of narrow size distribution. However, in most cases, the morphology of the final products are rarely anticipated.

Growth of anisotropic nanosize metal oxides and II-VI semiconductor in the inter-lamellar phases composed of alternating layers of amphiphilic molecules and water has been recently developed by J.H. Adair and his research group at the University of Florida. The feasibility of this novel approach has been extensively demonstrated, although the detailed mechanisms involved in the formation of anisotropic particles in the lamellar bilayers have not been fully understood. Initial studies indicated that besides geometrical constraint by anisotropic micellar structures, the critical criteria for the formation of anisotropically-shaped particles is the existence of a strong bond between ionic species of at least one of constituents of the precipitate and the hydrophilic part of amphiphilic molecules at the boundary of bilayer structure. If this condition is fulfilled, an amphiphilic "microreactor" can act as a template to form nanometer size particles with shapes corresponding to the amphiphilic structure employed.

2.4. Future Development and Outlook

The study of size-quantization effects and fabrication of nanoscale quantum confinement structures have been subjected to intense research in the past decade and will continue in the future for the both practical applications and fundamental science. Current trends of electronic and optoelectronic devices are miniaturization and integration. These continuing and unabated drives will lead to many of the new technologies away from bulk materials toward their thin film and nanometer size counterparts. At present, approaches to nano-structures based on chemical synthesis are less highly developed than approaches through physical microfabrication. However, there is little doubt it should be possible to generate a broad range of types of nano-structures by using synthetic chemical approaches:

that is, working "from atoms up" rather than by physical approaches; that is, "from top to bottom". In principle, chemical approaches offer the appeal of a level of control over the selection and placement of individual atoms that is ultimately much greater than that achievable by other methods. However, this increased control over individual nanostructures is purchased at the cost of increasing difficulty in building regular nano-structure arrays required in microelectronic systems. In order to optimize the size-quantized effects, producing monosized nanoscale clusters and assembling these quantum dots in arrays appropriately connected for use in future information processing must be achieved before the practical devices of microelectronics and photonics operating on this new principle become feasible. The solutions to these problems would be both an intriguing and potentially rewarding challenge. All will depend upon chemical progress and understanding and almost certainly will require new materials and processes.

In the meantime, the inclusion chemistry, confining the quantum dots inside crystalline hosts such as zeolites and amorphous such as pores glasses, will still play an important role in revealing fundamental details of quantum confinement effects and cluster/cluster interactions and pre-offer the hope of generating materials for optical switching devices. A range of materials prepared from self-assembly molecules of micellar structures with steadily changing cluster size allow detailed characterization of the size-quantized effects. Furthermore, in conjunction with the sol-gel technique, these cluster could be *in situ* transferred into different supporting matrices which not only have high optical quality but also play an important role in device functions.

CHAPTER 3

PREPARATION OF NANO-SIZE ANISOTROPIC PARTICLES USING SELF-ASSEMBLY MOLECULES AS TEMPLATES

3.1. Introduction

The ability to generate and control the properties and behavior of nanosize particles is central to both materials processing and product performance in many critical areas of modern technology such as catalysis, ceramic processing, solar energy conversion processes, pharmaceutical applications, and photographic technology. Size effects on the electronic and optical properties of these nanosize particles are also under intense investigation due to a fundamental interest in understanding how these properties vary as a crystallite grows from the molecule to the bulk material. Many approaches have been explored for the preparation of such *spherical or at least equiaxed* ultrafine particles, including the use of colloids, polymers, glasses, porous zeolite, and micelles to successfully control the aggregation problem. However, scant attention has been paid to fabricating *anisotropic*, nanoscale particles, which often possess unique physical and chemical properties due to the inherent anisotropic nature of such structures.

Particle morphology is of importance in many applications as well as in fundamental studies and reactions of solids. In some procedures, the morphology of the resulting dispersions is predictable, as is the case with aerosol processes which give spherical final powders. However, in most cases, the morphology of the final product can rarely be anticipated. Numerous examples have been reported showing that the particle shape is sensitive to various experimental parameters such as pH, temperature, reactant concentrations, nature of anions for the same cation, additives, agitation, etc. In some instances particles of different composition and geometry are obtained at the same

temperature with identical reagents at somewhat different concentrations. The same chemical compound of diverse morphologies may precipitate when metal salts of the same cation but different anions are used.

Often a small change in the pH results in solids of different composition, shape or size. For example, iron oxide particles can be precipitated from forced hydrolysis of ferric chloride solution. It is well known that the composition of solutes in solutions containing ferric ions is exceedingly sensitive to salt concentration, pH, anions present, temperature, and length of storage [68]. As a result, a variety of ferric (hydrrous) oxide that differ in chemical composition or particle morphologies may be obtained. The nature of the products may change with only minor adjustment in synthesis parameters. The major particle shapes are rods, spheres, cubes, and double ellipsoids. The crystallographic phases of the rod-shaped particle are α - or β -FeOOH; for the other particle shapes it is hematite [69].

It is known that controlling particle morphology is a complex process and requires a basic understanding of the interactions between solid state chemistry, the mechanisms and kinetics of interfacial reactions and solution chemistry. Generally, the way to control the morphology of the resulting particles from solution is to promote or inhibit the growth of different crystallographic planes of the resulting particle or via the nucleation and growth processes confined in a certain environment, such as in the zeolites and microemulsions containing different mesophases.

Amorphous particles are generally spherical due to their isotropic growth. On the other hand, single crystal particles assume their intrinsic crystallographic habits. Furthermore, it is well known that specific adsorption of ions, complexes, organic compounds, etc., may result in a variety of morphologies of colloidal microcrystallites by restraining or sometimes promoting growth of the facets to which they are absorbed; for instance: 1) dislike hematite produced in the presence of triethanolamine; 2) hexagonal particles of basic iron sulfate $[\text{Fe}_3(\text{SO}_4)_2(\text{OH})_5 \cdot 2\text{H}_2\text{O}]$ with corners and edges rounded off

by excess sulfate ions; 3) octahedral silver bromide obtained by absorption of bromide; 4) the silver chloride particles with either octahedron or rhombododecahedron morphologies in the presence of organic compounds such as dimethylthiourea or cations such as cadmium ions [70]. However, it is far from clear about the mechanism of habit modification of microcrystals despite its fundamental and practical importance.

Gibbs suggested that a polyhedral crystal in equilibrium with the surroundings would assume a shape with the minimum surface free energy. This idea was formulated by Wulff as follows [71]:

$$\frac{\sigma_1}{r_1} = \frac{\sigma_2}{r_2} = \dots = \frac{\sigma_i}{r_i} = \dots = \frac{kT}{2v_m} \ln \frac{p}{p_0} \quad [3-1]$$

σ_i = specific surface energy of the i th face of the polyhedral crystal

r_i = central distance to the i th face

k = Boltzman constant

v_m = molecular volume

p = vapor pressure of polyhedral crystal

p_0 = vapor pressure of a crystal of infinite dimensions

If the vapor pressures are replaced by the supersaturation and equilibrium activities for crystals in a solution, equation [3-1] is converted to the equilibrium form for materials precipitated from solution. According to the above theory, a crystal may grow under supersaturation, maintaining an equilibrium form with its minimum surface energy. However, the growth of the equilibrium form is rarely encountered since the solvent is not inert and unreactive toward the crystal. Specific solvent-solid interactions will modify the surface energies and hence modify the shape of resulting crystal from a specific solvent. The shape of a crystal is determined by the difference in the relative growth rate of the individual crystal planes, and resulting particles are normally bound by facets with the lowest growth rate constant (growth form). Thus, the equilibrium form is the ultimate crystal shape in equilibrium with the surroundings as a result of the recrystallization within the individual crystals in a closed system, whereas the growth form is a kinetically

determined shape created by the difference in growth rate constant among each facet of a crystal with a specific supersaturation.

Particles with the desired shape dictated by the relative growth rate among the various habit planes can be obtained by crystallographically controlled growth as described above. On the other hand, the different morphologies can also be realized by confining nucleation and growth processes of the particles in the presence of host materials including both organic and inorganic inclusions. These hosts possess anisotropic cages, channels, and layers with dimensions from a few angstroms to submicron can provide size, geometrical control, and stabilize the clusters. Furthermore, these inclusions are not only passive hosts, but may have profound influence on the physical and chemical properties of the clusters [41].

Among the various materials which can be used as a host matrix, amphiphilic molecules and their self-assembly associations have great potential to be used to synthesize anisotropically-shaped particles. Molecular self-assembly is the spontaneous association of amphiphilic molecules under equilibrium conditions into structurally stable, well-defined micellar structures. This is well known in colloidal and interfacial chemistry and also is ubiquitous in biological systems and provide the foundation for a wide variety of more complex biological structures. The nature of the micellar structures formed on association of amphiphilic molecules is a more delicate problem. The micellar structures which form are those for which the shape and size has a minimum in surface free energy. The surface free energy is dictated by a number of competing factors such as repulsive forces from the head group, hydrophobic attraction of hydrocarbon chain line, interaction between aggregates at high surfactant concentrations, and relative size and shape of polar and hydrophobic moieties of the amphiphilic molecule. For surfactant alone, a variety of micellar structures are conceivable. These include spherical, cylindrical, micellar, bilayer phase, and inverted structures as shown in Figure 3-1. It has been shown that the structure which forms can be roughly determined by a surfactant parameter V/AI . Here V

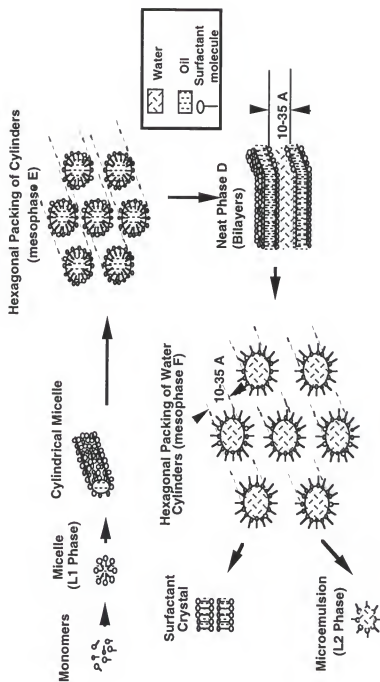


Figure 3-1. Phase structures for an ideal self-assembly system after Mittal and Mukerjee [73].

is the volume of the hydrocarbon chain, A the optimum headgroup area determined by repulsive force and attractive hydrophobic interfacial force, and I the optimum length of the hydrocarbon chain. The following criteria thus apply [72]:

$0 < V/AI$: tendency to form oil-in-water microemulsions

$V/AI > 1$: water-in-oil microemulsions are formed

$V/AI \sim 1$: tendency to form bilayer structures

Thus, amphiphilic molecules can be tailored to produce different structures in the microemulsion. Furthermore, other factors such as composition and concentration of surfactant (amphiphilic molecule), salt concentration, counterion valance, and the use of co-surfactants can be manipulated to promote the desired self-assembly structures [73].

As one of the synthesis techniques for ultrafine particles, self-assembly molecules have the potential to generate non-biological micellular structures [74]. These micellular structures can be used as microreactors within which a variety of nanoscale particles, particularly anisotropically shaped particles may be synthesized, although this is presently difficult through conventional material synthesis. However, while a particular self-assembly system may have an anisotropic structure, spherical particles have usually been produced and little attention has been directed toward controlling the shape of the resulting particles by utilizing the anisotropic aggregates as the microreactors to template anisotropic particles.

The work described herein demonstrates that lamellar bilayer phase consisting of alternating layers of aqueous and amphiphilic molecules can be used as templates to grow platelet metal hydroxide or semiconductor particles. The possible growth mechanisms and critical criteria for the formation of anisotropically-shaped particles will be discussed. For example, it was found that strong bonding between ionic species of at least one constituent of the precipitate and the hydrophilic part of amphiphilic molecules at the boundary of the bilayer structure is necessary to "template" particles in the self-assembly structures. If this condition is fulfilled, then an amphiphilic "microreactor" can act as a template to form

nanometer size particles with shapes corresponding to the amphiphilic structure employed. This research has been conducted toward the synthesis of platelet semiconductor particles (i.e., CdS) and metal hydrous (i.e., $\text{Cr}(\text{OH})_3$). Synthesis of semiconductor platelets, CdS, are of primary interest in the current work.

3.2. Synthesis of CdS Platelets from Lamellar Bilayer Templates

Reagent grade chemicals were used as starting materials. Cadmium nitrate tetrahydrate of greater than 98 w% purity (Fisher Scientific) and cadmium chloride anhydrous of greater than 99.0 w%, and sodium sulfide nonahydrate with 98% purity (Aldrich Chemical Company) were used without further purification. Sodium sulfide nonahydrate is kept refrigerated until just before the preparation of aqueous solution. The other chemicals, toluene (Fisher Scientific), cyclohexane (Fisher Scientific Co.), isooctane (Fisher Scientific Co.), and ammonium hydroxide (29 w% Fisher Scientific Co.), were used as received. Water deionized to a specific resistivity of greater than 10 M Ω was used throughout the experiments. Three different microemulsion systems were used to form lamellar bilayer phases: 1) sodium dodecylsulfate/amyamine-toluene-water; 2) octylamine-water; 3) aero-OT(AOT)-cyclohexane-water. Amphiphilic molecules employed in these systems for the formation of lamellar bilayer phases were octylamine (Sigma Chemical Company), and sodium bis(2-ethylhexyl) sulfosuccinate (Aldrich Chemical Co.). Sodium dodecylsulfate (SDS) of > 98 w% purity and amyamine (AA) (Aldrich Chemical Company) have been used as surfactant and co-surfactant respectively in ternary system.

Two microemulsion systems, sodium dodecylsulfate/amyamine-toluene-water and octylamine-water, have been used to produce hexagonal plate-like CdS particles through the lamellar bilayer in these systems. In terms of partial pseudo phase diagram of SDS/AA-toluene-water system, a composition of 8.8 wt% SDS, 17.7 wt% AA, 9.9 wt% toluene and 63.6 wt % water was initially selected in the region of lamellar bilayer (Figure 3-2a). For the binary system containing octylamine-water, the weight ratio of oil/water were

varied from 0.4, 0.45, 0.5, 0.55, 0.6 and 0.65 through the bilayer region in the binary phase diagram to control the size and thickness of the particles (Figure 3-2b). The various steps involved in the synthesis are schematically illustrated in Figure 3-3. Two lamellar bilayer phase were prepared separately containing Cd^{2+} and S^{2-} ions. The solutions were shaken vigorously. After standing for at least 30 minutes to ensure equilibration of the lamellar bilayer phase, the two solutions were then mixed together in the volume ratio of 1:1 followed by vigorous shaking to homogenize the mixture.

The fundamental reaction which takes place in these "microreactor" of the aqueous layer is as follows:

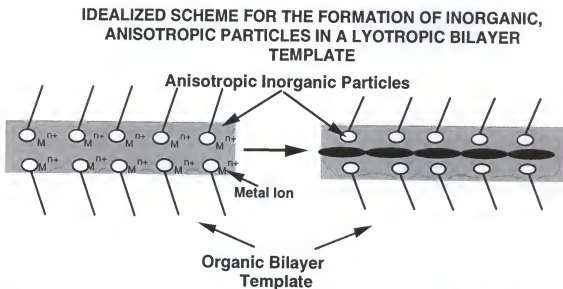
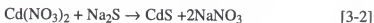


Figure 3-4. Schematically illustrated amphiphilic bilayers acting as a template in the formation of anisotropically-shaped nanoscale inorganic particles.

When at 25°C , $\log K_{\text{CdS}}$ is equal to -26.1 with a stoichiometric solubility for CdS (s) equal to $\sim 10^{-13}\text{M}$ [75]. Thus, the reaction goes to completion for all practical purposes with very little Cd^{2+} or S^{2-} remaining in solution at equilibrium. The mixture of two lamellar bilayer phases was maintained for another 15 min to fully equilibrate the precipitates. The

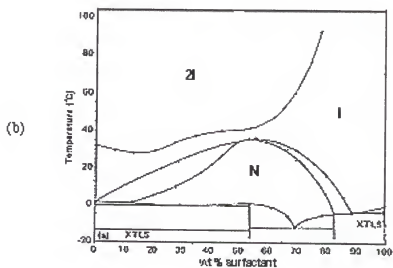
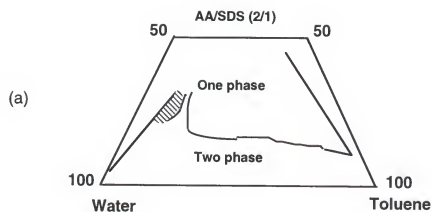


Figure 3-2. Phase diagrams of neat phase D (lamellar bilayer): (a) partial pseudoternary-phase diagram of SDS/AA-toluene-water system [76]; and (b) octylamine-water binary system, and N represent lamellar bilayer phase [77].

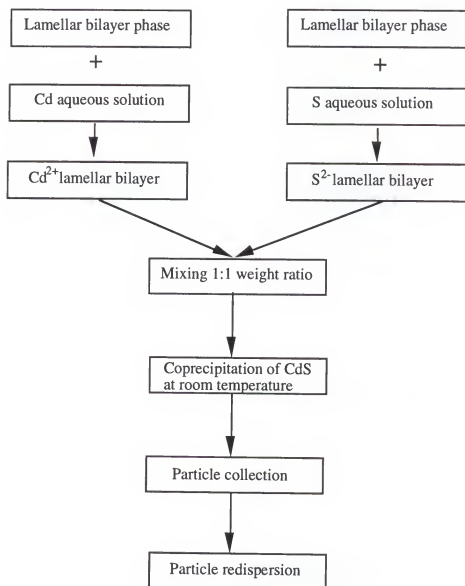


Figure 3-3. Flow-chart used to prepare the platelets of CdS in lamellar bilayer templates

resulting particles were collected by centrifugation at 7000 rpm or 17000 rpm at least 4 times, followed by decantation of the translucent supernatant fluid containing impurities such as amphiphilic molecules or soluble inorganic species, with redispersion in ethanol or methanol by sonicating the suspension for at least three minutes.

Optical microscopy with crossed polaroids and scanning electron microscopy (SEM) were employed to confirm the formation of the lamellar bilayer (Figure 3-5). Information on the shape, size, and distribution of the resulting particles was obtained from scanning electron microscopy and transmission electron microscopy (TEM). Crystallographic information was obtained from X-ray diffraction and TEM. In addition, optical spectrophotometry was used to examine the optical properties and size-quantized effects.

3.3. Results and Discussion

Both of the microemulsion systems have been observed to produce nanoscale platelet-shaped CdS particles from their neat phase bilayers (lamellar bilayer phase) (Figure 3-6). However, the size and distributions of the resulting particles are different. The formation of anisotropic platelets is very sensitive to the compositions of the mesophase as well as to processing parameters, such as reagents and concentrations, and preparation sequence. The possible growth mechanisms and critical criteria for the formation of anisotropically-shaped particles will be discussed as follows:

3.3.1. Characteristics of the CdS Platelets

The hexagonal platelet CdS particles have been observed by SEM and TEM in both of the microemulsion systems. The resulting platelets in the ternary system (SDS/AA-toluene-water) are approximately 200 nm wide and 20 nm thick with narrowly distributed size and shape as shown in Figure 3-6. On the other hand, CdS particles prepared by conventional coprecipitation in aqueous solution were observed to be arbitrarily-shaped

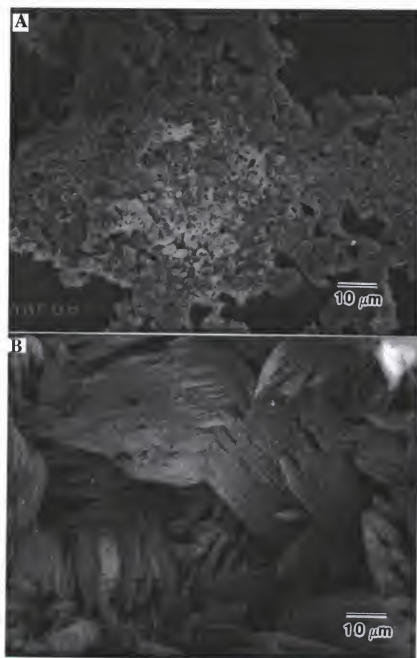


Figure 3-5. Micrographs of the neat phase bilayer (L2) phase in the SDS/AA-toluene-water system: (A) optical photomicrograph of the system under cross Polarizer; and (B) SEM micrograph of partially dried SA system.

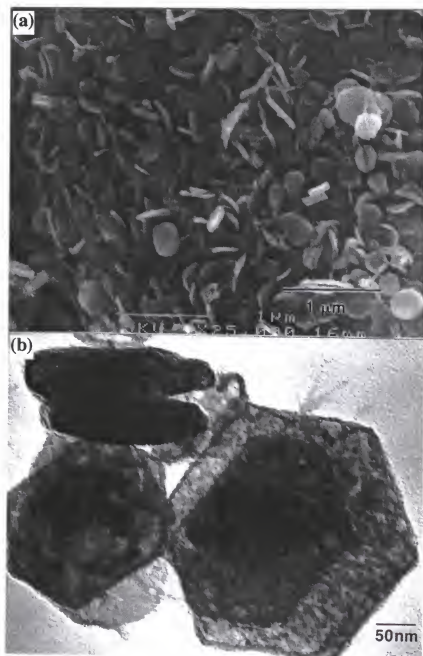


Figure 3-6. CdS platelets: (a) TEM micrograph of CdS platelets synthesized in SDS/AA-toluene-water system; (b) SEM micrograph of CdS platelets synthesized in octylamine-water system.

particles of 5-50 nm as shown in Figure 3-7. These results clearly indicate that the platelet-shape is induced by the templating effect of the lamellar bilayer structure rather than growth in the "equilibrium form".

Compared with the results from the ternary system, the CdS platelets prepared from the nonionic binary system show a large variation of the size distribution (Figure 3-6b). It is believed that the large variation of the size results from temperature sensitivity of the nonionic microemulsion system. Unlike particle formation in reverse micelles in which the solvent content of microemulsion droplets is rapidly exchanged (on a millisecond time scale) through droplet collision, formation of transient dimmers, and breakdown, the particle formation in lamellar phase maybe dominated by diffusion of ionic species within the aqueous layers. The thickness d_w of the water layer depends on the molar ratio of water to surfactant $X = [\text{water}]/[\text{surfactant}]$ [78] :

$$d_w = \frac{2dXM_w\rho_s}{M_s\rho_w} \quad [3-4]$$

Here, d is the length of a surfactant molecule and M and ρ are the molecular weights and densities of water and surfactant respectively. However, this simple relationship can not be applied due to many factors involved in the real dynamic processes during the nucleation and growth, and generally much thicker particles have been observed. So far, there is no explanation which has been proven by experimental evidence. It is postulated that the thicker particles may be due to interconnection of lamellar domains by diffusion and formation of big domains during growth.

It was argued that if the growth of the platelets proceeded inside amphiphilic templates without destroying the bilayer structures, the thickness of the final products should be a function of the thickness of the aqueous layer. In order to test this hypothesis, a series of experiments were conducted by varying the volume ratio of the water to surfactants in the nonionic binary system where the lamellar bilayer phase has a broad region due to the large solubility of water. A TEM study was performed in order to

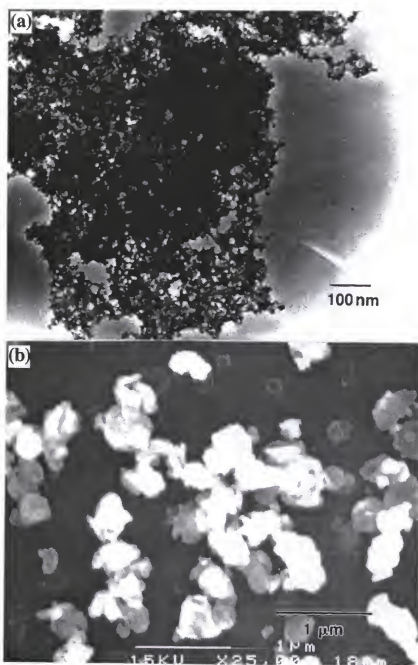


Figure 3-7. (a) TEM micrograph of CdS particles synthesized through conventional coprecipitation in aqueous solution with 0.05 M of metal salt concentration; (b) SEM micrograph of CdS particles synthesized with high metal salt concentration (0.1 M)

provide a more precise measurement of the particle thickness. It was found that the thickness of the platelets is approximately 10-20 nm and varies slightly as a function of the water content. However, the change in the thickness as a function of the volume ratio of water to surfactant could not be quantitatively determined because of the large variation of the resulting particles probably due to the phase instability in the nonionic systems [79].

To extend further, optical characterization was performed by spectrophotometer. It is clear from the UV-visible absorption spectra of CdS particles in Figure 3-8 that there is a correlation between the wavelength corresponding to the onset of the absorption, which is approximately 520 nm in the bulk CdS, and the size of the fine particles. During the last few years, a number of reports on size quantization effect in ultrafine semiconductor particles (i.e. with diameters of 20-200 Å) have appeared. It has been established that the quantum confinement of the electronic states, as a result of the ultrafine particles transforming the continuous bands of the bulk crystal into a series of discrete states or molecular orbital, is responsible for the observed shift of the absorption onset to higher energy with decreasing particle size. Much theoretical and technical interest has been stimulated by the observation that the band gap of semiconductor particles increases with decreasing particle size due to quantum confinement of the charge carriers. It seems that, in the case of our results, the particles are too large to obey the size quantization theory, but the "blue shift" observed in the optical absorption spectra may be caused by the thickness of the particles which is approximately in the range of 10-20 nm.

A crystallinity study was performed by X-ray diffraction and transmission electron microscopy. The sharp peaks of cadmium hydroxide were observed in the samples without post treatment (Figure 3-9a). CdS platelets synthesized in the lamellar bilayer phase were found to be XRD amorphous while CdS particles conventionally synthesized by coprecipitation from aqueous solutions showed a poorly crystallized zinc blend structure which was slightly detectable in the XRD pattern (Figure 3-9c). Selected area electron diffraction (SAED) image was taken from single platelet particle (Figure 3-10).

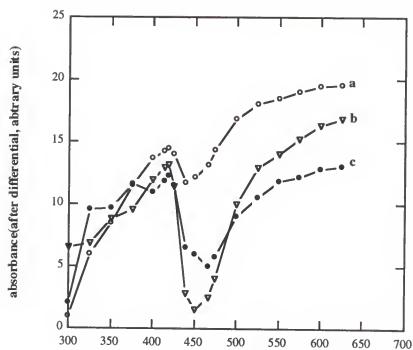


Figure 3-8. Differential absorption spectra of platelet CdS particles as a function of the weight ratio of water to amphiphilic molecules, W . (a) $W=0.8$; (b) $W=1.0$; (c) $W=1.1$

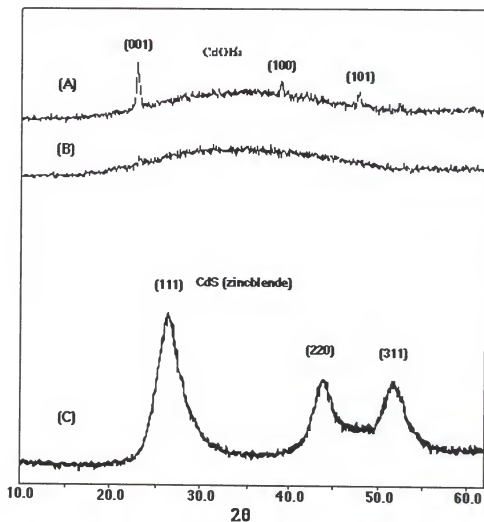


Figure 3-9. XRD patterns of CdS particles: (a): XRD pattern of CdS platelets prepared from microemulsion technique without acid wash; (b): washed with sulfuric acid; (c): XRD pattern of CdS particles synthesized through conventional coprecipitation.

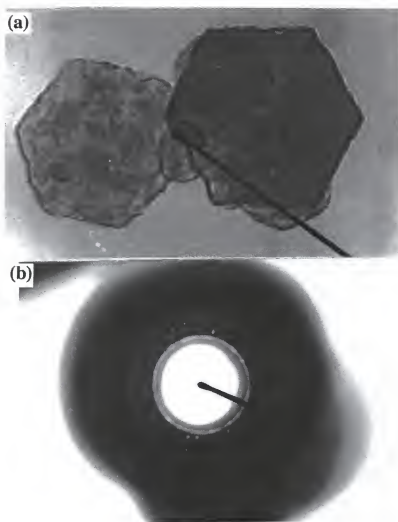


Figure 3-10. TEM micrograph and diffraction pattern of CdS platelets synthesized through lamellar bilayer of octylamine-water system

The result indicates that the CdS platelets are polycrystalline with a zinc blend structure. The results of the SAED also suggest that the single CdS platelet consists of much smaller primary particles. This is consistent with the XRD results, i.e. primary particles are too small to give sharp peaks corresponding to their structure in XRD pattern. Moreover, the size-quantized effect observed from the optical spectra may also be attributed from the nanometer-sized primary particles.

3.3.2. Template Effects

It was found that the sequence of preparing lamellar bilayer phase in SDS/AA-Toluene-Water system is one of the most important processing factors in terms of the influence on the resulting particle size and shape. SDS situated in the system containing AA prior to the addition of cadmium ions seems to interfere with the reaction between organic ligand and cadmium ions. Sodium ions in the aqueous phases might react with the organic ligands of amine groups, and then reduce the number of organic ligands which are available to form coordinate bonds with cadmium ions. Consequently, the resulting particles are arbitrarily shaped instead of platelet-shaped particles. The details are going to be discussed as follows:

Three different mixing sequences have been investigated:

System A: {[AA,TL], H₂O], SDS};

System B: {(SDS,H₂O), (AA,TL)};

System C: {[AA,TL], SDS], H₂O};

Figure 3-11a and b present TEM micrographs of the resulting particles from the different mixing sequences. So far, system A has been tentatively considered to be the standard because it has been the only system that gives rise to platy, nanosize particles with narrowly distributed size and shape as shown in Figure 3-11a. In contrast, these samples prepared from system B and C were different from those prepared using system A. For example, a mixture of platy particles and arbitrarily-shaped particles with broad size

distribution were found in system B (Figure 3-11b). In addition, after aging the sample for 24 hours, large hexagonal, platy particles about 3 μm wide were also found, which suggest that Ostwald ripping (coarsing) is taking place in the sample.

Based on the experimental facts, it is postulated that in addition to the geometrical confinement from the anisotropic microreactors, strong chemical affinity between polar head groups such as nitrogen ligand in the amine groups and the metal ions, which inhabit the particle surfaces in one dimension, makes a primary contribution to the formation of the hexagonal phase of the resulting particles. This hypothetical formation mechanism as shown in Figure 3-12 is composed of three steps: First, metal ions inside the hydrophilic aqueous layer are coordinated onto organic ligand through coordinated or electrostatic interaction. Second, Nucleation occurs on the amphiphilic templates through chemical reactions and followed by layered growth through the diffusion process. Finally, the formation of the platelets is resulted from both the templating effects to promote a preferential nucleation and directional growth and along with the geometrical confinement by lamellar layer structure. The experimental results shown in Figure 3-11 have provided an evidence to support this hypothesis. If the Cd ions was coordinated onto the ligands (for example, amine group), the formation would be likely going through three steps of the hypothesis (Figure 3-11a). If the ligands was partially saturated by other ions, some of arbitrarily-shaped particles was found in the final product (Figure 3-11b). There were no platelike particles If the ligands were completely left out (Figure 3-11c). Due to the over saturation of the solution, besides the platelet formation, some of small aggregates will form onto the surface of platelets and result in the XRD amorphous.

Thus, these results regarding the preparation sequence of lamellar bilayers can be understood based on the above hypothesis. SDS situated in the system containing AA prior to the addition of cadmium ions interferes with the coordination of the cadmium ions

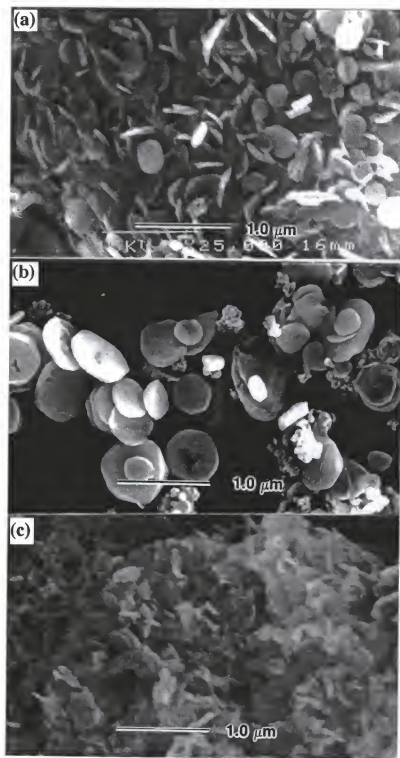


Figure 3-11. CdS particles resulting from the ternary system of SDS/AA-toluene-water, templating effect from organic ligand of amphiphilic molecule: (a) Platelet CdS formation according to the hypothesis; (b) amine groups were partially saturated by other ions; (c) without amine group.

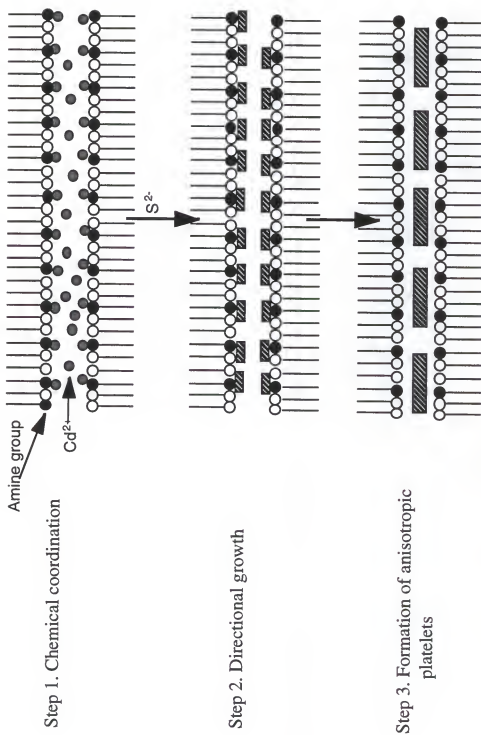


Figure 3-12. Scheme of platelet formation inside lamellar bilayer structure

with organic ligands resulting in the decrease in the quantity of cadmium ions bonded to the AA at the hydrophilic boundary of the bilayer structure.

It is clear that the preparation sequence of the lamellar bilayer phase can greatly affect the resulting particle size and shape through the templating effects. According to the criteria of the formation of anisotropically-shaped particles in the lamellar bilayer phase, strong chemical affinity between at least one of the ionic constituents of the resulting particles and the hydrophilic groups of amphiphilic molecules is said to be critical in the synthesis of anisotropically-shaped, nanosize particles. This is based on the result that platy, nanosize CdS particles are formed in the bilayer structure containing AA while only arbitrarily-shaped particles were produced in the bilayer structure without AA (Figure 3-11c). This leads to the hypothesis that coordination of the metal ions with a lone pair of the electrons provided by the nitrogen atoms in amphiphilic molecules greatly contributes to the formation of anisotropically-shaped particles.

3.3.3. Influence of the Metal Salt and Concentration on the Particle Formation and Morphology

The anion associated with the metal salt and concentration (C_{Ca}) have influences on the resulting particles in different aspects. Among three cadmium salts used in the preparation of the anisotropically-shaped CdS particles cadmium sulfate as well as cadmium nitrate were found to give rise to platy CdS particles. However, Figure 3-13 shows that the shape of resulting particles from cadmium chloride is much less defined. It is likely that a considerable proportion of cadmium chloride dissolved in the aqueous phase as a molecule or complex (i.e. without dissociating into ions completely) while cadmium nitrate and cadmium sulfate dissociated into ions much more in the aqueous phase. Therefore, the difference between cadmium chloride and the other cadmium salts in resulting particle size and shape seems relevant to the nature of the ion bonding. Cadmium chloride may have less template-effect because of less ions available to coordinate with the organic ligands of the template. The growth in the microreactor will therefore lose one of

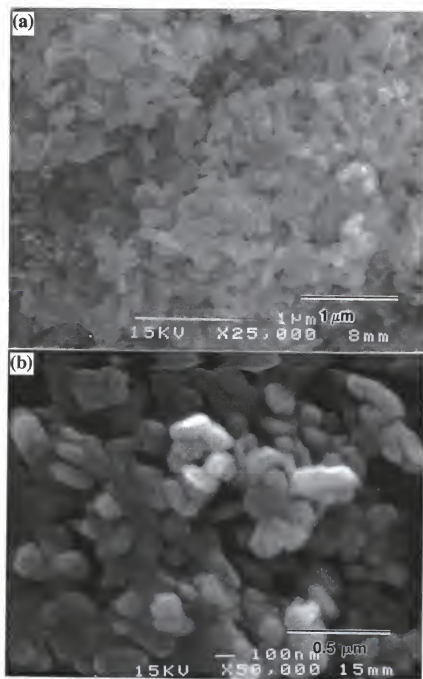


Figure 3-13. The effect of the starting materials on the formation of CdS particles: (a) CdS particles synthesized with CdCl_2 as a starting materials in SDS/AA-toluene-water system; (b) CdS particles synthesized with CdCl_2 as a starting materials in octylamine-water system

the two criteria necessary to form anisotropically-shaped particles in the anisotropic microreactor. As a result, the final products are found to have more arbitrarily-shaped particles.

It was found that there exists two critical points; an upper and a lower limit of concentration of metal ions (Cd^{2+}). CdS particles can not be observed below 0.002 M of the metal salt concentration. Above the upper 0.1 M of the metal salt concentration, the lamellar bilayer phase was changed and separated into two phases. Instead of platelets, arbitrarily-shaped CdS particles were observed (Figure 3-14a.)

As shown in Figure 3-14, platy particles of approximately 200-300 nm wide and 10-50 nm thick were produced when C_{Cd} was 0.02, and 0.05 M (Figure 3-13b-d). In the case of C_{Cd} 0.005 M (Figure 3-14c), the particle size was slightly larger (300-500 nm wide) with an increase in the quantity of arbitrarily-shaped particles.

Seemingly, well-known nucleation and growth mechanisms in terms of supersaturation for monodispersed particles by La Mer et al. may apply to the current work because a low limit existed and an increase in particle width was found at the lowest C_{Cd} (0.005 M) above the low limit (0.002 M). However, the formation process of these platy particles may be more complicated because they are polycrystalline

It is believed that irregular-shaped CdS, obtained when the C_{Cd} was above the upper limit, resulted from the phase changes of the amphiphilic system from the lamellar bilayer to another possible phase. At a fixed composition of amphiphilic molecules-water-oil system the continuous evolution of the mesophases, micelles→lamellar bilayer→reverse micelles, depended on the competition between the two opposite groups of the surfactant and the balance of two forces (hydrophilic and lipophilic) (Figure 3-15). The lamellar bilayer phase, a inter-middle phase, is formed at the region where the two opposite forces are balanced. The high ion concentration will change the mesophase by changing the hydrophilic to a lipophilic. Thus, as the ion concentration increases, the lamellar bilayer becomes unstable and will be destroyed above the upper limit of ion concentration. The

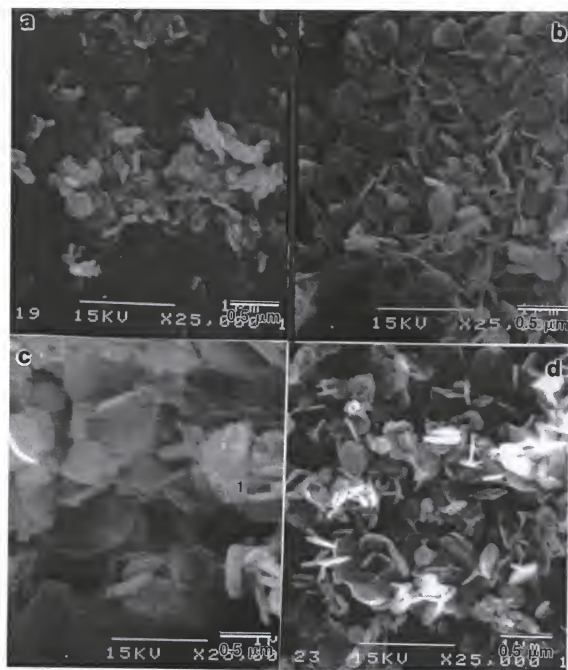


Figure 3-14. Concentration effects on the formation of plate-like CdS particles in lamellar bilayer phase: (a) 0.1 M; (b) 0.02 M; (c) 0.005 M; (d) 0.05 M.

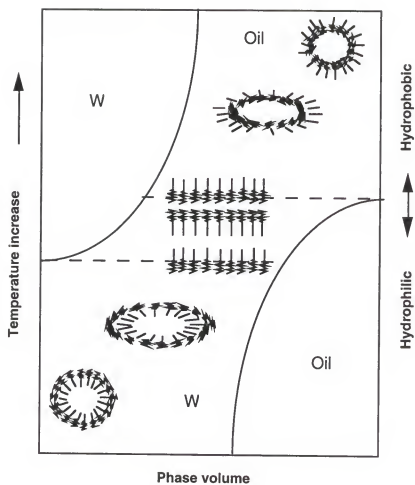
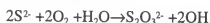


Figure 3-15. Schematic illustration of the change of solution behavior of surfactant with the hydrophile and lipophile balance in water-surfactant-hydrocarbon system [80].

high pH value of the aqueous solution results in the formation of cadmium hydroxide in addition to cadmium sulfide.

3.3.4. Influence of the Other Processing Parameters on the Particle Formation

Studies of the influence of bilayer phase equilibration time, T_1 , and precipitate equilibration time, T_2 , were also carried out to establish a precise synthesis procedure of producing platy CdS particles. It was found that T_1 had no influence on the size and shape of the resulting particles, which implies that the reaction and particle formation in the lamellar bilayer phase was a rapid kinetically controlled process due to the large diffusion rate of the reactants inside the bilayer structure. However, a quantitative increase of impurities such as arbitrarily-shaped particles or fiber-shaped particles was found in both cases with increasing T_1 and T_2 (Figure 3-16). An increase in these impurity implies the presence of a dissolution-reprecipitation reaction of CdS concurrent to the consumption of S^{2-} caused by dissolved oxygen and the possible formation of thiosulfate ion through the oxidation reaction of sulfide ion:



Consumption of S^{2-} by oxygen results in the increase of impurities and low productivity of the desirable particles followed by elimination of particle formation.

3.4. Conclusion of Synthesis of Platy CdS Using Lamellar bilayer Phase

Anisotropically-shaped, i.e. platy, nanosize CdS particles with narrowly distributed size and shape, which can be incorporated into the potential applications such as optoelectronic devices and flat panel suspended particle displays, have been successfully synthesized using lamellar bilayer of self-assembly molecules-water-oil. Focus has been on the investigation of the synthesis conditions with attention directed toward both a fundamental understanding of particle formation in the lamellar bilayer phase and optimization of synthesis parameters, which are summarized as follows:

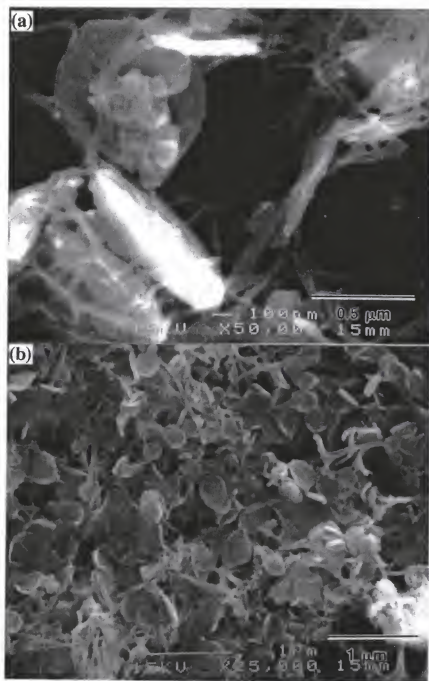


Figure 3-16. The effects of equilibration time (T_1) of lamellar bilayer phase and aging time (T_2) on the formation of CdS platelets: (a) the effect of phase equilibration time; and (b) the effect of aging time.

- 1) Anisotropically-shaped, nanosize CdS particles with narrowly distributed size and shape were synthesized from cadmium sulfate as well as cadmium nitrate using lamellar bilayer phases from both SDS/AA-toluene-water and octylamine-water systems.
- 2) Strong chemical affinity between metal ions and the hydrophilic groups of amphiphilic molecules and the phase stability of lamellar bilayers in the processing conditions are two critical criteria for the formation of the anisotropically-shaped particles.
- 3) Anisotropically-shaped, nanosize particles were found to be XRD amorphous while TEM showed them to be polycrystalline particles of zinc blend type CdS, which indicates that the platy particles observed by SEM and TEM consist of much smaller primary particles,
- 4) The selected microemulsion systems should have a large water solubility in the lamellar phase region and good thermal stability which will allow the precipitation or reduction to proceed over a relatively wide range of temperature. The solubility of the salts should not be limited by specific interactions with the solvent or the amphiphilic molecules.
- 5) For the ternary system of SDS/AA-toluene-water, the preparation of the lamellar bilayer phase was found to be the most critical factor that affected the resulting particle size and shape. It can be attributed to the difference in the quantity of metal ions coordinated with nitrogen atoms of AA molecules.
- 6) There existed lower and upper limits of metal salt concentration. The platy, nanosize CdS can only be produced within this concentration range without destroying the bilayer structure.
- 7) Extended equilibration times must be avoided because aging of S^{2-} may cause the increase of impurities and low productivity of desired particles.

CHAPTER 4

PREPARATION OF NANOMETER-SIZED CdS/OXIDE COMPOSITE PARTICLES USING REVERSE MICELLES IN CONJUNCTION WITH METAL ALKOXIDE HYDROLYSIS AND CONDENSATION

4.1. Introduction

In semiconductor particles of nanometer size, a gradual transition from solid to molecular structure occurs as the particle size decreases. The study of nanometer sized crystallites provides an opportunity to observe the evolution of material properties with size. In this size regime, the physical and chemical properties of the particles strongly depend on their size. A favorite example of property dependent size is the well-established relationship between the optical absorption and size of small CdS particles: with decreasing radius the onset of absorption is shifted to higher energies (size quantization effect). The different rates with which each of the bulk properties develops as size increases provides the possibility to observe and perhaps control novel behavior of nanocrystallites. Potentially interesting properties include nonlinear optical properties, unusual fluorescence behavior, catalytic properties, structure and phase transitions, transport properties, surface chemistry, and their use as precursors for nanostructured materials processing [81].

Because of its optimum characteristics among many available semiconductors, CdS has been the most popular and the best described as an example of the preparation of such nanometer-sized particles and their size quantization effects. A key problem in the preparation is to the ability to control the size and size distribution. Great effort has, therefore, been made to optimize the preparation conditions. landmarks on this road are the polyphosphate preparation of CdS [4], the reverse micelle preparation [7], size

fractionation via exclusion chromatography [5], gel electrophoresis [6], and size selective precipitation of 1-thioglycerol and trialkylphosphine oxide [8] stabilized particles.

Based upon these successes in the synthesis and isolation of pure clusters with a well-defined structure, the final and also optimum goal would naturally come in the development of a technique which can fabricate these nanometer-sized clusters into a usable form for practical applications. Furthermore, this technique will be able to complicate the nanosize structures by surface coating and modification to form nanometer-sized composite particles having an analogy with the quantum-well structures for the studies of the underlying physics and potential applications. So far only very few examples are reported including one by Song-yuan Chang *et al.* [63]. The content of this chapter introduces the basic concept of microemulsion-reverse micelles and their application as microreactors to synthesize nanometer-sized CdS particles. A novel method based on the microemulsion technique in conjunction with hydrolysis and condensation of metal alkoxide precursors *in-situ* in reverse micelles to form metal/oxide and semiconductor (CdS)/oxide nanometer-sized composite particles will be demonstrated. Moreover, by modifying the organometallic precursors and controlling the processing parameters a transparent gel containing the nanometer-sized particles has been obtained. Optical properties of the nanometer-sized semiconductor clusters and the nano-composites have been studied.

4.2 Background

4.2.1. General Remark

Synthesis of nanometer-sized particles is a new emerging field in solid state chemistry. Crystallites of nanometer sizes are inherently unstable due to their high surface energy. Under conventional nucleation/growth conditions, crystallites tend to grow larger than the size domain where "anomalous" nanometer size behavior can occur, thus the preparation of small particles must take place under kinetically controlled conditions. In

addition, even if crystallites of nanometer sizes are formed, they tend to aggregate or undergo Ostwald ripening to minimize their surface tension. Therefore, in view of the factors affecting the size of crystallites it is not surprising to find that successful methods for the synthesis of nanoclusters always involve the use of terminating or stabilizing reagents and/or reaction and control of the diffusion of constituent chemicals with reagent concentration, reaction temperature, choice of reaction media, etc. One successful method for terminating and stabilizing nanosize clusters is the use of solid materials that control particle size by means of their microporous structure and that prevent Ostwald ripening by inhibiting molecular diffusion. Examples of this method include the formation of small CdS clusters within zeolite pores [41] and the formation of PbS and CdS clusters of controllable sizes in polymeric ion-exchangers such as ethylenemethacrylic acid copolymers [39] and Nafion [36]. In the former case the cluster size is controlled by the pore size of the zeolite structure, and in the latter by varying the effective concentration of metal cation within the polymers prior to semiconductor cluster formation.

Another way to synthesize nanometer-sized clusters is to precipitate the clusters in solution by conventional colloid chemistry, and control the sizes by arresting the precipitates in the growth stage using terminating agents. The growth of the cluster is kinetically interrupted by these organic molecules physically or chemically capping on the surface of the clusters, which is often referred to as "arrested precipitation" and is distinct from the conventional method. Examples of the free-standing particles prepared by this method include the precipitation of nanometer-sized metals, metal oxides, and semiconductors in reverse micelles and whiskers and the precipitation of CdS and ZnS clusters using functional organic molecules such as thiophenol as a capping agent [39]. In the former case the clusters precipitate in the water pools of an amphiphilic molecule's aggregates with the size of the final product is ensured by the geometrical constraints of the aggregate's scales, and latter by chemically capping the surface of the clusters to kinetically control the growth processing.

Using various organic and inorganic materials having different pore sizes and structures as a matrix, inclusion chemistry provides an advantage in processing the nanometer-sized clusters into arrays for device applications. However, the synthesis of nanometer-sized clusters in the solid matrices available so far often results in a low concentration of clusters, and makes characterization rather difficult. Furthermore, highly optically transparent matrices with the desired microporosity are seldom found except in porous silica glass. Free-standing nanometer-sized particles prepared by arrested precipitation are therefore preferred in order to characterize nanosize clusters. The disadvantage of the method is that it is difficult to transfer the free-standing particles into a optical quality matrix or arrange these particles into desired arrays for certain applications.

Nevertheless, the needs for close control of the characteristics of nanometer-sized clusters has directed attention to chemically-based particle synthesis techniques. The chemical approaches seek to (a) achieve mixing at the molecular level by using metal-containing aqueous and/or organic precursor solutions, and (b) control chemical homogeneity and particle size by exploiting methods such as inclusion in various solid matrix, or atomization, evaporation, sublimation, and emulsification to form small liquid drops prior to particle production. Among the previously mentioned synthesis techniques, the recent development of microemulsion-based particle synthesis takes the concept of compartmentalization several steps further to its limit, i.e., the molecular level. The feasibility of this novel approach has been extensively demonstrated, although the detailed mechanisms involved in the formation of particles are yet to be understood and completely explained. The relevant literature indicates an impressive diversity in the materials synthesized, microemulsion systems used, and synthesis routes explored. A complex body of information is now available, which needs to be critically examined in order to further advance the science of microemulsion-based particle synthesis. Moreover, fast development of the new technologies continuously demands new materials as well as new synthesis techniques. Thus, to further exploit the potential of the microemulsion-based

synthesis technique to meet the demands of nanometer-size technology is both an exciting and rewarding challenge for both chemists and materials scientists.

4.2.2 Reverse Micelles as Microreactors

Surfactants, denoted as S, dissolved in organic solvents form spherical aggregates called reverse micelles. Reverse micelles can be formed both in the presence and absence of water. However, if the medium is completely free of water, the aggregates are very small and polydisperse. The presence of water is necessary to form relatively large surfactant aggregates. Water is readily incorporated in the polar core, forming a so-called "water pool," characterized by w , the water-surfactant molar ratio ($w=[\text{H}_2\text{O}]/[\text{S}]$). The aggregates containing a small amount of water ($w<15$) are usually called *reverse micelles* whereas *microemulsions* correspond to droplets containing a large amount of water molecules ($w>15$).

The spontaneous curvature for reverse micelles corresponds to the energetically favorable packing configuration of the surfactant molecules at the interface between a polar and an apolar solvent. It depends basically on the molecular geometry. The surfactant molecule can be represented as a truncated cone (Figure 4-1) whose dimensions are determined by the respective ranges of hydrophilic and hydrophobic parts.

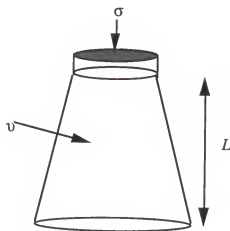


Figure 4-1. Shape of surfactant molecules forming reverse micelles.

Then if v is the surfactant molecular volume, σ the area per polar head, and l the length of the hydrophobic part, the number $v/\sigma l$, called the "packing parameter", gives a good idea of the shape of the aggregates formed spontaneously. In order to form reverse micelles the number of the parking parameter has to be equal to one. The radius of the water droplet can be expressed [55]

$$R_w = \frac{3V_{aq}[H_2O]}{\sigma[S]} \quad [4-1]$$

where V_{aq} is the volume of water molecules. Various experiments confirm the linear variation of the water pool radius with the water content and, at a given water content, the invariance of the water pool radius with the polar volume fraction.

The region of existence of reverse micellar structures in a surfactant-oil-water system can be depicted in terms of pseudo-ternary phase diagrams. The size and location of the thermodynamically stable one-phase microemulsion region is dependent on a number of factors, foremost of which are the nature of the surfactant molecules, the type of oil, the nature and location of the aqueous phase, and the temperature [80]. The ternary diagrams for the Aerosol OT-isooctane-water, and for sodium dodecylsulfate/amyamine-toluene-water shown in Figure 4-2 illustrate the effects of specific surfactant/oil combinations on microemulsion formation. It is worthwhile to point out that due to high surface tension of the ionic surfactant, the middle chain length co-surfactant, (e.g., amyamine for the system in Figure 4-2b) usually a nonionic surfactant, is needed in order to form a stable microemulsion.

Microemulsion droplets are slightly polydisperse, but are a thermodynamically stable phase. On the other hand, the solute content of microemulsion droplets is rapidly exchanged (on a ms time scale) through droplet collisions, formation of transient aggregates, and breakdown of these transient dimers (Figure 4-3). The readiness with which this process proceeds in a given system is determined by the inter-micellar exchange rate constant, k_{ex} , the maximum value of which is the rate constant for diffusion-controlled droplet collisions, k_{en} . Because of reactions in a water-in-oil microemulsion involving

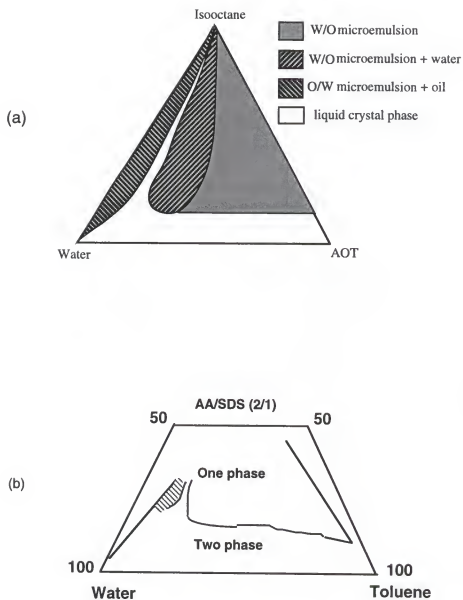


Figure 4-2. (a) The ternary diagram for Aerosol OT-isooctane-water, $T = 15^\circ$ [82]. (b) quaternary diagram for sodium dodecylsulfate/amylamine-toluene-water system [76]. The hatched areas in both phase diagrams denote the lamellar bilayer phase region

reactant species totally confined within the dispersed water droplets, a necessary step prior to their chemical reaction is transferring of the reactants into the same droplet, the dynamic properties of the microemulsion have been subjected to a intensive investigation [83].

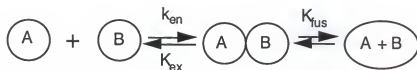


Figure 4-3. The dynamic process of microemulsion

It was found that for very rigid droplet-type structures such as that of Aerosol OT reverse micelles, k_{ex} can be four orders of magnitude lower than k_{en} , i.e. where only one out of 10^4 encounters results in merging and solubilisation exchange. Furthermore, the lability of the interface and thus the rate of exchange in a given microemulsion systems can be significantly altered by temperature and incorporation of cosurfactants and additives [84].

Because of the exchange processes between droplets, described above, microemulsions can be used to synthesize size-controlled crystallites by carrying out coprecipitation or chemical reaction in the water pools. A number of different inorganic materials have been prepared through reverse micellar systems, including metallic and semiconductors clusters [57, 60], carbonate aggregates [85], magnetic particles [86], and colloidal hydrated alumina [87]. In light of these results, specific factors which need to be considered in the design of synthesis processes can be identified as (a) phase behavior and solubilization, (b) average occupancy of reacting species in the water pools, (c) intramicellar interactions, (d) the nature of solubilized water and parameter R , and (e) the dynamic behavior of microemulsion aggregates.

A new field of study has been opened with the solubilization of gelatin in microemulsion systems, which leads to formation of transparent hydrophobic gels based on microemulsions. These transparent gels constitute a dispersive medium with viscosities varying from that of the liquid to true physical gels. The new media offer numerous

perspectives from a fundamental point of view for the study and understanding of gelation mechanisms. This is based on the competition between the branching network induced by the strands of gelatin and the spontaneous compartmentalization induced by the amphiphilic surfactants. The rate of gelation can be controlled by varying the concentration of the micelles and controlling the dynamic process of the microemulsion. From the practical point of view, the photochemical applications appear to be promising, as an optically clear solid organic medium is made available.

4.3. Preparation of CdS/Oxides Spherical Nano-Composites

4.3.1. Synthesis of CdS/SiO₂ Nano-Composites

Reverse micelles were prepared from both ionic and nonionic surfactants using the procedures similar to those of H. Yamauchi [88] and Osseo-Asare *et al* [89]. One of the anionic surfactants used to form reverse micelles was sodium bis(2-ethylhexyl) sulfosuccinate, usually called Aerosol OT or AOT from Aldrich Chemical Company. The nonionic surfactant Igepal CO-520, poly(oxyethylene) nonylphenyl ether, was also from Aldrich Chemical Company. Both surfactants were used without further purification. Other chemicals, such as tetraethoxysilane (TEOS, 99% Fisher Scientific Co.), cyclohexane (Fisher Scientific Co.), isooctane (Fisher Scientific Co.), ammonium hydroxide (29% Fisher Scientific Co.), cadmium nitrate (certified, Fisher Scientific), and sodium sulfide nonohydrate (Aldrich Chemical Co.) were used as-received. Deionized water with a specific resistivity of greater than 10 M Ω was used in the preparation of all reagent solution.

The microemulsion reaction matrix was prepared using either AOT or Igepal. Although different detailed recipes have been used for each preparation, a typical recipe was 20 ml of a microemulsion prepared at ambient temperature in a 30 ml vial with rapid stirring. The microreaction reactant compositions were 4 grams surfactant, 10 mL

cyclohexane and 1.64 grams of $1 \times 10^{-2}\text{M}$ or $5 \times 10^{-3}\text{M}$ aqueous solution of cadmium nitrate and sodium sulfide nonhydrate. The amount of aqueous solution was added in accordance with the different molar ratio of water to surfactant, $R = [\text{water}]/[\text{surfactant}]$. The radius of the water pool could be changed by varying R as discussed previously. Therefore, the size of the resulting particles could also be varied.

In order to optimize the size, size distribution, and crystallinity of the resulting particles, a microemulsion system of anionic surfactant (AOT) containing Cd ions was heated to 70°C using a constant temperature water bath with $\pm 0.01^\circ\text{C}$ variation. After 10 minutes at 70°C , an equal volume microemulsion of S ions without heat treatment was injected into the microemulsion of Cd ions and mixed with rapid stirring. Samples were extracted at different times during the heat treatment.

The general experimental procedure used to prepared CdS/SiO₂ nanosize composites is illustrated in Figure 4-4. After nanosize CdS particles were coprecipitated by mixing two separate microemulsions containing Cd⁺² and S⁻² ions together while stirring, TEOS was injected via a syringe into the stirred microemulsion consisting of CdS nanosize particles. The amount of TEOS injected was varied according to the different molar ratios of water to TEOS, $H = [\text{water}]/[\text{TEOS}]$, which is the most important factor dictating the thickness of the final coating layer on CdS nanosize particles. NH₄OH was injected into the microemulsion to accelerate the condensation reaction of metal alkoxide precursors. Two series of samples were prepared in terms of the two most critical variables, namely, R and H . The structure, size and morphology of the resulting composites were examined by transmission electron microscope (TEM), high resolution transmission electron microscope (HRTEM) and X-ray diffraction spectroscopy (XRD). Optical absorption spectra were collected at room temperature on Perkin-Elmer spectrophotometer. Samples were used in the liquid state with appropriate references. Photoluminescence experiments at room temperature and low temperature were carried out on a SPEX spectrometer with the excitation at 350 nm. Samples used for luminescence measurement were prepared by spin

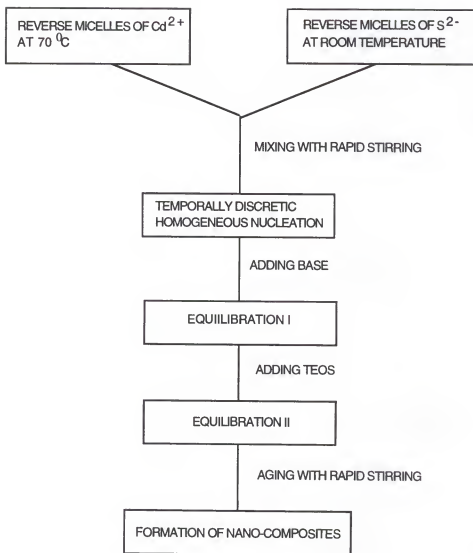


Figure 4-4. Schematic diagram of the synthesis procedures used to prepare CdS/SiO₂ nano-composites.

coating on a Si wafer and followed by heat treatment at 200°C for several minutes. A UV-visible spectrophotometer was also used to monitor the hydrolysis and condensation process in terms of the changes of the optical intensity as a function of time.

4.3.2. Synthesis of CdS/TiO₂ Nano-Composites

The general process used to prepare the composite particles can be described in three steps (Figure 4-5). The first step consisted of the preparation of microemulsion reaction matrix; water-polyoxyethylene octylphenyl ether (Igepal CO-520)-cyclohexane or decane was chosen in such way that the microemulsion would be concluded in the monophased area of the ternary phase diagram shown in Figure 4-2. This microemulsion reaction matrix was used to co-precipitate the nanosize CdS particles. The second step involved modification of titanium (IV) isopropoxide (97%, Aldrich Chemical Co.); modification of the precursors was achieved by adding acetylacetone in a typical ratio of Ti/acacH=1 accompanying the exothermic reaction. The modified alkoxides were diluted with ethanol to obtain a stable solution through an alcohol interchange reaction between the ethoxy and propoxy groups. A typical ratio of the ethanol to the modified precursors, defined as T in this experiment, was T=5. The acetylacetonate modification process for titanium isopropoxide followed by dilution with ethanol is schematically depicted in Figure 4-6. The third step in the process was preparation of CdS/TiO₂ nanosize composites; CdS nanosize particles were coprecipitated by mixing two separate microemulsions containing Cd⁺² and S⁻² ions together with rapid stirring. After 5-10 min. of equilibration, the modified titanium isopropoxide was injected into the microemulsion consisting of CdS nanosize particles using a syringe. The amount of the modified titanium precursors injected was varied according to the different molar ratio of the water to precursors, $H = [\text{water}]/[\text{precursors}]$. Acid (0.1M HNO₃, 28%, Aldrich Chemical Co.) and base (0.1M NH₄OH, 28% Aldrich Chemical Co.) were added to control the relative rate of hydrolysis and condensation in order to obtain different final products.

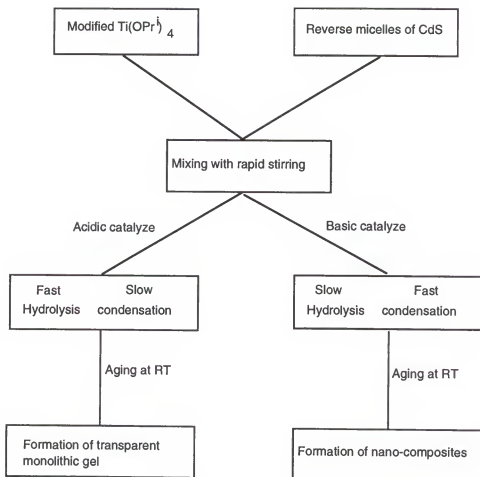


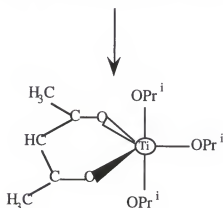
Figure 4-5. Schematic diagram of the synthesis procedure used to prepare CdS/TiO₂ nano-composite and transparent monolithic gel.

(a) Modification of $\text{Ti}(\text{OPr}^i)_4$ through chelating ligands with 1:1 molar ratio



1

1



(b) Alcohol interchange reaction through ethanol with 1:5 molar ratio



1

5

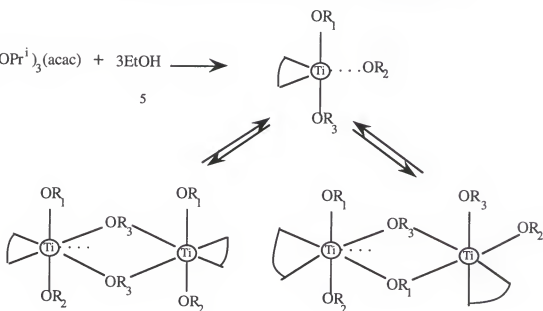


Figure 4-6. Schematic diagram of the modification procedure used for titanium isopropoxide.

4.4. Results and Discussion

Spherical, monodispersed nano-composites with different macrostructures have been successfully fabricated within microemulsion matrices. The formation of nanosize composites in microemulsions proceeded through various stages different in both nature and kinetics. Among the process steps the precipitation of the monodispersed nanometered-sized CdS with well-defined crystallinity appeared to be critical. Furthermore, controlling the rates of hydrolysis and condensation of the organometallic precursors in the microreaction chamber hold the key in the formation of suitable nano-composite particle. Thus, each one of the two steps in synthesis has to be carefully controlled in order to obtain the desired composite structure and crystallinity and will be discussed in details.

4.4.1. Nucleation and Growth of the Nanosize CdS Particles

The formation of metal sulfide particles from metal ion and sulfide ion in reverse micelles involves a chemical reaction stage, a nucleation stage, and a particle growth stage. Takayuki *et al.* [90] reported that CdS particle formation in reverse micelles through nucleation and growth occurred very rapidly and was complete within 20 ms, followed immediately by particle coagulation. The first stage in the precipitation reaction is between the metal ion and sulfide ion resulting in the formation of a metal sulfide molecule. This initial step is described by



Nuclei are formed in the nucleation stage from the oversaturated solute molecules. In the growth stage, larger particles are formed by particle growth, particle coagulation, and Ostwald ripening. Particle growth occurs by the addition of the solute molecules or ions to the particles. Particle coagulation is the result of the combination of the particles, making contact as a result of Brownian motion. Ostwald ripening occurs via the growth over

smaller particles. The overall mechanism of the CdS formation in reserve micelles is governed by the inter-micellar exchange rate control process.

Although considerable progress has been made in the controlled synthesis of II-VI semiconductor crystallites including CdS, interpretation of sophisticated optical experiments often remains difficult due to polydispersity in size and shape, surface electronic defects due to uneven surface stabilizing groups, and even further by the poor crystallinity of the clusters resulting from precipitation at ambient temperature. Thus, having an appropriate high quality model system is essential in distinguishing properties truly inherent to the nanometer size regime from those associated with variation in sample quality. Ideally, the samples must display a high degree of monodispersity, regularity in crystallite core structure, and a consistent surface derivatization (cap). The work of Murray and co-workers [91] on synthesis of semiconductor nanocrystallites by rapid injection of organometallic reagents into a hot coordinating solvent provides guidance to this work.

Because of the large temperature range in which a stable microemulsion can exist [80], an anionic surfactant system, AOT-isooctane (or cyclohexane)-aqueous, was chosen to produce a temporally discrete homogeneous nucleation: injection of reagents into the hot reaction vessel results in a short burst of homogeneous nucleation. The depletion of the reagents through nucleation and the sudden temperature drop associated with the introduction of room temperature reagents prevents further nucleation and separates the nucleation stage from the growth stage, thus achieving monodispersity in the resulting particles. Furthermore, slow growth and annealing in the reaction matrix results in regularity in core structure.

Figure 4-7 presents absorption spectra of nanometer-sized CdS synthesized in the same microemulsion matrix through two different preparation route. Sharpening in the absorption features strongly suggest that the particles resulting from heat treatment have a narrow size distribution [92]. In contrast, the spectra obtained from room temperature

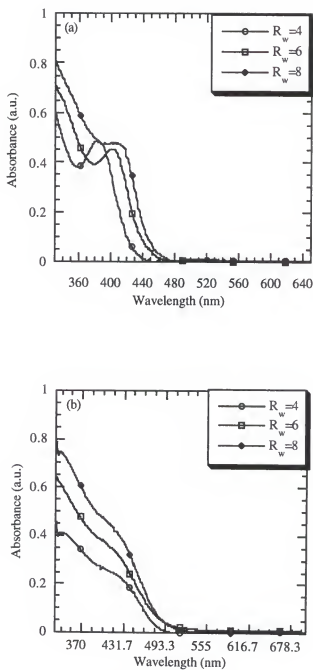


Figure 4-7. Absorption spectra of CdS clusters prepared through two different synthesis routes in microemulsion matrix. R_w represent the radius of water droplet of reverse micelle. (a) synthesized in reverse micelles through temporal nucleation and growth; (b) synthesized in reverse micelles at ambient temperature.

synthesis show less features due to the inhomogeneous broadening as a result of a relatively large size distribution.

4.4.2. Characteristics of the Resulting Particles

X-ray diffraction and transmission electron microscopy were used to determine the crystalline structure. The X-ray diffraction patterns of the CdS particles having various average diameters are shown in Figure 4-8. Due to the small particle size the diffractograms of the samples a-d exhibit only very broad diffraction peaks from which a clear identification of the crystalline structure is not possible. However, in the case of large clusters (samples e-f) averaging 50-80 Å in diameter, the crystalline structure is readily derived from the diffractograms. The clusters resulting from the temporally discrete nucleation method are clearly cubic (zincblende). It should be mentioned that room temperature synthesis of CdS mostly yields the cubic phase, whereas CdS particles in the hexagonal phase were obtained only when high temperatures (above 350°C) were applied [94]. Since bulk CdS is almost exclusively found in the thermodynamically favored hexagonal phase it may be concluded that surface capping and elevated temperature make the growth of the CdS cluster favorable in kinetic control.

In order to elucidate the size and crystal structures, TEM was used to image individual crystallites and develop a statistical description of the size distribution. It was found that the samples prepared from the nonionic microemulsion system without heating are amorphous in nature. On the other hand, the diffraction pattern of the sample from an anionic microemulsion system at elevated temperature reveals a clearly cubic lattice structure (Figure 4-9), which has been observed by several other authors [93].

Furthermore, high resolution TEM (HRTEM) with lattice contrast allows the determination of the morphology of individual crystallites and reveals details of lattice planes in the individual crystallites. Figure 4-10 shows a gallery of single CdS nanocrystallite molecules imaged from three different samples. For the smallest clusters it

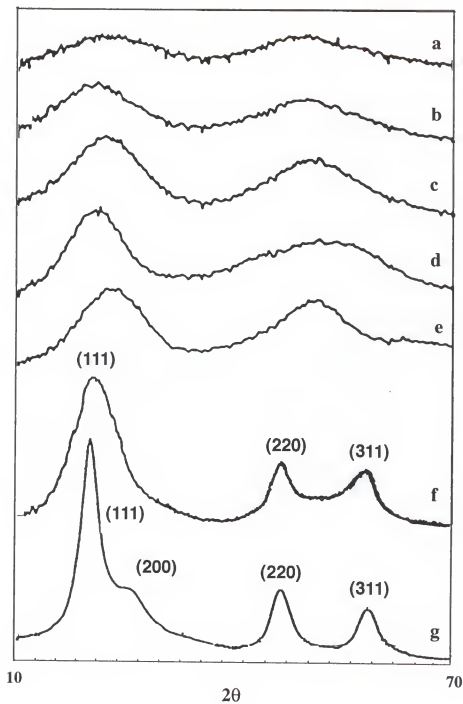


Figure 4-8. X-ray diffraction patterns of the CdS clusters, the evolution of the crystallinity as the cluster size increases (see Table 4-1)

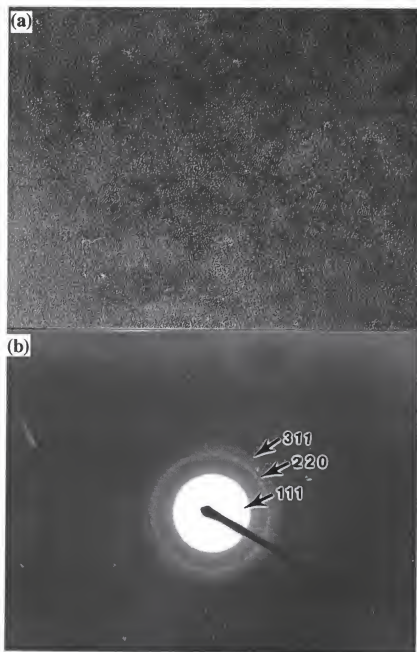


Figure 4-9. TEM micrograph (a) and diffraction pattern (b) of the CdS cluster prepared through temporally discrete homogeneous nucleation from anionic microemulsion matrix (sample b referred in table 4-1).

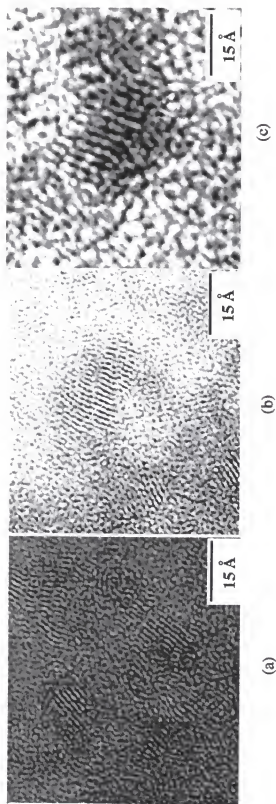


Figure 4-10. Gallery of HRTEM images of CdS Clusters (sample designation and synthesis conditions are given in Table 4-1)

is rather difficult to reliably determine the shape, but in the case of large clusters a nearly spherical shape of the clusters is recognized (Figure 4-10c).

The cluster size and size distribution is determined by high magnification electron imaging. Imaging at 600000 times magnification with moderate crystallites coverage allows careful size measurements of 30-50 individual nanocrystallites on a single image.

Table 4-1. Comparison of size and excitonic transition energy

Sample	R [water]/[surfactant]	Average cluster diameter (Å)	Excitonic transition energy (eV)
a	2	14.06	4.02
b	4	17.86	3.65
c	6	27.81	3.44
d	8	34.05	3.21
e	10	37.50	3.07
g	12	38.24	3.04
f	15	58.75	2.63
h	17	73.70	2.57

4.4.3. Formation of the Nano-Composites in Microemulsion Matrix

4.4.3.1. Influence of the processing parameters

Spherical CdS/SiO₂ nano-composites have been obtained from both AOT-isooctane-aqueous and Igepal-cyclohexane-aqueous systems. Figure 4-11(a) presents some TEM and XPS data for the CdS/SiO₂ nano-composites obtained at the low H range (H<50). Due to the low atomic number of the cluster nano-composites the core-shell structure is hardly recognized in these electron micrographs. However, the XPS analysis indicate the existence of the CdS cluster (Figure 4-11b).

Influence of the processing parameters on the formation of nano-composites have been studied. For a constant R, increasing H decreases the growth rate and the particle

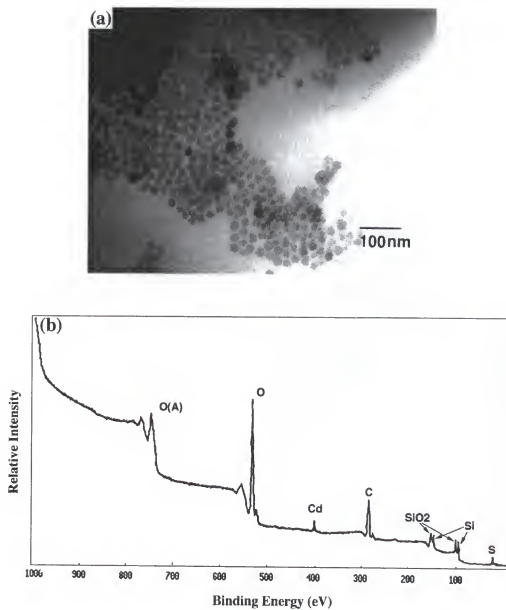


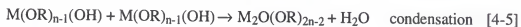
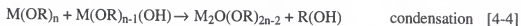
Figure 4-11. (a) CdS/SiO₂ nano-composites synthesized from nonionic surfactant system with R=4, H=100, and X=1. (b) XPS spectra of the nano-composites.

size. This is in contrast to the Stober process, where an increased H increases the hydrolysis rate and increases the particle size [95]. In the lower H region (i.e., $H < 10$), the size of the CdS/SiO₂ composites shows a decrease as the R ratio increases, which agrees with the results obtained by Osseo-Asare [89] in the case of the synthesis of silica particles through the same microemulsion system. Compared with Ag/SiO₂ synthesized under the same conditions, much slower condensation reactions of TEOS precursors in the reaction matrix containing CdS particles have been observed with increasing H. The resulting nano-composites of CdS/SiO₂ obtained at a high H ratio have a polydisperse size distribution.

To control the relative rate of hydrolysis and condensation reactions and to obtain a stable suspension, the amount of base added was monitored by the ratio of the base to TEOS, designated as X. A series of experiments has been conducted at various X ratios with the same R and H. As a result, a stable suspension can only be obtained when X is close to 1, and the suspension will sediment with increasing X due to perhaps a faster condensation reaction resulting in larger particles.

4.4.3.2. Mechanism of the nano-composites formation

To explain the influence of these processing parameters on the resulting composite particles, a formation mechanism of nano-composite particles in a microemulsion matrix has been proposed and schematically illustrated in Figure 4-12 and Figure 4-13. As in an alcoholic solution of water and bases such as ammonia, metal-organic derivatives within the microemulsion reaction matrix are also undergoing a hydrolysis reaction and two possible condensation reactions, which can be represented as follows [89]:



As a first approximation, we may assume that the reverse micellar aggregates present in the solution are not affected by the addition of TEOS molecules nor by the subsequent

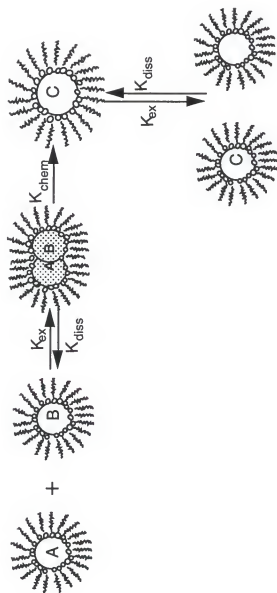


Figure 4-12. Scheme of the particle formation in reverse micelles; chemical species of A and B meet in transient dimer to form C through chemical reaction.

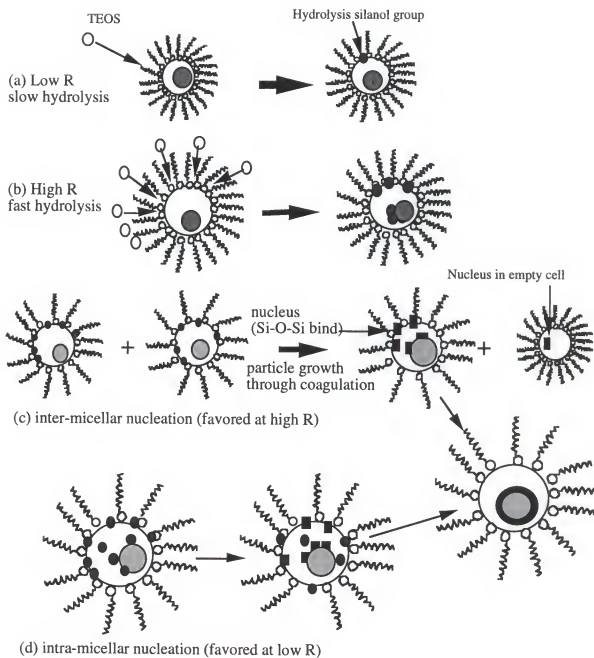


Figure 4-13. Scheme of the composite particle formation in microemulsion reaction matrix.

reactions, and in particular that the aggregation numbers (micellar concentration) remain unchanged. Under these assumptions, the TEOS alkoxide molecules interact rapidly with the water molecules inside the reverse micellar aggregates, forming partially hydrolyzed species. Once formed, these hydrolyzed species remain bound to the micellar aggregates due to their enhanced amphiphilic character (brought about by the formation of silanol groups) (Figure 4-13). In this case all further reactions are restricted to the locale of the micellar aggregates, and thus the overall mechanisms of particle nucleation and growth involves both intra and inter-micellar events. On this basis, it is likely that hydrolysis may occur in each reverse micelle (basically an intra-micellar process). On the other hand, condensation (particle growth) may occur within a given micelle or by inter-micellar contacts. Therefore, formation and size of the composite particles depends on the relative rates of the hydrolysis and condensation reactions. There are several factors which may affect the rate of hydrolysis in reverse micelles; the rate of the hydrolysis decreases as the R ratio decreases. With low water content (small R ratio), most of the water molecules are bound to the polar head of the surfactant molecules. Thus, the hydrolysis rate is slow. With increasing water content (R ratio), more free water is available to participate in the hydrolysis reaction. Thus, the hydrolysis reaction can be expected to be enhanced when more free water is present. The H ratio affects the rate of hydrolysis by enhancement of the diffusion rate of the TEOS alkoxide molecules into the reverse micelles. It was found that the rate of hydrolysis in the reverse micelles containing Ag (as discussed in Chapter 5) is faster than that of reverse micelles containing CdS and results in a more uniform distribution both in the size and thickness of the shell. These results imply that the nature of the core materials and the particle surface play an important role in the interaction between the core particles and the hydrolyzed silanol group which leads to the surface modification. The core materials may also affect the hydrolysis process by influencing the pH value inside the reverse micelles.

The "unseeded" SiO_2 particles have been found in the final products of the composite particles according to the reaction route (Figures 4-12 and Figure 4-13), which may be attributed to the distribution of the ionic species of the core material in the reverse micelles, or the dynamic process of the inter-micellar interaction. First, the reverse micelles may not be fully occupied by the ionic species of the core's materials in the first stage if the concentration of the micelles is larger than that of the reactants. Thus, empty micelles will exist where the SiO_2 particles can form followed by hydrolysis and condensation of TEOS alkoxide molecules. Second, the empty micelles may also form during the dynamic process of inter-micellar interaction. The "empty" droplets may be released during the inter-micelle interaction as suggested by Fletcher [96].

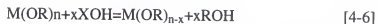
Large resulting composite particles of CdS/SiO_2 have been obtained as the R ratio decreases while the H ratio has been kept below 50 (large TEOS content). Thus far, these results have not been fully understood. In the case of the growth of pure silicate through microemulsion, Osseo-Asare postulated that if the dominant mechanism of particle growth is diffusion controlled inter-micellar interaction which results in aggregation of the nuclei and thus in a fewer number of growing particles, particle growth would be favored at small R values since micellar collision is higher. This would result in larger particles at small R values, which has been found in the formation of CdS/SiO_2 . However, the opposite results were found in the case of Ag/SiO_2 (chapter 5), in which the size of the resulting composite particles showed a nearly linear increase as the R ratio increased. It was again speculated that the chemical nature of the core material plays an important role in controlling the hydrolysis rate of organometallic precursors. Silver clusters with a acidic nature may have stronger catalysis behavior to protonic silanol groups and thus enhance the hydrolysis rate [97]. As a result, higher concentrations of Ag ions in the large R ratio will give a larger sizes for the composite particles. Even in the case of the low R and high H (less TEOS precursors available), the growth mechanism could also be very different with pure silica. Because of the existence of the core materials, surface modification and growth of

the TEOS precursors will most likely occur on the heterogeneous surface of the core instead of growing the pure silica or filling the empty micelles generated during inter-micellar collision due to low oversaturation level.

Therefore, the rate of hydrolysis and condensation of TEOS alkoxide molecules in reverse micelles are determined by R, H, bulk solvent, and the core materials. At the low R region (keeping X and bulk solvent unchanged) the rate of the hydrolysis is low due to less free water within reverse micelles. The slow reaction and less TEOS precursors (large H) result in a slow growth of the composite particles. However, it has been observed that at the same synthesis condition, "rigid" Ag/SiO₂ nano-composites with well defined spherical core-shell structures were resolved compared with "soft" barely spherical CdS/SiO₂, which indicate that the core materials have indeed a great influence on the growth of the nano-composites.

4.4.3.3. Chemical modification of titanium alkoxide

One of the main drawbacks of transition metal alkoxides is their high reactivity with water due to their lower electronegativity and the ability to exhibit several coordination states. Fast hydrolysis rates with these alkoxides make polycondensation difficult to control, therefore less reliability of the final product can be assumed. Thus chemical additives are almost always used in order to improve the sol-gel process and obtain better materials. Such additives can be solvents, acidic or basic catalysts, or stabilizing agents. In most cases they are nucleophilic XOH molecules that react with the alkoxide giving rise to a new molecular precursor:



The chemical reactivity of the alkoxide with nucleophilic species mainly depends on the following three factors:

1. The electrophilic power of the metal atom increases when its electronegativity decreases.
2. The ability of the metal to increase its coordination which can be estimated as the difference between its usual coordination number N in the oxide and its oxidation state z.

3. The nucleophilic strength of the chemical modifiers.

In order to obtain the desired final product a good rule has been summed up in terms of the hydrolysis and condensation reaction.

Table 4-2. Product obtained according to the relative rates of hydrolysis and condensation [98].

Hydrolysis Rate	Condensation Rate	Result
Slow	Slow	Colloids/sols
Fast	Slow	Polymeric Gels
Fast	Fast	Colloidal Gel/Gelatinous Precipitate
Slow	Fast	Controlled Precipitation

It suggests that, depending on the relative hydrolysis and condensation rates, different final products can be obtained.

Acetylacetone is known to be a rather strong chelating ligand and many metal β -diketonates have already been reported in the literature [99]. The enolic form of β -diketones contains a reactive hydroxyl group which react readily with metal alkoxides. Therefore, acetylacetone has often been used as a stabilizing agent for metal alkoxide precursors to improve the process. Recently, TiO_2 colloids have been stabilized up to high pH with acetylacetone [100]. The structural investigations of the colloids of titanium oxide prepared from the modified alkoxide were conducted using X-ray absorption near edge spectroscopy (XANES) and extended X-ray absorption Fourier spectroscopy (EXAFS) [101]. It was shown that the coordination number of titanium increases from four ($\text{Ti}(\text{OPr})_4$) to five ($\text{Ti}(\text{OPr})_3\text{acac}$) by the modification with acetylacetone, then to six with oligomeric species formed during the dilution with ethanol. The acetylacetone modification process for titanium isopropoxide followed by dilution with ethanol is schematically depicted in Figure 4-7 or page 89. Through the acetylacetone modification, titanium

isopropoxide is transformed to a more stable complex against hydrolysis in contrast to that without modification.

According to the "rule" depicted in Table 4-2 the composite particles were obtained in the microemulsion matrix by controlling relative rate of hydrolysis and condensation reaction of titanium isopropoxide precursors. The results have shown that the control of particle size, size distribution and especially particle aggregations is much more difficult than with the relatively slow-reacting silicon alkoxide. Even under the chemical modification of metal alkoxide precursors, the hydrolysis rate is difficult to control and sometimes aggregation of particles into irregular flocs occurred after a short reaction time. Figure 4-14a shows the resulting composite particle synthesized using modified titanium isopropoxide through reverse micelles under acidic conditions. The TEM image photomicrograph reveals the composite structure of the core and the shell. Moreover, the transparent-gel containing the nanometer-sized semiconductors has been obtained. In contrast, under basic condition the resulting particles tend to aggregate (Figure 4-14b). Current work seeks to manipulate the microemulsion formulation, organometallic precursor modification, and the behavior of additives such as acid or base in the reaction matrix in order to achieve condensation and particle growth in a controlled manner. The gelation of transition metal oxides in the microemulsion matrices is a new area which shows promise in the areas of energy conversion, special catalysis, and photochemical applications. The experimental results show that in the chemical modification gelation of the transition metal oxide inside the microemulsion can be controlled and results in an inorganic-organic hybrid gel.

4.4.5. Optical Characterization and Size Quantization Effects

Optical-absorption spectra (Figure 4-15a) collected at room temperature for CdS quantum dots at various size indicated the lowest exciton energies and gave a qualitative idea of the size distribution. The most striking features are as follows: first, the spectra of

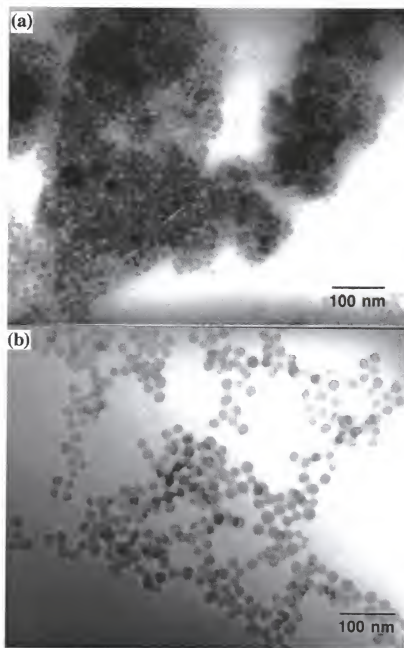


Figure 4-14. TEM microphotographs of the CdS/TiO₂ nano-composite synthesized from Igepal-cyclohexane-water system with modified titanium isopropoxide precursors ($R=5$, $H=200$, $X=1$) under different conditions: (a) acidic condition, and (b) basic condition.

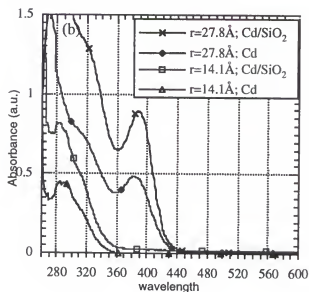
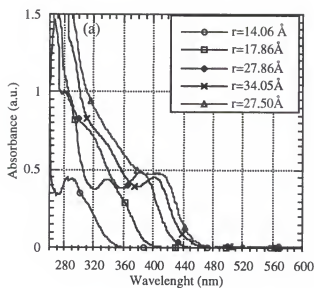


Figure 4-15. (a) Absorption spectra of CdS clusters having different sizes, and (b) comparison of absorption spectra between CdS clusters and their nano-composites.

the nanometer-sized particles stabilized by anionic surfactant (AOT) show a well-developed maximum near the onset of absorption which is ascribed to the first excitonic (1s-1s) transition. In some cases even higher energy transitions are observed. Second, with decreasing particle size the transition energies shift to higher values as a consequence of the size quantization effect. Third, the absorbance of each sample was enhanced when the quantum dots were further capped by SiO_2 [Figure 4-15b].

Absorption spectra directly reflect the electron energy spectra of quantum-sized semiconductor clusters. In a bulk semiconductor, the electron and hole are bounded by the screened Coulomb interaction with a binding energy of a few to tens of millielectronvolts. This exciton is easily ionized with thermal energy, which accounts for the absence of a strong exciton absorption band in bulk semiconductors at room temperature. By confining the electron and hole in a small cluster, the binding energy as well as oscillator strength can increase due to the enhanced spatial overlap between the electron and hole wave functions and the coherent motion of the exciton.

Several theoretical models have been developed over the past decade to calculate the size-quantization effect on the electronic energy structure. Each method has its particular strengths and weaknesses. The simplest model used to predict the optical properties of the microcrystallites considers the effect of boundaries on the electron and hole wave functions of a bulk crystal; the localized wave functions are envisioned as wavepackets built up from infinite crystal single-electron Bloch wave functions. Thus the starting point for the model is the standard effective mass approximation (EMA) used in semiconductor physics. The Hamiltonian governing the envelope function of the localized electrons and holes is expressed as

$$H = -\frac{\hbar^2}{2m_e\Delta_e} - \frac{\hbar^2}{2m_h\Delta_h} + V(r_e) + V(r_h) - \frac{e^2}{\epsilon|r_e - r_h|} \quad [4-7]$$

where the subscripts e and h refer to the electron and hole coordinates, respectively, $V(r_i)$ is the potential experienced by the localized electron and hole, m_i is the electron or hole effective mass, ϵ is the low-frequency dielectric constant, and the last term represents the

electron and hole Coulomb interaction. The changes of the energy spectra resulting from quantum confinement can be illustrated in a very simple way in the scheme shown in Figure 4-16a. Efros and Efros [102] considered the solution of Schrodinger's equation for the Hamiltonian of Equation [4-7] in two extreme situations by assuming that the surrounding medium for the microcrystallites can be modeled as an infinitely deep spherical potential well. In the first case, the energy of electron and hole confinement ($\sim \hbar^2 / m_i r^2$) was assumed dominant relative to the Coulomb interaction energy ($\sim e^2 / \epsilon r$), where r is the crystallite radius. This results in a splitting of both the valence and conduction bands into a series of subbands consistent with what one would expect for a particle in a box. The energy shift of the electron and hole subbands relative to the bulk crystal band edge is obtained by expressing Eq.[4-7] in spherical coordinates. Ignoring the Coulombic term and imposing the infinite potential-well boundary condition, yields the characteristic equation for the electron and hole envelope functions,

$$J_{l-1/2}(\sqrt{2m_i E} / \hbar^2 r) = 0 \quad [4-8]$$

where l is the orbital angular momentum quantum number of the state. For each value of l , an infinite but discrete set of energy shift eigenvalues are obtained, characterized by the radial quantum number n . The energy of the J th optical transition involves shifts of both the electron and hole subbands given by

$$E_g + (\hbar^2 / 2\mu r^2) X_j^2$$

$$X_1 = 3.142, X_2 = 4.493 \quad [4-9]$$

where μ is the reduced electron-hole mass, E_g is the bulk crystal band gap, and values of X_j for the two lowest energy transitions are given. The lowest energy transition is between the $n=1, l=0$ hole state and $n=1, l=0$ electron state while the next transition involves $n=1, l=0$ and $n=1, l=1$ states. The selection rules for optical transition are broken.

In the second case treated by Efros and Efros, the Coulombic energy was assumed to be dominated with the result that the lowest energy state is an exciton with its energy

shifted due to the confinement. The exciton radius is considered sufficiently small relative to the crystal radius to permit a separation of Eq.[4-7] into center of mass and internal coordinates, yielding a hydrogenic type wave-function solution.

Brus [103] treated Eq.[4-7] in a manner more appropriate to CdSe and CdS glass since the crystallite size and the exciton radius can be comparable. The calculation includes the Coulombic interaction as a perturbation and the lowest energy electronic transition is shifted relative to the normal band gap by the amount ΔE :

$$\Delta E = \frac{\hbar^2 \pi^2}{2\mu r^2} - \frac{1.8e^2}{\epsilon r} - 0.248 E_{Ry}^* \quad [4-10]$$

where E_{Ry}^* is the effective Rydberg energy. The first term again represents the particle-in-a-box quantum localization energy and has a simple $1/r^2$ dependence, the second term represents the Coulomb energy with a $1/r$ dependence, and the third term is a result of the spatial correlation effect. This last size-independent term is usually small but can become significant for semiconductors with small dielectric constant.

Although the effective mass approximation contains the basic physics of the quantum size effect. It can not be expected to be quantitatively correct, especially for very small clusters (i.e., in the strong confinement region). This can be understood from the band-structure scheme. In the effective mass approximation the highest valence band and the lowest conduction band are assimilated closer to the extrema ($k=0$) to parabolic curves of the form $\frac{\hbar^2 k^2}{2m^*}$, where k is the amplitude of the wave vector. As k increases, this expression varies more steeply than the true dispersion relation [Figure 4-16b]. Consequently, the exciton peak position will be over estimated in comparison with the true value for small clusters in the strong confinement region. Furthermore, the effective mass approximation is not rigorous enough for valence states. The materials under consideration have a complex valence-band structure with three subbands [Figure 4-17]. Respective holes behave like particles of spin $3/2$ or $1/2$. Outside $k=0$ they are coupled by effective

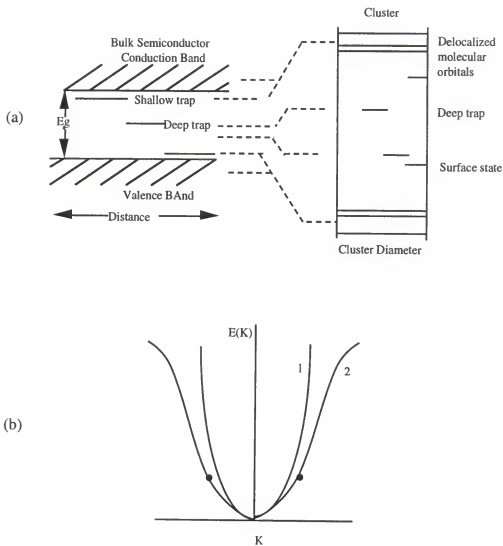


Figure 4-16. (a) Schematic correlation diagram relating cluster states to bulk crystal states [103]. (b) $E(k)$ diagram: curve 1, case for parabolic band; curve 2, true energy band which is parabolic only near $k=0$; (\bullet), two eigenvalues for the first excited state [14].

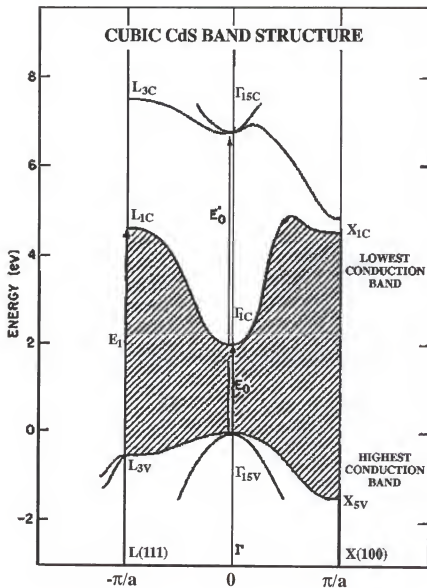


Figure 4-17. Partial band structure diagram of cubic crystalline CdS. The lines labeled $L(111)$ and $X(100)$ refer to different directions within the unit cell. [103]

spin-orbit interaction and should be treated in a multiband envelope-function model with Luttinger-Kohn effective mass parameters [104].

A better description of the band structure can be obtained from a tight-binding framework in the strong confinement region. In this region the size of the microcrystallites is closer to the molecules, thus one may seriously question whether a concept based on long-range crystalline order is still meaningful and whether a molecular or cluster picture is more appropriate. Since the atomic structure is implicitly considered, the tight-binding method is more adequate for small crystallites. Lippens and Lannoo [105] have used the tight-binding method to calculate the energy levels for clusters of wide-bandgap semiconductors such as cubic CdS clusters (Figure 4-17). By using a recursion method and restricted interactions to first-nearest neighbors to reduce computing time, the results for the clusters small enough to fit into the strong confinement region agree well with experimental data.

Figure [4-18] presents the size-dependent energy spectra of CdS clusters compared with the different theoretical results calculated from effective mass approximation (EMA)[106] and the effective tight-binding approximation (EBTM) [107]. Comparison between the experimental data and the theoretical results reveals that the effective mass calculation gives a good agreement for the cluster with diameter, d , equal to or larger than the two times of the bulk exciton Bohr radius ($a_B \approx 35 \text{ \AA}$ for CdS). However, this agreement fails as the diameter of the cluster decrease ($a_B > r$), and the effective tight-binding method gives better results. Similar results have been reported by several author [108].

The luminescent properties of CdS clusters and surface-modified CdS (CdS/SiO_2) clusters were examined by steady-state photoluminescence spectroscopy at both room temperature and 4 K. It is difficult to quantitatively interpret the experimental results due to the complicity involving interfacial states between the clusters and matrix, impurity levels, and defects inherent to the processes. However, the general tendency resulting from the

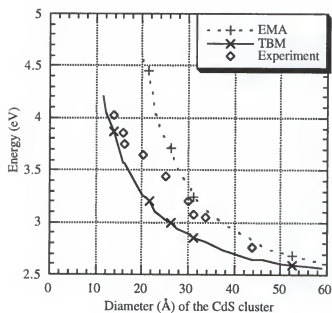


Figure 4-18. Size dependence of the first excitonic transition, comparison between experimental results with the theoretical calculations. The results of EMA are obtained from equation [4-10] and the results of TBM are adopted from Lippens and Lannoo[105].

size-quantized effects has been revealed by the PL spectra. As the size of the clusters decrease, the luminescence peak moves to higher energy, following the absorption spectra [Figure 4-19a]. It has been speculated that the broadening of the luminescence spectra and low quantum yield were attributed to the size-inhomogeneities and the recombination of charge carriers immobilized in traps of different energy. As the cluster size decreases, the HOMO-LUMO gap opens up, which makes certain defect states energetically accessible [109]. The luminescence spectra of the SiO₂ surface-modified CdS clusters show more features than that of colloidal CdS. The energy of the short-wavelength luminescence peak agrees closely with the onset of absorption spectra with a slight red shift, indicating that the origin of this emission is a direct electron-hole recombination or, at least, emission from shallow trapping levels very close to the respective band edges (Stoke-shift) (Figure 4-19a). It is interesting to note that the intensity of the absorption spectra of the surface-modified CdS clusters is stronger than that of non-surface-modified CdS clusters (Figure 4-19b). These results indicate that the SiO₂ surface modification provides a passivating agent for removing surface defects of CdS. So far, identification of the low energy emission peaks of the surface-modified clusters was unsuccessful. Difficulties arise from the surface and matrix influences and intrinsic defects. Teubner [110] suggests that the increase in the intensity of the orange-red emission in CdS-doped silicate glasses, relative to CdS sols, arise from the presence of excess Cd²⁺ ions which increase the number of S²⁻ anion vacancies (the origin of a radiation center), and from less passivation of the surface defect sites by the silicate host atoms.

4.5. Conclusions

Nano-composite CdS/SiO₂ quantum dots with surface-modification through the hydrolysis and condensation of organometallic precursors such as tetraethoxysilane (TEOS) and titanium (IV) isopropoxide in microemulsions have been successfully

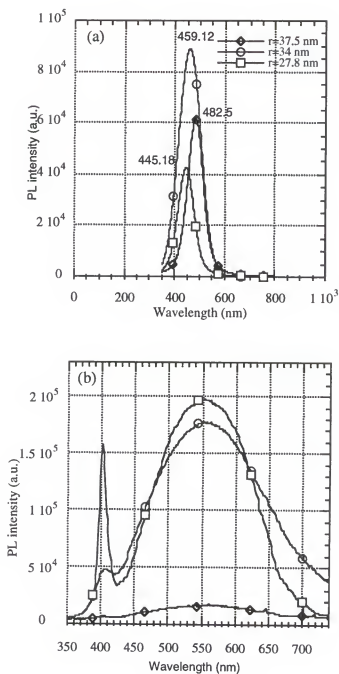


Figure 4-19. Photoluminescence spectra of the CdS cluster and its nano-composites. (a) PL spectra as a function of the particle radius, and (b) PL spectra of CdS nano-composites at 4 K (square) and CdS cluster (circle), and room temperature LP spectra of CdS nano-composites (diamond)

synthesized. The nanometer-sized quantum dots grown by temporally discrete homogeneous nucleation in combination with reverse micelles have a narrow size-distribution and well-defined crystallinity. It was demonstrated that by adjusting the processing parameters such as the ratios of water to surfactant, water to organometallic precursor, and amount of catalyst, the size and the size distribution of the nano-composites can be controlled. Furthermore, a chemically modified titanium precursor allows one to control the relative rate of the hydrolysis and condensation and different final products of the nano-composites with core-shell structures or transparent-gel doped with quantum dots can be obtained.

Optical characterization of the surface-modified quantum dots show strong quantum confinement effects indicated by well-resolved exciton transition and emission from both absorption and luminescence spectra. Surface-modification provides an effective passivating agent to the surface states of the CdS clusters and therefore gives strong absorption and luminescence intensities. The experimental data of the size-quantization of the CdS clusters were compared with the theoretical results of the effective mass approximation and tight-binding method. The agreement and the deviation of the experimental results with the theoretical prediction reveal the strength and weakness of each theory.

CHAPTER 5 SYNTHESIS OF Ag/SiO₂ NANOMETER-SIZED COMPOSITE PARTICLES

5.1. Introduction

The investigation of the physicochemical properties of finely dispersed metals, which Faraday used to call colloidal solutions of metals, date to at least the past century. The earliest, but perhaps not the first interest in these colloids is the use of metal particles as catalysts in photochemical and radiation chemical reactions [111]. The motivation for recent research of colloidal metal particles has been focused on the unique electro-optical and electrochemical properties similar to the recent development of nanometer-size semiconductors [112]. There are no basic differences between semiconductor and metal particles. Many effects which have been found for semiconductor particles, such as their ability to store excess electrons and holes, changes in electronic properties upon surface modification, photoelectron emission, and sensitization of photoreactions of other solutes, are also observed in metallic colloids.

Optical properties of metal particles with dimensions much smaller than a wavelength are interesting and have been accorded attention by a large number of physicists. Since such a small particle is necessarily surrounded by a dielectric metal oxide passivation layer, one unavoidably deals with a composite material made of small metal particles embedded in a dielectric. The interface between the metal and dielectric leads, through the surface-plasma resonance, to the dielectric anomaly that is the origin of the beautiful colors of metal colloids. It was also observed more recently that the width of the absorption band of the metal colloids, which is roughly proportional to the imaginary part of the susceptibility, increases when the size of particles decreases [113]. This effect was

accounted for classically in terms of a limited mean free path, or quantum mechanically in terms of the quantum confinement [114].

The first experimental study of the nonlinear optical properties of such metal colloids was reported by Ricard et al. in 1985 [28]. It was observed that optical phase conjugation in these media is very strongly resonantly enhanced near the surface-plasma resonance frequency. Since composite materials are macroscopically isotropic, their nonlinear response is mainly due to the third order Kerr effect, which is well suited to study optical nonlinearities and, furthermore, is closely related to important applications such as real-time holographic and bistable memory devices, optical correlators, phase-conjugator devices, optical polarizers, etc. [115]. In the past few years, several authors including Neeves, Flytzanis and Haus [30-31] proposed theoretical calculations of the nonlinear-optical behavior based on the model composites of nanospheres with a metallic core (e.g., Ag and Au) and nonlinear shell (e.g., CdS) or with a nonlinear core and metallic shell suspended in a nonlinear medium. Optical phase conjugation is shown to be enhanced from each nonlinear region because the optical field can be concentrated in both the interior and the exterior neighborhoods of the particle and magnified at the surface-mediated plasma resonance. However, so far there are no such composite model particles in practical available to verify these theoretical predictions.

Surface coating or surface modification of nanometer semiconductor and metal particles offers a new challenge to synthesis. Interest in these materials is partially motivated by the development of optical properties that mimic the superior performance characteristics of atoms or molecules. Furthermore, control over the coating thickness gives a further engineering degree of freedom to elucidate the underlying physics of these structures. For example, by changing the thickness of the shell and the particle radius, the overlap of the wave functions and the band gap can be changed [116]. The physical parameters of each material as well as the interface between the "heterostructures" will have a great influence on the optical properties [117].

Besides unique optical properties of metallic clusters, there are important applications of small metal particle technology to a number of areas: heterogeneous catalysis, surface enhanced Raman scattering, fields of research where surface and interface properties are important such as in heat exchangers and thermometers at ultralow temperatures, magnetic devices, and superconductivity, to many but a few. In many of these applications the essential properties are specifically a consequence of the small size and do not exist in the bulk material at all. Thus, the processes of making metal clusters with narrow size distribution are critical in order to reveal and furthermore to apply these properties in practical applications.

A wide variety of methods have been used to prepare such small clusters including hydrosols, impregnation/chemical reduction and ion exchange/chemical reduction, inert gas evaporation, vacuum evaporation, nucleation of metal clusters by irradiation and microlithography. For example, in the hydrosol method an acid solution of the appropriate metallic element is first prepared. A reducing agent, usually sodium citrate, is rapidly mixed with the solution to produce a suspension of particles. Dialysis can be used to remove the remaining ions and then a protective agent such as gelatin is normally introduced to ensure that the resulting particles are well dispersed. Noble metal particles including silver [118], gold [119] and platinum [120] have been prepared in this way. Another powerful chemical method, impregnation/chemical reduction, uses a support matrix with very high specific area and restricted pore size (typically less than 1 nm) within which chemical reduction of metal salt can be performed. Customarily, the reduction is effected with hydrogen gas at elevated temperature. In this method an aqueous solution containing the metallic element is prepared and impregnated into the porous space of a support such as SiO_2 or Al_2O_3 . For instance, in the case of Pt this could be a solution of H_2PtCl_6 [121] or for Pd one might use PdCl_2 or $\text{Pd}(\text{NH}_3)_4$ [122]. Similarly, particles of many other metallic elements have been made such as Na, Ca, Cu, Ag, Ta, W, Au, and Ti, to name a few. The support material, impregnated with solution, is usually dried and

then heated in air, a process referred to as calcination. Then it is chemically reduced to the metallic state in flowing hydrogen at a temperature between 250 °C and 450 °C. A final step of heat treatment in a flowing helium gas stream at a somewhat higher temperature is frequently used to ensure that metal surface is cleansed of chemisorbed hydrogen.

It is apparent that there is not a universally adequate method for production of particles applicable to every element and every application. In many cases the preparation methods must be designed in order to meet the specific requirements of application. This chapter demonstrates a unique method to prepare the nano-composites of Ag/SiO₂ inside a microemulsion reaction matrix in conjunction with hydrolysis of organometallic precursors such as tetraethoxysilane (TEOS), followed by condensation reaction in the water nanodroplets to form a coating layer onto the surface of the nanosize metal in reverse micelles. It is believed that not only metal/silica nano-composites, but semiconductor/oxide and even semiconductor/insulator/metal multiple layer heterostructures can also be able to be prepared using this method.

5.2. Materials and Experiment

The new approach utilizes water-in-oil microemulsion (reverse micelle) where the Ag particles are synthesized by reduction of Ag⁺ ions, in situ, in the reverse micelles, followed by hydrolysis and condensation of tetraethoxysilane (TEOS) inside the reverse micelles to perform a coating layer on Ag nanosize particles.

Reverse micelles were prepared from both ionic and nonionic surfactants using the procedures similar to those of Osseo-Asare [89]. The anionic surfactant used to form reverse micelles was sodium bis(2-ethylhexyl) sulfosuccinate, usually called Aerosol OT or AOT, from Aldrich Chemical. The nonionic surfactant Igepal CO-520, poly(oxyethylene) nonylphenyl ether, was also from Aldrich Chemical. Both surfactants were used without further purification. Additional chemicals, such as Ag(NO₃)₃ (Aldrich Chemical Co.), tetraethoxysilane (TEOS, 99% Fisher Scientific Co.), cyclohexane (Fisher Scientific Co.),

isooctane (Fisher Scientific Co.), ammonium hydroxide (29% Fisher Scientific Co.), were used as received. Water was deionized in our laboratory greater than 8 M Ω /cm.

The general procedure used to prepare Ag/SiO₂ nano-composites is schematically shown in Figure 5-1. Although different detailed recipes have been used for each preparation, a typical recipe was 20 ml of a microemulsion prepared at ambient temperature in a 30 ml vial with rapid stirring. The microemulsion solution contains 4 ml Igepal, 10 ml cyclohexane and 1.64 ml of 10⁻² M Ag(NO₃)₃ solution. The amount of aqueous solution was added in accordance with the different molar ratio of the water to surfactant, $R=[\text{water/surfactant}]$. The radius of the water pool can be changed by varying the R to control the size of the resulting particles. The silver aqueous solution was added using a syringe. The microemulsion was mixed vigorously with rapid stirring. After 5 minute equilibration, one drop of hydrazine hydrate as a reducing agent (N₂H₄·xH₂O) was added to the solution. The suspension changed from a lighter golden brown to darker in color. After another 5-10 minute equilibration, the TEOS stock solution was injected into the microemulsion. The amount of TEOS injected was varied according to different molar ratios of the water to surfactant, $H=[\text{water/TEOS}]$. In order to facilitate the ease of processing the microemulsion reaction matrix, a tetraethoxysilane (TEOS) stock solution containing 50% TEOS and 50% cyclohexane by weight was prepared to ensure the homogenous dispersion of the TEOS in the microemulsion reaction matrix. To expedite the condensation reaction, base as NH₄(OH) was injected into the stirred microemulsion. The amount of base added was monitored through another ratio: $X=[\text{NH}_4(\text{OH})]/[\text{TEOS}]$. This ratio is specifically for the purpose of consistency, as the pH is measured independently in the organic solvent.

The structure, size, and morphology of the resulting composite particles were examined by transmission electron microscopy (TEM), X-ray diffraction (XRD) and X-ray photoluminescence spectroscopy (XPS). In the TEM study the sample was prepared by dropping a freshly prepared cluster solution on a carbon film supported on a Cu grid. The

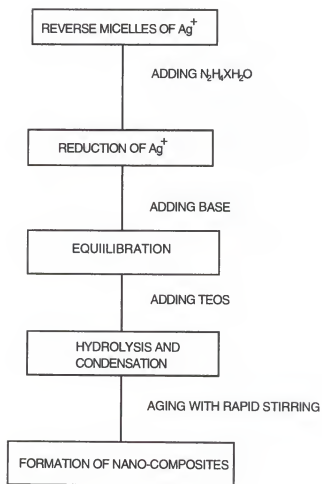


Figure 5-1. Schematic diagram of the synthesis procedure used to produce Ag/SiO₂ nano-composite

mean diameter and standard deviation of the clusters were determined from the obtained micrographs by averaging the measured diameter of 50 and 100 particles.

A series of absorption spectra was taken as a function of reaction time to monitor the hydrolysis and condensation processes with respect to changes of the optical intensity. UV-visible spectra was also used to study the size-effects on these nanometer-sized metallic clusters.

5.3. Results and Discussion

Spherical Ag/SiO₂ nanometer-size composite particles with narrow size distribution have been obtained with reduction of metallic element in reverse micelles followed by *in-situ* hydrolysis and condensation in the microemulsion. Preparation of nanosize composites from microemulsion proceeded through various stages different in both nature and kinetics. While the core particles are formed by homogeneous nucleation and growth, the shells are likely formed through heterogeneous nucleation and growth. Because the two steps are different in mechanism, controlling the formation of the nano-composites is very sensitive to modest processing changes.

5.3.1. Formation of Ag colloids

5.3.1.1 Effect of ratio of the water to surfactant on particle size and distribution

Most details of the studies of the Ag nanosize particle formation process in reverse micelles have been reported based on the two step model [123]: A rapid first step is complete reduction of the metal to the zero valance state. The second step is the growth, via reagent exchanges between micelles through the inter-micellar exchange. The nucleation and growth of Ag particles are likely to be a diffusion-controlled process through inter-micellar interaction, but can be influenced by many other factors such as phase behavior and solubility, average occupancy of reacting species in the aqueous pool,

intra-micellar interaction, nature of solubilized water and parameter R, and dynamic behavior of the microemulsion [56].

Thus, special attention has been paid to control the ratio of water to surfactant, R, to select solvent and the concentration of the reagent in order to control the size and optimize the size distribution of the resulting particles. Optical spectra and transmission electron microscopy have been used to determine the size and size distributions of the metal particles resulting from variations of these experimental parameters. Figure 5-2 shows the absorption spectra of colloidal silver particles obtained in the reverse micelles from the Igepal-cyclohexane-water system at various R, whose size was independently determined by TEM. These spectra are characteristics of metallic silver particles with a surface-plasmon resonance centered around 400 nm, slightly varying with the particle size. It was found that at low R, the surface-plasmon resonance peaks in the absorption spectra of the small Ag particles were broad with a low optical intensity. The electron diffraction pattern in Figure 5-3 indicates a crystalline face-center-cubic (fcc) structure with a lattice constant of 4.08 Å. Upon increasing R, the surface-plasmon resonance peak around 400 nm progressively became narrow and more intense with a slight red shift, which can be correlated with the size of the particles [30] and will be discussed in detail in Chapter 6. The change of R has an influence on the distribution of the resulting particles. It can be noticed in Figure 5-4, that as R increases above 10, the size of metallic cluster remains unchanged but the size distribution of the resulting particles becomes more polydispersed due to the increase of kinetic instability of the reverse micelles with the increasing R. The results consistent with the above observation were obtained by several other authors [30, 56]. A uniform size distribution can only be obtained when R is below 10 in both the Igepal as well as AOT systems.

5.3.1.2. Effect of the reagents

While increasing ion concentrations, the increase of the size of the resulting particles has been observed by change in the optical absorption spectra of the colloidal

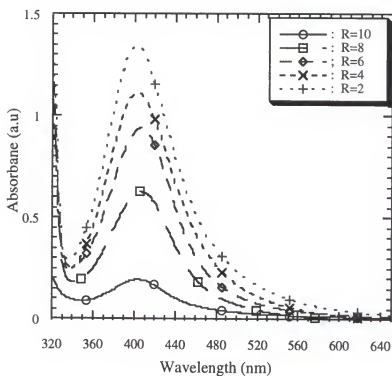


Figure 5-2. Absorption spectra of Ag metal clusters formed in Igepal-cyclohexane-water reverse micelles at various water content (R).



Figure 5-3. TEM micrographs of Ag clusters synthesized in Igepal-cyclohexane-water reverse micelles: (A) TEM micrograph of Ag clusters with $R=2$; and (B) diffraction pattern taken from the same sample.

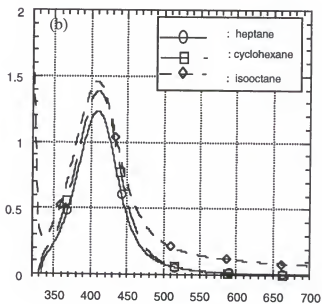
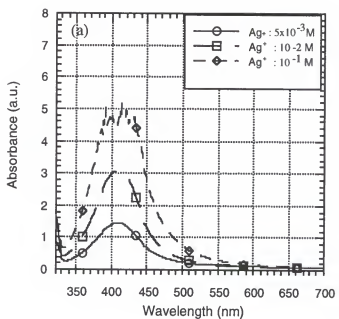


Figure 5-4. a: Absorption spectra of the Ag clusters at various salt concentration. b: Absorption spectra of the Ag clusters at various solvent

suspensions (Figure 5-4a). Increasing the concentration of Ag^+ from $5 \times 10^{-3} \text{ M}$ to 10^{-2} M , the absorption spectrum becomes narrower and more intense, which indicates that the size of the silver particles has been increased. This change in the spectrum can be explained in terms of the classical mean free path effect and size-quantized theory [114].

The ionic strength and the concentration have a great influence on the formation and the stability of the microemulsion systems [73]. Compared with the ionic surfactant, the nonionic surfactants are relatively insensitive to changes in the electrolyte concentration [124]. In nonionic surfactant systems (Igepal-cyclohexane-water), as the salt concentration increases from 10^{-3} M to 10^{-2} M , the suspensions of the microemulsions can stand for several days without sedimentation occurring. However, the suspensions can only remain stable for several hours in the anionic, AOT-isooctane-water anionic microemulsion.

5.3.1.3. Solvent effect

Figure 5-4b. presented the changes of absorption spectra of Ag particles with increasing chain length of apolar solvent. The enhanced intensity in the absorption spectra with increasing solvent chain length indicates the increase in the size of the resulting particles due to the changes in the process of particle growth. It is well known that the inter-micellar exchange process is governed by the attractive interactions between micelles, which vary as a function of chain length of the hydrocarbon solvent, temperature, and radius of the micelles [125]. The attractive potential of micelles will be enhanced by increasing the length of hydrocarbon chain of the bulk solvent. Consequently, the intermicellar exchange rate constant K_{ex} will be increased. Thus, to further control the particle size, a series of experiments was conducted with variation of the bulk solvent in the sequence of the cyclohexane, heptane, and isooctane. The results indicate that for example, replacing cyclohexane by isooctane induced a increase in the intermicellar exchange rate constant from $K_{\text{ex}}=10^6 \text{ M}^{-1}\text{s}^{-1}$ to $K_{\text{ex}}=10^7 \text{ M}^{-1}\text{s}^{-1}$ [96]. Hence, the size of the resulting particles will increase due to the enhanced intermicellar exchange rate.

5.3.2. Formation of the Composites

Formation of the thin layer of SiO_2 onto the Ag cluster was achieved by *in situ* hydrolysis and condensation of metal alkoxide precursors of tetraethoxysilane (TEOS) in reverse micelles. To control the thickness and uniformity of the SiO_2 layer a variety of processing parameters such as the ratio of the water to surfactant, R, the ratio of the water to the metal alkoxide precursors, H, and the amount of base added to enhance the hydrolysis and polycondensation (referred to the ratio of TEOS to base, X) have been paid special attention. The size and size distribution of the resulting nanometer-sized composites were quantitatively characterized by electron microscopy. Optical properties of these nanocomposites were characterized by linear and nonlinear optical spectroscopes.

5.3.2.1. Particle characteristics

The TEM micrographs and histograms presented in Figure 5-5 and 5-6 show that the resulting Ag/ SiO_2 nanosize composites are essentially monodisperse and spherical in shape. The size of the composite particles shows a linear increase as the R and H ratio increases. The thickness of the coating layers can be controlled through varying the molar ratio of water to TEOS (H). Figure 5-7 shows the increasing thickness of the coating layer on the Ag nanosize core as the ratio of the water to TEOS (H) increases while the size of the cores are barely changed (R=constant). To determine the median size and standard deviation, t values were collected from the Standard Mathematical Tables for normal distributions [126]. Subsequently, a linear regression was performed on the plot of log normal probability of particle size on the y-axis against the t-values on the x-axis in the range of cumulative percentage from 15% to 85%. From the obtained linear equation the Ag/ SiO_2 nano-composites have a median diameter from 12.5 to 35 nm with ± 0.25 nm standard deviation as a consequence of the variation of the H ratios from 100 to 300 at R=4. TEM diffraction pattern of the resulting Ag/ SiO_2 nano-composite particles shows

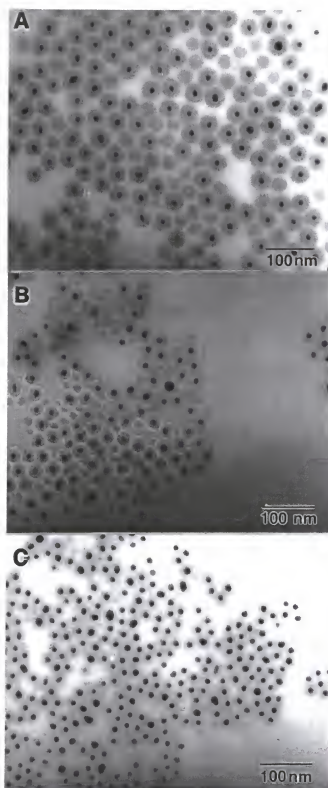


Figure 5-5. TEM micrographs of Ag/SiO₂ nano-composites formed in Igepal-cyclohexane-water system at R=4, X=1, and various H ratios: (A) H=100; (B) H=200; and (C) H=300.

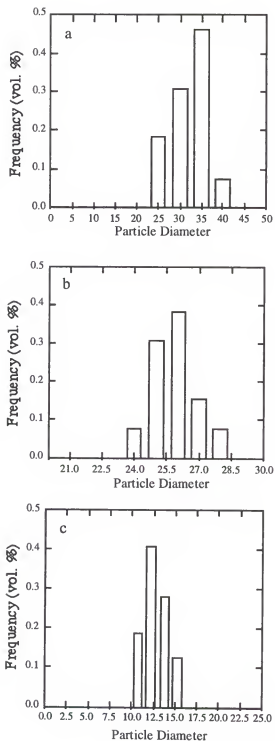


Figure 5-6. Histogram of the Ag/SiO₂ nano-composites synthesized at R=4, X=1, and different H: (a) H=100; (b) H=200; and (c) H=300.

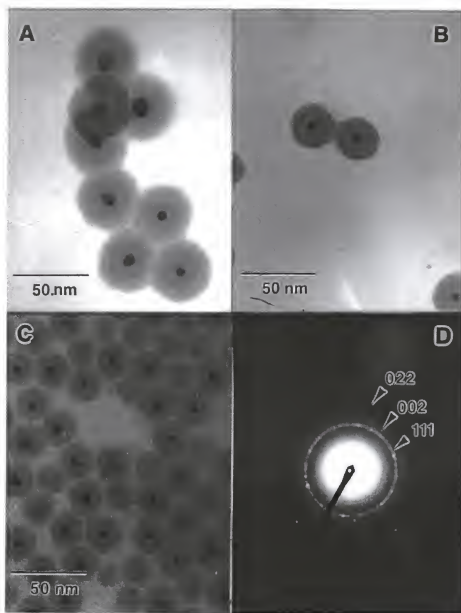


Figure 5-7. TEM micrographs of Ag/SiO₂ nano-composites at the constant of $R=6$ and $X=0.75$, and different H : (a) $H=100$; (b) $H=200$; (c) $H=300$; (d) Diffraction pattern of the nano-composites.

that the Ag core has a face-centered cubic crystal structure (Figure 5-7d). In addition, the presence of the surfactant allows the formation of a remarkably ordered particle arrangement upon volatilization of the solvent. Similar film-like aggregates formed by the presence of surfactant molecules have been described by Alexander and Iler [127] for silica sols and by Akasy [128] for a suspension of colloidal gold particles. As suggested by Alexander and Iler the negative charge of the silica particles under alkaline conditions induces growth of the aggregate (i.e., particle attachment) only around the edges of the monolayer of particles where ionic repulsion is least.

The results in Figure 5-8 present the effects on the resulting particles as changing the water content, R , when the TEOS and the ratio of TEOS to catalyst, X , were kept constant. At low water content most of the water was bound to the hydrophilic head group of amphiphilic molecules and the rate of hydrolysis of the TEOS was slow. Consequently, the thickness of the oxide layer increased slowly. As the R ratio increases, more free water inside the reverse micelle was available for the hydrolysis reaction of the TEOS, resulting in thicker or a larger size of the SiO_2 layer. The changes of the oxide layer thickness as a function of R and H ratios have been plotted in Figure 5-9a. It was also found that at the low water content the size distribution of the resulting particles remained fairly narrow and increased linearly with the R . However, as increasing the water content close or above $R=10$, the particle size increased and the size distributions of both core metal and oxide layer became polydisperse Figure 5-9b because reverse micelles become unstable and more polydispersity as increase water content [129]. It is worth mentioning that the same results have been reported by Guizard et al. [129] in the hydrolysis of Ti and Fe alkoxides in a non-ionic surfactant (a polyoxyethylene alkylphenylether)-decane-water reverse micellar system. This deviation could be due to the inter-micellar collisions which result in a larger micellar-size distribution with the increasing R , or due to the temperature sensitivity of the nonionic surfactant.

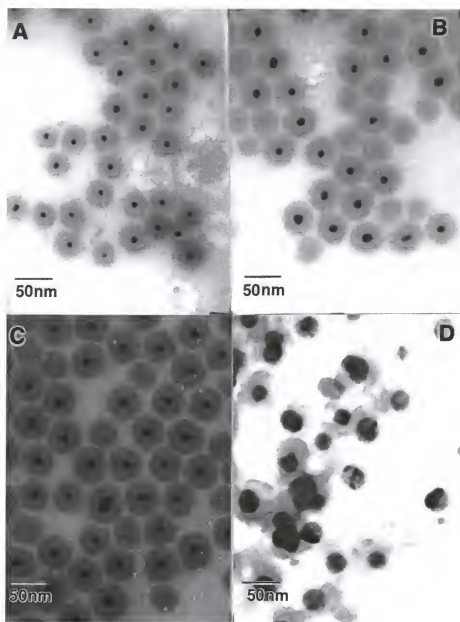


Figure 5-8. TEM micrographs of Ag/SiO₂ nano-composites synthesized at the conditions of X=1 and H=100, and different water content: (a) R=2; (b) R=4; (c) R=6; (d) R=10.

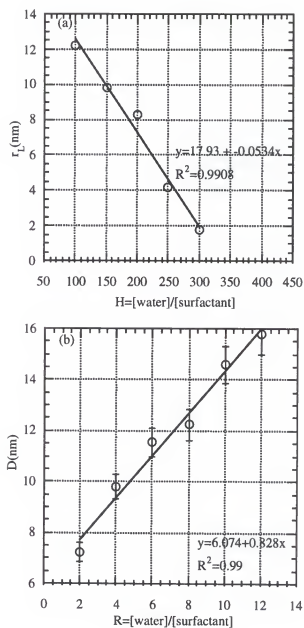
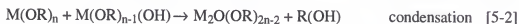


Figure 5-9. (a): Variations of the thicknesses of SiO_2 layers (r_L) as a function of the H at the conditions of $R=4$, $X=1$. (b): The size of the Ag clusters changes with the R ratio changing.

To control the relative rate of hydrolysis and condensation reactions and to obtain a stable suspension, the amount of base added was monitored by the ratio of the base to TEOS, depicted as X. It was found that the microemulsion became unstable and the resulting particles became more polydispersity as X increased when other parameters such as R and H were kept constant. A stable suspension could only be obtained when X was close to 1, with the suspension flocculated when the X was further increased.

5.3.2.2. Mechanism of the composites formation

The basic formation mechanism of the Ag/SiO₂ nano-composites is the same as that of CdS/SiO₂ nano-composite particles described in the Chapter 4. As in an alcoholic solution of water and bases such as ammonia, metal-organic derivatives within the microemulsion reaction matrix are also undergoing a hydrolysis reaction and the two possible condensation reactions, which can be represented as follows [89]:



As a first approximation, it may be assumed that the reverse micellar aggregates present in the solution are not affected by the addition of TEOS molecules nor by the subsequent reactions, and in particular that the aggregation numbers (micellar concentration) remain unchanged. Under these assumptions, the TEOS alkoxide molecules interact quickly with the water molecules inside the reverse micellar aggregates, forming partially hydrolyzed species. Once formed, these hydrolyzed species remain bound to the micellar aggregates due to their enhanced amphiphilic character (brought about by the formation of silanol groups). In this case all further reactions are restricted to the locale of the micellar aggregates, and thus the overall mechanisms of oxide layer formation and growth involve both intra and inter-micellar events [89]. On this basis, it is likely that hydrolysis may occur in each reverse micelle (basically an intra-micellar process). On the other hand, condensation (particle growth) may occur within a given micelle or by inter-micellar

contacts. Therefore, formation and size of the composite particles depend on the relative rates of the hydrolysis and condensation reactions. Figure 5-10 shows the UV-visible absorption spectra obtained during hydrolysis of $1 \times 10^{-4} \text{M}$ TEOS for various R values. The changes in the absorption bands was used to qualitatively monitor the relative rate of hydrolysis and condensation. The results again support the hypothesis proposed in chapter 4 (and schematically described in Figure 4-12, 13): the rate of the hydrolysis decreases as the R ratio decreases. With low water content (small R ratio), most of the water molecules are bound to the polar head of the surfactant molecules. Thus, the hydrolysis rate is slow. With increasing water content (R ratio), more free water is available to participate in the hydrolysis reaction. Thus, the hydrolysis reaction can be expected to be enhanced when more free water is present. The H ratio affects the rate of hydrolysis by enhancement of the diffusion rate of the TEOS alkoxide molecules into the reverse micelles. It was found that the rate of hydrolysis of the organometallic precursors in Ag contained reverse micelles is much faster than that of CdS contained reverse micelles and result in a more uniform distribution both in the size and thickness of the shell. This suggest that the nature of the core's particle surface plays an important role in the interaction between the core materials and the hydrolyzed silanol group, and thus, influence the surface modification and layer growth. The rate of condensation through the inter-micellar interaction can be controlled by the bulk solvent. The fast condensation rate has been observed as a result of increasing the chain length of the bulk solvent due to the enhancement of the inter-micellar interaction.

A significant number of homogeneous "pure" SiO_2 particles have been found in almost all of the final products. As mentioned in chapter 4, the formation of homogeneous SiO_2 may be attributed to the distribution of the core's ionic species in the reverse micelles or associated with the dynamic process of the inter-micellar interaction. The reverse micelles may not be "fully occupied" by the metallic clusters of the core's materials in the first stage if the concentration of the reactants is relatively low and aggregation number of

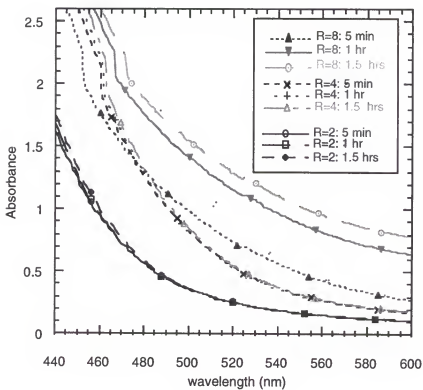


Figure 5-10. The increase of the rate of hydrolysis as a function of water content, R , can be quantitatively monitor through the changes of the slopes of absorption spectra taken from 5 min to 1.5 hrs after initiation of hydrolysis of TEOS. (at the constant of $X=1$ and $H=100$, and different R : $R=2$; $R=4$; $R=8$;))

micelles is relatively large. Thus, empty micelles will exist where the SiO_2 particles can form followed by hydrolysis and condensation of TEOS alkoxide molecules. The empty micelles may also form during the dynamic process of inter-micellar interaction as suggested by Fletcher [96]. The "empty" droplets released during the inter-micelle interaction may provide a microenvironment for TEOS precursors to nucleate and grow through hydrolysis and condensation. Thus, the formation of the pure SiO_2 particles is likely inherent with the microemulsion process to synthesize the nano-composite particles.

5.4. Conclusion

Spherical nano-composite Ag/ SiO_2 particles with uniform size distribution have been prepared using self-assembly molecules in conjunction with hydrolysis and condensation of organometallic precursors. These metallic nanometer-size composite particles have excellent stability and reproducibility based on optimizing the synthesis conditions. The average size of the metallic cluster is found to be dependent on the micellar size, the nature of the solvent, and concentration of the reagent. The UV-visible spectroscopy and TEM studies of the particle formation indicate that the reaction process in the complex matrix (reverse micelles and TEOS) is governed by the diffusion control process in terms of the dynamics behavior of the micelles (inter-molecular exchange rate). The nature of water in the reverse micelle also plays an important role on the reaction: at very low water content the nature of water bound with the hydrophilic head groups of amphiphilic molecules is drastically different from bulk water, which can explain the exceptional stability of the metallic nano-composites. With increasing water content, the nature of water becomes bulk-like (free water) and facilitates more rapid hydrolysis. By controlling the other processing parameters such as the ratio of water to TEOS, and the ratio of TEOS to catalyst, the size and the coating layer can be adjusted and different final products either nano-composites or even transparent gels can be obtained. The versatility of this method may be useful in optical electronic and other practical applications.

CHAPTER 6 OPTICAL PROPERTIES OF NANO-COMPOSITE Ag/SiO₂ PARTICLES

6.1. Introduction

The optical spectra of low-dimensional solids such as metal and semiconductor clusters can be substantially different from their bulk parents. For instance, when the size of semiconductor microcrystallites decreases, the absorption edge of the linear optical spectrum is shifted towards higher energies, resulting from changes of the electronic structure due to the confinement of charge carriers. The absorption peaks around the absorption edge are attributed to the enhanced exciton banding energy and is of fundamental interest in the study of the electronic structure and nonlinear optical properties of the semiconductor microcrystallites. Schmitt-Rink et al [130] have shown that the reduction in dimensionality of a system from 3D (bulk) to essentially 0D for semiconductors can, in certain conditions, lead to an enhanced optical nonlinearity which is determined by the electron and hole states of such 0D microcrystallites. Richard et al. [28] reported the first experimental study of nonlinear optical properties of metallic colloids (clusters). It was observed that optical phase conjugation in these media is very strongly enhanced near the surface-plasma resonance frequency of the metal clusters. Neeves et al. [30] postulated that the optical phase conjugation could be further enhanced by nanometer-size composites with a metallic core and nonlinear shell or with a nonlinear core and metallic shell. The enhanced optical nonlinear response associated with metal-insulator composites appears to be related to the quantum size effects and local field enhancement at the surface-plasmon resonance.

There already exists an extensive body of literature on the subject of optical nonlinearities, and, in particular, on the third-order nonlinearity ($\chi^{(3)}$) of semiconductor

and metal microcrystallites in conjunction with potential practical applications. It is not the intention here to deal with this topic in detail, but simply to highlight some of the ideas that have been proposed, to demonstrate a few representative experimental techniques and results, and to provide scientific background with the aim to interpret the experimental results in this section. There are number of general texts available, including those by Boyd [131], Shen [132], Gibbs [133], and Prasad and Williams (1991) [134], and there are several reviews by Williams et al. [135], Brus [103], and Wang [12], that discuss some of the basic physics and chemistry involved with nanometer-size microcrystallites.

6.2. General Treatment

When an electromagnetic wave propagates through a medium, it induces a polarization \vec{P} as a result of the relative motion of the electrons and nuclei in response to the applied fields. The induced polarization oscillates at the frequency determined by the combination of the properties of the material and frequencies obtained in the incident light waves. The optical properties of the medium and the characteristics of the radiation that is transmitted through the medium result from interactions between the fields radiated by the induced polarization and the incident fields. The propagation of an optical wave in a medium is described by the Maxwell equation:

$$\nabla^2 E(r,t) - (\epsilon, \mu_0) \frac{\partial^2 P(r,t)}{\partial t^2} = \frac{1}{c_0^2} \frac{\partial^2 E}{\partial t^2} \quad [6-1]$$

where $E(r,t)$ is the macroscopic electric field arising both from the optical wave and from the induced polarization, averaged over domains that are large compared with molecular dimensions. $P(r,t)$ is the induced polarizations describing the effects of a medium present in the propagation path. Nonlinear optics is concerned with how the electromagnetic field of a light wave interacts with the electromagnetic field of matter and other light waves. As light travels through a material, this electric field interacts with other electric fields within the material. These internal fields are a function of the time dependent electron density

distribution in the material and the electric fields of the other light waves if, for example, two or more light sources are used. In a nonlinear optical material, strong interactions can exist among the various fields. These interactions may change the frequency, phase, polarization, or path of the incident light .

The bulk polarization, \bar{P} , induced in the medium can be written as a Taylor series in the optical electric field E , assuming that the anharmonic terms are relatively small; so [134]

$$\bar{P} = \chi^{(1)}E + \chi^{(2)}E^2 + \chi^{(3)}E^3 + \dots \quad [6-2]$$

where $\chi^{(1)}$ is the first-order (linear) optical susceptibility, and $\chi^{(2)}$ and $\chi^{(3)}$ are the nonlinear second- and third-order optical susceptibilities respectively. In general,

$$\chi^{(1)} \gg \chi^{(2)} \gg \chi^{(3)}$$

and $\chi^{(2)}$ and $\chi^{(3)}$ only become important when intense light sources are used and optical electrical fields greater than 10^6 Vm^{-1} are generated. For low light levels, where E is only on the order of hundreds of volts per meter, only the $\chi^{(1)}$ term is significant.

At optical frequencies, $\chi^{(1)}$ is related to the refractive index, n , by the relation

$$n^2(\omega) = 1 + 4\pi\chi^{(1)} = \epsilon(\omega) \quad [6-3]$$

As n is complex, it contains both real and imaginary terms:

$$\tilde{n} = n + iK \quad [6-3']$$

where K is the extinction coefficient. The real parts of $\epsilon(\omega)$ and \tilde{n} are related to refraction, while the imaginary part, iK , is related to the absorption of light. In the linear case involving $\chi^{(1)}$, the normal refractive index, n , as well as K are independent of the optical electrical field strength E .

For the simple treatment, only the time-dependent terms will be considered. This is for the case of light incident normal to a slab of dielectric medium, and

$$E = E_0 \cos(\omega t) \quad [6-4]$$

For the modulation effects resulting from the effect of the optical field on both n and K , the polarization P can be represented substituting Eq.6-4 into 6-2 to give

$$\bar{P} = \chi^{(1)} E_0 \cos(\omega t) + \chi^{(2)} [E_0 \cos(\omega t)]^2 + \chi^{(3)} [E_0 \cos(\omega t)]^3 + \dots \quad [6-5]$$

Since $\cos^2(\omega t)$ equals $1/2 + 1/2 \cos(2\omega t)$, and $\cos^3(\omega t)$ equals $1/4 \cos(3\omega t) + 3/4 \cos(\omega t)$, the Eq.6-5 can be rearranged to give

$$P = \frac{1}{2} \chi^{(2)} E_0^2 + \chi^{(1)} E_0 \cos(\omega t) + \frac{3}{4} \chi^{(3)} E_0^3 \cos(\omega t) + \frac{1}{2} \chi^{(2)} E_0^2 \cos(2\omega t) + \frac{1}{4} \chi^{(3)} E_0^3 \cos(3\omega t) \quad [6-6]$$

Because the second-order nonlinear interactions involving $\chi^{(2)}$ only take place in noncentrosymmetric crystals having no inversion symmetry, we can ignore the terms in $\chi^{(2)}$, since most of the systems with which we are concerned have a centrosymmetric structure and inversion symmetry with $\chi^{(2)}=0$. Third-order interactions involving $\chi^{(3)}$ occur in all materials and this is the process of interest here.

Thus, for the terms in Eq.6-6 containing $\chi^{(3)}$, $\frac{1}{4} \chi^{(3)} E_0^3 \cos(3\omega t)$ represents the response at frequency 3ω resulting from an applied field at frequency ω , and this leads to third-harmonic generation. Three photons of frequency ω disappear, creating one photon at frequency 3ω . The other term, $\frac{3}{4} \chi^{(3)} E_0^3 \cos(\omega t)$, describes the nonlinear contribution to the polarization at the same frequency ω as the incident field, and this leads to a nonlinear contribution to the refractive index n .

The third-order nonlinear optical susceptibility, $\chi^{(3)}$, occurs independently of whether or not a material possesses inversion symmetry. Included among these effects are those especially popular for production of a phase-conjugate wave such as stimulated

Brillouin scattering, stimulated Raman scattering, and degenerate four-wave mixing in Kerr-like media. Some important effects are:

- third-harmonic generation
- nondegenerate four-wave mixing
- Raman scattering
- instantaneous ac Kerr effect
- (degenerate four-wave mixing)
- Brillouin scattering
- dc-Kerr effect
- two-photon absorption
- dc-induced harmonic generation

As an example of third-order effects, $\chi^{(3)}$ in a Kerr-like media depends linearly upon the intensity of the incident light wave. In a liquid, such an effect can arise from a forced orientation of elongated molecules along an applied electric field; if the electric field vector is not along a principal axis of the individual molecule's polarizability tensor, then the induced dipole is not parallel to the field and the torque is nonzero, forcing the partial alignment of the molecule's high polarizability axis along the direction of applied electric field. This will increase the refractive index that a linearly polarized light wave experiences and thereby decreases the speed of the light wave. Other mechanisms that can contribute to the nonlinear refractive index of a material include off-resonant excitation of narrow-band absorbers and distortion of the electronic distribution in a material. These latter two mechanisms are closely related.

A Kerr-like effect is characterized by an intensity-dependent refractive index of the form

$$n = n_0 + n_2 \langle E^2 \rangle \quad [6-7]$$

This intensity-dependent index is responsible for self-focusing, in which a transverse (x, y) intensity variation in a beam propagating in the z direction causes a corresponding transverse variation in refractive index, which can be thought of as a lens formed in the material. For a spatially smooth beam whose intensity peaks on axis, a positive value for n_2 induces a positive lens, which further concentrates the light, causing the formation of a stronger lens, etc. For a material with a negative n_2 , self-defocusing occurs [134].

In addition to spatial effects, the intensity-dependent index will vary in time if the optical field envelope does. Thus a pulse of light will experience a time-varying refractive index, and this pulse will acquire a form of frequency modulation known as self-phase modulation. When multiple beams pass through such a material, interference sets up through a phase grating that can scatter beams into new directions or into each other. This nonlinearity provides the basis for degenerate four-wave mixing.

6.3. Linear and Nonlinear Optical Effects in Metal Clusters

6.3.1. Surface Plasmon Mode and Linear Optical Properties

The linear optical properties of small metallic particles are of considerable interest and have been accorded attention by a large number of physicists. Colloidal dispersions of metals exhibit absorption bands or broad regions of absorption from the ultraviolet to visible range due to the excitation of plasma resonance or interband transition, and such absorption are thus a very characteristic property of the metallic nature of the particles. Some colloidal metals have distinct absorption bands in the visible region, and as a consequence they have attractive colors for cosmetic applications. The most notable of these are dispersions of silver, copper, or gold, which have applications as the yellow or red coloring agents in some colored glasses and in decorative glazes for porcelain. On the other hand, several other colloidal metals, for example rhodium or platinum, exhibit only rather broad absorption continua which extend throughout the visible-near ultraviolet range, and these colloids are brown or grey.

According to the Drude theory, the plasma resonance of bulk metals corresponds to the point where the free electrons can no longer shield the interior of the metal from the incident radiation.

$$\varepsilon = 1 - \frac{\omega_p^2}{\omega(\omega + i/\tau)} = \varepsilon_1 + i\varepsilon_2 \quad [6-8]$$

$$\varepsilon_1 = 1 - \frac{\omega_p^2 \tau^2}{(1 + \omega^2 \tau^2)} \quad [6-9]$$

$$\varepsilon_2 = \frac{\omega_p^2 \tau}{\omega(1 + \omega^2 \tau^2)} \quad [6-10]$$

when $\omega^2 \tau^2 \gg 1$

$$\varepsilon_1 = 1 - \left(\frac{\omega_p^2}{\omega^2} \right) \quad [6-11]$$

where $\omega_p^2 = \frac{4\pi N e^2}{m}$ is the plasma resonant frequency and N is the number of free electrons in the metallic cluster. Above the plasma resonance frequency, the reflectivity drops and dielectric constant becomes positive.

The bulk plasma resonance frequency of alkali metals is proportional to the number of free electrons per unit volume. In transition metals, the contribution of the bound electrons from the d-band can greatly decrease the plasma resonance frequency. A comparison between copper and silver demonstrates this effect. The band structure of both metals are similar, and the contribution to the dielectric constant from the free electrons crosses zero of dielectric function above 8 eV (Ag=9.2 eV, Cu=8.7 eV). The d-s interband transition is 4.0 eV for silver, and 2.0 eV for copper. In the copper, the positive maximum in the real part of dielectric constant contributed from the bound d-band electron occurs when the free electron contribution is still strongly negative. As a result, the plasma resonant frequency will not be changed by the interband transition, and the dielectric

function crosses zero well above 6 eV. In the case of silver, the positive maximum occurring at 4.0 eV is sufficient to compensate the negative part of dielectric constant from free electrons and bring the total real part of the dielectric constant across to zero. Then silver has a pronounced plasma resonance at 3.9 eV which consists of a collective oscillation or hybrid resonance including both the free (s) and bound (d) electrons. On the other hand, in copper, because the contribution from bound electrons is not enough to balance that from free electrons, the total dielectric constant remains near zero without crossing it for a broad range of energies. As a consequence, the characteristic drop in reflectivity begins at 2 eV attributed from the d-s interband transition, but the decrease is small and the plasma frequency of copper occurs above 10 eV.

However, the optical absorption spectra is quite different for the bulk versus small metallic particles. The characteristics of the optical spectra of small metallic particles and the differences with bulk metal are attributed to the so-called surface-plasma resonance and the limited mean free path of the small particles (in particular, when the size of the metallic particle is smaller than the wavelength of light), which can be adequately explained with the classical Mie theory [136].

Consider a single representative spherical particle of diameter d with complex dielectric constant [136], embedded in a dielectric medium of dielectric constant ϵ_m . In the presence of an oscillating electric field, the build-up of surface charge provides a restoring force that leads to resonant density oscillations of the conduction electrons at a suitable frequency. This is the surface plasma mode. Using Mie's formalism, the absorption coefficient, K , of the small metallic particles dispersed homogeneously in a dielectric medium with the dielectric constant ϵ_m is given by

$$K = \frac{18\pi f \epsilon_m^{3/2}}{\lambda} \frac{\epsilon_2}{(2\epsilon_m + \epsilon_1)^2 + \epsilon_2^2} \quad [6-12]$$

where the f is the volume-filling fraction of metal and λ is the photon wavelength. The absorption coefficient has a maximum value when the real part of denominator goes to zero, which can occur at the surface-plasmon resonance frequency

$$\varepsilon_1(\omega_{sp}) = 2\varepsilon_m \quad \text{or} \quad \text{Re}\{\varepsilon_1(\omega_{sp}) + 2\varepsilon_m\} = 0 \quad [6-13]$$

where ω_{sp} is the surface-plasma resonance frequency.

It is generally accepted that a good approximation to the dielectric constant in small particles is easily obtained from the bulk optical constant. The contribution due to interband transitions $\varepsilon_b(\omega)$ is mostly believed to remain unchanged, but the Drude-like free electron part should be modified because of the change of the limited mean free path of the electrons as particle size decreases. By taking into account the contribution of surface scattering as particle size decreases, the resulting dielectric constant can then be written as :

$$\varepsilon(\omega) = \varepsilon_b(\omega) - \frac{\omega_p^2}{\omega(\omega + i/\tau)} = \varepsilon_b(\omega) - \frac{\omega_p^2/\omega^2}{1 + 1/\omega^2\tau^2} + i \frac{\omega_p^2/\omega^2}{\omega\tau(1 + 1/\omega^2\tau^2)} \quad [6-14]$$

where τ is the size limited scattering time,

$$\frac{1}{\tau} = \frac{1}{\tau_0} + \frac{2v_F}{d} \quad [6-14']$$

where the term τ_0 is the scattering time in the bulk material, v_F denotes the Fermi velocity, and d is the diameter of the particle. In combination with the condition of surface-plasmon resonance (Eq.6-13), we obtain:

$$\frac{\omega_p^2/\omega_{sp}^2}{1 + (1/\omega_{sp}\tau_0 + 2v_F/\omega_{sp}d)^2} = \varepsilon_b(\omega_{sp}) + 2\varepsilon_m \quad [6-15]$$

In the interpretation of the optical properties of small particles, it was soon realized that the limited mean free path of the electrons is the most important factor leading to modifications of the optical constant of finely dispersed metals.

Classically, one assumes that for sufficiently small particles the electron mean free path is entirely limited by boundary scattering, and will be smaller than the bulk mean free path. As a consequence, for the small particles the linewidth, Γ , at the half-maximum of the surface plasmon peak, which is given by [137],

$$\Gamma = \tau^{-1} = \frac{2v_F}{d} \quad [6-16]$$

will become broader as the size of the particles decrease. Taking the Fermi velocity for silver to be $v_F = 1.4 \times 10^8 \text{ cm sec}^{-1}$ one can easily calculate the classical theory of the linewidth from Eq. 6-16. The results from the classical theory are found to fall closely through the experimental data [137].

For a very small particle a new effect may come into play: Due to size quantization, the conduction band will break up into discrete levels with an average separation that is large compared to the thermal energies. This is the so-called quantum size effect. The Drude expression of Eq. 6-14 will then no longer be valid. Several attempts have been made to derive a dielectric function relevant for this situation quantum mechanically. Kawabata and Kubo [138] have argued that the classical interpretation of mean free path limitation by scattering at the surface of the small particles is incorrect. The surface of the particles in this size range (less than 100 nm) does not really scatter the electrons. It rather manifests itself as a boundary condition for electron states bound to a finite volume of the particle. The dissipative part ϵ_2 of the dielectric constant represents dipole transitions between these eigenstates, and has been calculated based on quantum theory. The general expressions found for ϵ_2 by different authors agree with the result originally obtained by Kawabata and Kubo with:

$$\epsilon_2^{QM}(\omega) = \frac{12\omega_p^2 v_F}{\pi^2 \omega^3 d} g_s \left(\frac{\hbar \omega}{\epsilon_F} \right) \quad [6-17]$$

where Comparing this solution with the classical result as given in Eq.6-14 in the limit for small particles, when $1/\tau \approx 2\nu_F/d$:

$$\epsilon_2^{Drude}(\omega) \approx \frac{2\omega_p^2\nu_F}{\omega^3d} \quad [6-18]$$

The general tendency of the observed linewidth of the surface plasmon resonance of small silver particles is consistent with this d^{-1} dependence, as predicted in both quantum mechanical results and the classical Drude-like model. However, the effective mean free path from quantum mechanical theory is approximately twice the value of the classical estimation leading to a linewidth of surface plasmon resonance that is considerably smaller than the one observed. For example, using the quantum mechanical formalism for silver particles as given by Kawabata and Kubo:

$$\Delta\lambda = 0.0063 + 0.58/d + 4.32 \times 10^{-9}/d \quad [6-19]$$

where $\Delta\lambda$ is in micrometers and d is in Ångstrom units. The experimental results from the silver-glass samples are in good agreement with the classical theory. On the other hand, very recent work (Charle, Frank, and Schulze, Ref.139) on rare-gas isolated silver particles gives evidence for much narrower surface plasmon resonance and appears to be more consistent with the quantum mechanical theory. Thus far, the different results between the classical theory and quantum mechanical theory have not been reconciled. It should be noted that a fairly large size distribution often exists in the most samples. In addition, a further complication arises when one considers the deviations from spherical particle shape. For either a distribution of size or orientations of shape existing in samples the combined surface plasmon absorption will tend to be broadened.

The situation is even more controversial when considering the position of the peak of the surface plasmon resonance. The classical Mie theory only takes into account Maxwell's equation, and therefore the resulting resonances are purely geometrical in origin. For small particles, higher order terms of Mie theory can be neglected and the position of

the resonance peak will be fixed, unless some size dependence of dielectric constant comes into play [140]. This is illustrated by model calculation for small sodium particles of Smithard and Tran [141]. It was found that the peak of the resonance has insignificantly shifts for particles with diameters below approximately 10 nm. For even smaller particles the classical concept of the limitation of the mean free path will lead to a shift of the peak position towards longer wavelength.

In contrast, the model calculation based on the quantum size effect for small particles gives a different result than the classical one, and the peak of the resonance shifts towards higher frequencies as the size of the particle decrease. This shift to higher frequencies of the position of the surface plasmon resonance with decreasing particle size was found to be the general solution of quantum mechanical calculation.

Among the numerous experiments attempted to verify the theoretical results, silver is the most suitable metal, since it is relatively easy to handle and the surface plasmon resonance is very prominent and narrow. Even more important, the size distribution of Ag colloids can easily be measured directly by electron microscopy. Accordingly, one could expect having reliable results from Ag colloids. Unfortunately, the experimental results are very divergent, and very sensitive to the matrix in which Ag colloids are embedded as well as the preparation procedures: Ganiere et al. [142] (aggregation in a glass matrix) reported a red shift and strong broadening of the surface plasmon with decreasing particle mean diameter. Genzel et al. [143] (aggregation in a glass matrix) obtained a strong broadening and if at all, a very weak blue shift. Schulze et al. [139] (gas aggregation and subsequent embedding in solid Ar) measured a definite blue shift but a comparatively weaker broadening with decreasing size. The linewidth of the absorption band increases in all cases linearly with the reciprocal mean diameter $1/d$. Obviously, it is hard to draw any definite conclusions from these experiments, except that something certainly happens. Resorting to theory for a decision does not help either. A thorough examination of the literature reveals that the different theoretical approaches (classical, semi-classical, and

quantum mechanical) give different results, and depend sensitively on the approximation and especially on the models (e.g. infinite barrier models) chosen to make the calculations. Therefore, it is generally accepted that a quantitative straight forward comparison between experiment and theory appears to be inconclusive and remain uncertain at the present time.

The experimental results suggest that the Mie theory likely holds true for larger particles ($d > 10$ nm) whereas changes with decreasing size in the peak position and linewidth of the surface plasmon absorption band depend sensitively on the surface properties of the metallic cluster. The existence of electric-double layers in polar solvent and chemical- and physical-absorption onto the surface of metallic particles indeed modifies the electronic density profile in the surface layer of the metal particles, and thus changes the effective electronic potential. As a consequence, the surface plasmon resonance and linewidth of the plasmon absorption peak, the characteristics of the electronic structure, will be changed. Embedding the Ag clusters grown in the gas phase in different matrices within the same experimental run, Charle et al. studied the matrix effects on the shift of the surface plasmon peak due to different surface modifications. The results obtained support the simple classical picture: the plasmon peak shift sensitively depends on the interaction of the clusters with surrounding atoms or molecules. The more electrons that are spilled out of the geometrical surface of the metal clusters (demetalization), the more a red shift is favored. On the other hand, the more electrons that are injected into the metal clusters through the surface, the more a blue shift is observed.

6.3.2. Linear Absorption Optical Spectra of Ag and Ag/SiO₂ Clusters

Figure 6-1a shows the linear absorbance of the Ag and Ag/SiO₂ clusters prepared through the microemulsion method developed in the course of the present work. The resonance features are due to surface-plasmon excitation. The resonance frequency of the Ag clusters capped with surfactant was around 405 nm with a slight red shift as the size of the clusters increased. To measure the full width at half maximum (FWHM) of each

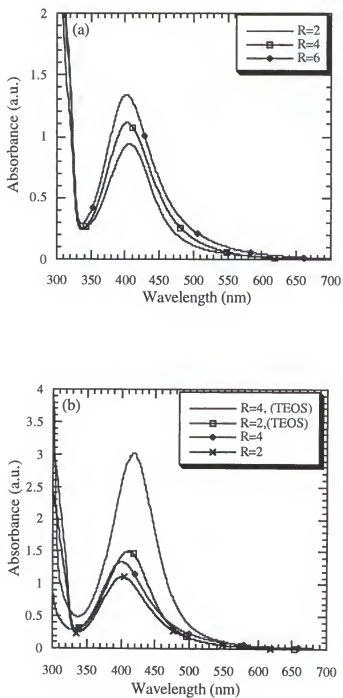


Figure 6-1. Linear absorption spectra of Ag clusters and their nano-composites: (a) Linear absorption spectra of Ag colloids, and (b) comparison of the Ag clusters with Ag/ SiO₂ nano-composites.

absorption spectrum, $\lambda \approx 300$ nm have been used as a baseline to obtain FWHM of ~ 58 nm for four samples. If Ag particles are modeled as spheres, then ϵ_2 is size independent according to the experimental results. The results suggest that for particles with dimensions less than 15 nm the quasi-static approximation in Eq.6-16 is reasonable [144]. Within the quasi-static approximation, features of the absorbance spectrum such as the width and the peak position of the surface-plasmon resonance are size independent. Thus, the free path effect resulting in the plasmon broadens and the peak shifts as a function of the size can not be observed in this size range.

However, the absorption spectrum of the nano-composites in Figure 6-1b shows that relative intensity as well as the surface-plasmon resonance peak change in comparison with the pure Ag colloids while the size of the Ag cluster remained the same. The plasmon resonance peak shift towards the higher energy region with increasing intensity of the absorbance. The plasmon resonance according to both classical and quantum mechanical theory are very sensitive to the electronic density profile [145]. The more electrons that are spilled out of the surface of the metal cluster (demetallization), the more a red shift is favored. In contrast, the more electrons that are injected into the cluster surface, the more a blue shift is favored. A number of authors have, in the past, invoked demetallization to explain phenomena associated with the surface of metals [146]. The red shift or blue shift of the surface-plasmon resonance have been observed by injecting excess charges (electrons or holes) [147]. These effects are attributed to the influence exerted by the changing electron density on the discrete interband transitions. The filling of the conduction band states at the Fermi level by injecting electrons shift the transition to higher photon energies. Conversely, hole injection causes the onset of interband transitions to shift to lower energies. Thus, the red shift of the surface-plasmon resonance observed in our experiment could be attributed to the chemisorption of the hydrolyzed silanol group onto the surface of Ag clusters.

6.3.3. Nonlinear Optical Properties of Ag/SiO₂ Nano-Composites

Relative to linear optical properties, nonlinear optical properties of small metallic clusters have only attracted intensive study in the past few years. The interest arises from both fundamental science and potential applications. The conjugate reflectivity of small gold particles was first reported by Ricard et al. [28] at $\lambda=530$ nm, they measured a value of $\chi^3 = 10^{-8}$ esu and a response time of <50 psec. A later paper, by Hache et al. [148] reported the development of a model for third-order nonlinearities of metallic clusters, in which two essential elements were used to account for the possible enhancement of the conjugate signal in the metallic clusters: surface-plasmon excitation and a $\chi^{(3)}$ that is due to quantum size effects.

At the surface-plasmon resonance large enhancements of local field inside the particle can be realized according to the well known "effective medium theory" [149]. In this quasi-static limit the local field of a spherical particle, E_l , is related to the applied field, E_0 , by

$$E_l = \frac{3\varepsilon_d(\omega)}{\varepsilon_m(\omega) + 2\varepsilon_d(\omega)} E_0 = f(\omega)E_0 \quad [6-20]$$

where $\varepsilon_m = \varepsilon'_m + i\varepsilon''_m$ is the complex dielectric response of metal, ε_d is the dielectric function of the host material, and $f(\omega)$ is defined as the local-field factor. The nonlinear source polarization can be written as [146]

$$\vec{P}^{(3)} = 3 \left[\rho f(\omega)^2 |f(\omega)|^2 \chi_m^{(3)} \right] E_f E_b E_p^* \quad [6-21]$$

where E_f , E_p and E_b are the electric field of the three incident beams in the degenerate four-wave mixing (DFWM) experiment, ρ is the volume fraction of the particles in the composite material, and $\chi_m^{(3)}$ is the third-order nonlinear susceptibility of the metallic cluster. A significant feature of the model is the strong size dependence of $\chi_m^{(3)}$, which is proportional to $1/r^3$, where r is the radius of the metal particle.

Another possible mechanism attributed to the nonlinear response of metal particles is based on Fermi smearing or nonequilibrium electron heating. Schoenlein et al. [150] measured change in the reflectivity of a thin gold film, using a pump-probe technique with a 65-fsec pulse. The pump pulse energizes the conduction electrons, resulting in a high electron temperature while the lattice remains cool. The heating leads to the Fermi smearing, which rearranges the occupancy distribution of conduction electrons near the Fermi surface, increasing the occupancy above the Fermi energy and decreasing the occupancy below the Fermi energy. The Fermi smearing affects the transition probability of the d -band electrons to the conduction-band energies near the Fermi level, leading to changes in the reflectivity at the surface of the gold film. The Fermi smearing contribution has been incorporated by Hache et al. [144] into a model for the nonlinear response of metal-particle composites. The results predict that the value of $\chi_m^{(3)}$ due to Fermi smearing is independent of particle size and will dominate a quantum size contribution by 2 orders of magnitude in 5 nm diameter gold particles while the surface-plasmon resonance remains an important feature of the observed $\chi_m^{(3)}$, owing to the enhanced local field.

Furthermore, Neeves et al. [30] postulate that the nonlinearities of the metallic clusters could be further increased if the composites consist of core-shell structure such as a metallic core and nonlinear shell or versa vice. Optical phase conjugation will be enhanced from each nonlinear region because the optical field can be concentrated in both the interior and the exterior neighborhoods of the particle and magnified at the surface-plasmon resonance. Enhancement of the phase conjugate signal is calculated based on the electrostrictive mechanism dominant in the microsecond time scale and the electronic mechanism dominant in the picosecond time scale. Moreover, the model predicts that a limited range of resonance tunability can be achieved by adjustment of shell thickness.

6.3.3.1. Local field enhancement and effective dielectric constant

The electric field in heterogeneous composites containing small and dilute particles can be calculated using classical electrodynamics theory. Consider a layer of nonabsorbing

material with dielectric constant ϵ_m which contains a volume fraction f of small absorbing metal particles with dielectric function ϵ_i , (Figure 6-2). This composite medium is polarized by an external field E_0 . The degree of the polarization is determined by the shape and dielectric function of the particles, by the dielectric constant of the surrounding medium, and by the extent to which particles interact by means of their dipolar moments

The polarization of the composite medium can be described quantitatively by defining an average dielectric function ϵ^{av} . This is easily done only if the field inside the sphere, E_i and the field outside the sphere, E_m , are nearly homogeneous. The field E_m

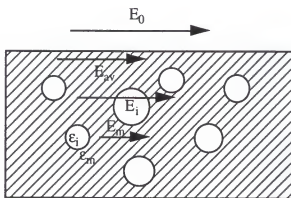


Figure 6-2. Ionic spheres with dielectric function ϵ_i embedded in a nonabsorbing medium with dielectric constant ϵ_m . The electric fields inside the spheres and in the nonabsorbing medium are denoted by E_i and E_m respectively.

outside a particle is a superposition of the external field E_0 and the dipolar fields of the other particles. The inner field of a particle E_i is a superposition of E_m and a depolarizing field due to the induced surface charges on the particle. The field of E_m will fluctuate through the composite. This inhomogeneity of E_m is partly due to the discreteness of the particles and partly due to nonuniformity in the particle size and shape distributions. The field E_i may also be inhomogeneous for several reasons. However, if the particles are assumed to be small compared to the wavelength of the field, the depolarizing field is

homogeneous over the volume of the particle and the field inside the particle is proportional to the applied field.

Assuming that the average field inside the composite medium can be written as:

$$E_{av} = fE_i + (1-f)E_m \quad [6-22]$$

with E_i and E_m not independent of one another, then as a particle with ellipsoidal shape, the field along one of the principal axes can be written [149],

$$E_i = \frac{\epsilon_m}{g\epsilon + (1-g)\epsilon_m} E_m \quad [6-23]$$

The depolarizing factor g can have values between zero (acicular shape) and one (platelet shape). For a sphere with $g = 1/3$ the field inside the particle is

$$E_i = \frac{3\epsilon_m}{\epsilon + 2\epsilon_m} E_m \quad [6-23']$$

Using the continuous condition of the tangential component of the field, $E_{av} = E_0$, E_m can be expressed in terms of E_0 with,

$$E_m = \frac{\epsilon + 2\epsilon_m}{(\epsilon + 2\epsilon_m) - f(\epsilon - \epsilon_m)} E_0 \quad [6-24]$$

and the induced electric dipole moment can be written as

$$P = \frac{\pi}{6} d^3 \frac{\epsilon - \epsilon_m}{\epsilon + 2\epsilon_m} 3\epsilon_0 E_0 \quad [6-25]$$

It is clear from Eqs. [6-22]-[6-25] that the magnitude of the electric field in the interior and vicinity of the particle as well as the induced dipole moment can be substantially enhanced compared with the field far from the particle by choosing material parameters that satisfy the condition of the surface plasmon resonance: $\text{Re}(\epsilon + 2\epsilon_m) = 0$.

The most important results from the above derivations is that the effective dielectric function of the medium together with the particles can be expressed as

$$\tilde{\epsilon} = \epsilon_m + 3f\epsilon_m \frac{\epsilon - \epsilon_m}{\epsilon + 2\epsilon_m} \quad [6-26]$$

where $\epsilon = \epsilon' + i\epsilon''$ (complex and frequency dependent) is the dielectric constant of the metallic particle and ϵ_m (real) is that of the matrix dielectric.

6.3.3.2. Degenerate four-wave mixing (DFWM)

Four-wave interactions have become one of the most thoroughly investigated nonlinear optical effects. These processes are symmetry-allowed in all media and have found numerous applications in spectroscopic investigations with short pulses. For a physical understanding of the various phenomena, the frequency dependence of the third order susceptibility, χ^3 , is often used for the theoretical description. For spectroscopic purposes (e.g., pump-probe experiments to study the nonlinear responses) the frequency resonance of χ^3 and off-resonance situations are very important in investigations of the various material excitations and in the applications involving the generation of pulses at new frequencies.

When three laser beams at different frequencies ω_1 , ω_2 , and ω_3 are mixed in the sample by the third-order nonlinear susceptibility, the coherently generated nonlinear signals can have the frequency $\omega_4 = |\omega_1 + \omega_2 - \omega_3|$. The inherent four-photon interaction involves the annihilation of the two quanta (ω_1, ω_2) and the creation of the two new photons (ω_3, ω_4) : $\omega_1 + \omega_2 = \omega_3 + \omega_4$. The intensity of the new component I_4 is determined by the incident intensities (I_1, I_2, I_3) according to [151]

$$I_4 = \text{const} |\chi^3| I_1 I_2 I_3 l^2 \left(\frac{\sin \Delta k l / 2}{\Delta k / 2} \right)^2 \quad [6-27]$$

where $\Delta k = |k_1 + k_2 - k_3 - k_4|$ is the phase mismatch, and l denotes the interaction length.

The equation refers to low intensity situations which neglect both depletion of the incident

radiation and stimulated amplification. Usually two instead of three incident fields are coupled by the four-photon interaction (i.e. photons of one field act twice, $\omega_1 = \omega_2$ or $\omega_3 = \omega_4$ corresponding to $I_1 = I_2$ or $I_3 = I_4$). The specific role that a frequency component plays in the interaction is determined by the mismatch Δk .

The general case involving three (or four) different frequency components ($\omega_1, \omega_2, \omega_3, \omega_4$) is called non-degenerate frequency mixing. In the fully degenerate case, all four frequency components are equal. However, the fields may still be distinguishable by their polarizations and/or beam directions. There also exists a third possibility involving two different frequencies: $\omega_1 = \omega_3$, $\omega_2 = \omega_4$. This situation, also called scattering from light-induced (or phase) grating, is referred as partially degenerate four wave mixing. The wave vector diagrams for the three situations are shown in Figure 6-3 [152]. For partial or fully four degenerate four wave mixing, the phase matching condition $\Delta k = 0$ is satisfied automatically due to the frequency degeneracy. The broken arrows in the figure represent the k vectors of the induced grating which are often helpful in visualizing the nonlinear process. For a detailed theoretical treatment of the four-wave mixing process, see Oudar and Shen [153] and Ye and Shen [154].

Degenerate four-wave mixing (DFWM) is a third-order process involving the nonlinear susceptibility $\chi^{(3)}(-\omega; \omega, -\omega, \omega)$ and is the most commonly used technique in the study of the various nonlinear optical processes due to its experimental simplicity and automatic phase matching. In the DFWM measurement, three beams at frequency ω intersect in the material. The nonlinear interaction produces a fourth beam at the same frequency and its intensity is proportional to the product of the input intensities and absolute square of $\chi^{(3)}$. In the case far from single or different-frequency resonance of $\chi^{(3)}$, in a Kerr-like medium, four-wave mixing is readily visualized in terms of the nonlinear change of refractive index connected with the real part of the third order nonlinear susceptibility. Electronic transitions in terms of the so-called electronic hyperpolarizability contribute significantly to the nonlinear susceptibility so that four-wave mixing at electronic

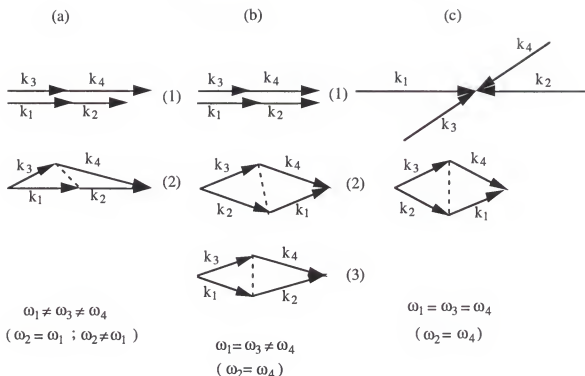


Figure 6-3. Wavevector diagrams of the mixing process $\omega_1 + \omega_2 \rightarrow \omega_3 + \omega_4$; (a) nondegenerate case with phase-matching $\Delta k = 0$ adjustable in the off-axis geometry (2); (b) partially degenerate four-wave mixing with automatic phase-matching in the one-beam (1) and two-beam (2) experiments, whereas in the four-beam geometry, $\Delta k = 0$ has to be adjusted; (c) fully degenerate case, DFWM, with automatic phase-matching with pairwise counterpropagating (1) or co-propagating beams (2) for arbitrary beam intersection angle. Broken lines indicate the k -vectors of several induced (non-propagating) phase and/or amplitude gratings (from ref 152).

transition resonance can be visualized as polarizability changes associated with the nonlinear susceptibility (both in the real and imaginary part) and yield information on the dephasing time of the transition. DFWM can be carried out in different geometries: off-axis or collinear. The case of pairwise counter-propagating beams displays interesting properties with optical phase conjugation which can be used for real-time processing of optical fields based on time reversal of the incoming wave. The usual experimental configuration of the laser beams in DFWM measurements is the phase conjugation geometry. In phase conjugate-geometry two pump beams (E_1 , E_2) arranged to be counterpropagating and the third probe beam intersects the other two at some angle in the sample. The generated wave travels directly along the angled probe beam but in the opposite direction as if the probe beam were "reversed" in time. This apparent reversal also holds for the spatial shape of the probe beam which exactly retraces itself. One way to visualize four wave mixing is to realize that the input beams modify the refractive index of the material in proportion to the intensity. Two beams intersecting at an angle in the medium interfere and form an intensity grating, and therefore a grating of index modulation. This index modulation grating then diffracts the other beams in a direction that satisfies the Bragg condition for diffraction. Generally, in the phase conjugate geometry, two different gratings are formed that lead to diffraction in the direction opposite to the probe beam. The $\chi^{(3)}$ of the material can be determined from relative measurements of the intensity of the phase conjugate beam generated in a material compared to that generated in a material with known $\chi^{(3)}$.

6.3.3.3. Degenerate-four-wave mixing experiment

Three samples of Ag/SiO₂ nano-composites having the same Ag core radius and different SiO₂ coating layer thickness have been used in the experiments. The sample preparation and characterization were discussed in Chapter 5. Linear optical absorption measurement was first conducted. It was found that the surface-plasmon resonance frequency for each sample is varied as a function of the ratio of the radius of core particle

, r_1 , to that of the composite particles, r_2 [Figure 6-4]. Thus, the frequency of the laser beam was tuned according to the surface-plasmon resonance frequency of each sample.

A standard DFWM arrangement was used to measure the nonlinear optical properties of the nano-composite particles (Figure 6-5). The experiments were conducted using a Ti sapphire solid state laser ($\lambda=403$ nm) providing 200 fs pulses at a repetition rate of 250 kHz with a beam diameter of 1mm. The sample cell is constructed from two windows with a 0.5 cm spacer to minimize conversion that could destroy the grating.

The beam geometry of the DFWM experiment is shown in Figure 6-6. Two counterpropagating pump beams (E_1 , E_2) and a probe beam (E_p) are mixed in the sample cell to form two orthogonal spatial gratings of different periods. The pump beams scattered by the gratings give rise to the conjugate beam E_c and amplify the probe beam. The orthogonal spatial gratings is referred to as the coarse grating for the large-period grating and as the fine grating for smaller-period grating. The grating period is given by

$$\Lambda = \frac{\lambda}{2 \sin(\theta/2)} \quad [6-28]$$

where θ is the angle between E_1 and E_p for the coarse grating and between E_2 and E_p for the fine grating and λ is the wavelength of the light in the medium. Polarization selection is achieved with a half-wave plate. For the coarse grating, E_1 and E_p are polarized vertically and E_2 is polarized horizontally by rotation with the half-wave plate. A similar approach was used by Jain and Lind [155] for characterization of semiconductor-doped glasses, and by Neeves [30] for the polystyrene suspensions.

The computer data acquisition and signal processing system with the chopped beam, condition is used to separate the phase conjugate signal from scattered light resulting from random concentration fluctuations. The total intensity I_T received at the photomultiplier is given by

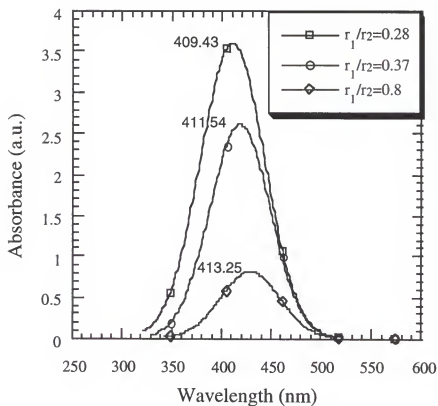


Figure 6-4. Changes of surface-plasmon resonance as a function of the ratio of r_1/r_2 .

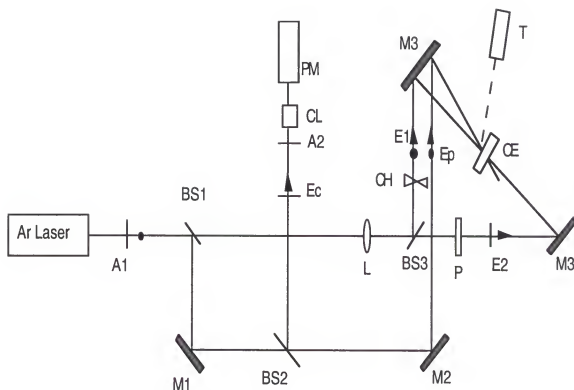


Figure 6-5. DFWM in the coarse-grating configuration. The symbols \bullet and $-$ indicate vertical and horizontal polarization, respectively. A: analyzers; M: mirrors; BS: beam splitters; P: polarizer; CL: collimator; L: lens; CH: chopper; T: telescope; CE: sample cell; E_1 and E_2 : counterpropagating pump beams; E_p : probe beam; E_c : conjugate beam.

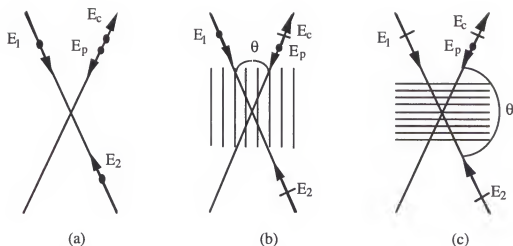


Figure 6-6. Schematic diagram for DFWM geometries: (a), coarse and fine orthogonal spatial grating configuration; (b), coarse-grating configuration; (c), fine-grating configuration. The symbols • and - indicate vertical and horizontal polarization, respectively.

$$I_T = I_s + I_c \quad [6-29]$$

where I_s is the total scattering contribution,

$$I_s = I_{1s} + I_{2s} + I_{ps} \quad [6-30]$$

and I_c is the conjugate-beam contribution. Furthermore, the two components of I_T can be separated since I_s is linear with laser power P and I_c is cubic with the laser power,

$$I_T = aP + bP^3 \quad [6-31]$$

The experimental $\chi^{(3)}$ can be obtained by curve fitting Eq.6-31 and comparing the value with the theoretically predicted $\chi^{(3)}$ which will be discussed in the next section.

6.4. Results and Discussions

Measurements of I_c versus pump intensity are shown in Figure 6-6 for the coarse-configurations with the probe-to-pump ratio ($I_{\text{pump}}:I_{\text{probe}}$) of 1:150. Measurements of I_c versus pump intensity for the coarse-grating configuration are shown in Figure 6-7 with the same intensity ratio of probe-to-pump as that of the fine-grating (Figure 6-8). In each case,

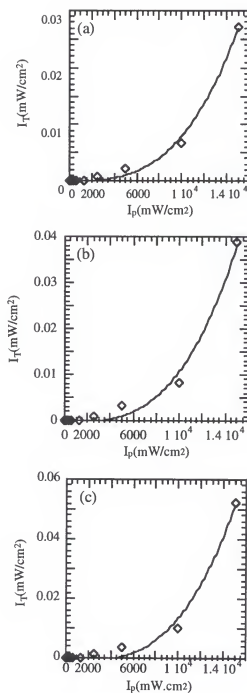


Figure 6-7. Intensity I_T versus pump intensity for the coarse-grating configuration. Sample (a): $y = 4.0696 \times 10^{-7} x^3$; (b): $y = 4.4803 \times 10^{-7} x^3$; (c): $y = 4.4367 \times 10^{-7} x^3$. Solid lines represent the best fit to Eq.6-31.

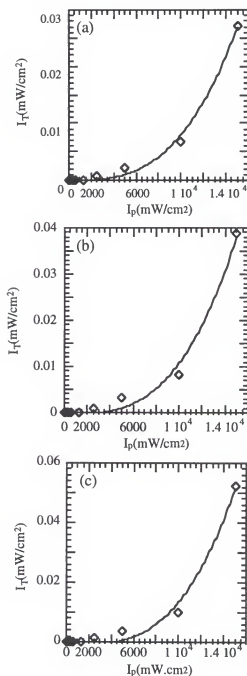


Figure 6-8. Intensity I_c versus pump intensity for the fine-grating configuration. Sample (a): $y=7.9238 \times 10^{-7}x^3$; (b): $y=1.1726 \times 10^{-6}x^3$; (c): $y=1.6544 \times 10^{-6}x^3$. Solid lines represent the best fit to Eq.6-31.

the two pump beams (E_1 and E_2) have equal intensities. Each set of data points could be fitted (solid line) by using equation [6-31], verifying the theoretically predicted, cubic dependence on the intensity indicative of the conjugate signal.

The theoretical calculations of the third-order nonlinear optical susceptibility of the nano-composites are carried out in terms of both the electrostrictive mechanism and electron mechanism [30]. Furthermore, the third-order nonlinear optical susceptibility of the metallic cluster is calculated by taking into account the quantum size effects.

Electromagnetic theory described in this chapter was used to calculate the electric-fields of the nano-composite particles as well as the enhancement factor f . The composite model was constructed with a spherical metallic core of radius r_1 and a spherical shell of radius r_2 in a suspending medium. The dielectric permittivities of the inner sphere, the shell, and the outer medium, are ϵ_1 , ϵ_2 , and ϵ_3 , respectively [Figure 6-9].

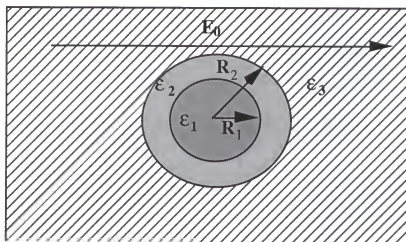


Figure 6-9. The simplified diagram of nano-composite particle embedded in a homogeneous medium is subjected to an electromagnetic field.

The electric-field distribution in each of three regions is obtained to within the electrostatic approximation by solution of the Laplace's equation with the boundary conditions appropriate to the model [30]:

$$\Delta\varphi = 0 \quad [6-33]$$

$$\varphi = \sum \left(a_n r^n + \frac{b_n}{r^{n+1}} \right) P_n(\cos\theta) \quad [6-34]$$

where φ is the electric potential. The electric field in the core region is given by

$$E_1 = \frac{9\varepsilon_2\varepsilon_3}{\varepsilon_2\varepsilon_a + 2\varepsilon_3\varepsilon_b} E_0 \left[\cos(\theta) \hat{e}_\theta - \sin(\theta) \hat{e}_r \right] \quad [6-35]$$

The electric fields in the shell region, E_2 , and outside the composite particle are given by

$$E_2 = \frac{3\varepsilon_3}{\varepsilon_2\varepsilon_a + 2\varepsilon_3\varepsilon_b} \left[(\varepsilon_1 + 2\varepsilon_2) + 2(\varepsilon_1 - \varepsilon_2)(r_1/r)^3 \right] E_0 \cos(\theta) \hat{e}_\theta \\ - \frac{3\varepsilon_3}{\varepsilon_2\varepsilon_a + 2\varepsilon_3\varepsilon_b} \left[(\varepsilon_1 + 2\varepsilon_2) - 2(\varepsilon_1 - \varepsilon_2)(r_1/r)^3 \right] E_0 \sin(\theta) \hat{e}_r \quad [6-36]$$

$$\text{and } E_3 = \left(2 \frac{\varepsilon_2\varepsilon_a - \varepsilon_3\varepsilon_b}{\varepsilon_2\varepsilon_a + 2\varepsilon_3\varepsilon_b} \frac{r_2^3}{r^3} + 1 \right) E_0 \cos(\theta) \hat{e}_\theta \\ + \left(\frac{\varepsilon_2\varepsilon_a - \varepsilon_3\varepsilon_b}{\varepsilon_2\varepsilon_a + 2\varepsilon_3\varepsilon_b} \frac{r_2^3}{r^3} - 1 \right) E_0 \sin(\theta) \hat{e}_r \quad [6-37]$$

where

$$\varepsilon_a \equiv \varepsilon_1(3 - 2P) + 2\varepsilon_2P \quad [6-38]$$

$$\varepsilon_b \equiv \varepsilon_1P + \varepsilon_2(3 - P) \quad [6-39]$$

$$P \equiv 1 - \left(\frac{r_1}{r_2} \right)^3 \quad [6-40]$$

The factor P is the ratio of shell volume to total particle volume. The field E_1 is the position-dependent complex vector fields in the core and E_0 is the field far from the particle.

It is clear from Eqs.32-37 that the magnitude of the electric field in the interior and vicinity of the particle can be substantially enhanced compared with the field far from the

particle when a resonance condition in the denominator is satisfied. Analogous to Eq.6-13, the condition for surface-plasmon resonance for the composite sphere is

$$\text{Re}(\epsilon_2 \epsilon_a + 2 \epsilon_3 \epsilon_b) = 0 \quad [6-41]$$

which leaves imaginary part $\text{Im}(\epsilon_2 \epsilon_a + 2 \epsilon_3 \epsilon_b)$ as a residual. Thus, the field enhancement at the surface-plasmon resonance of the composites can be written as

$$E_1 = \frac{9 \epsilon_2 \epsilon_3}{\epsilon_1 [3 \epsilon_2 - 2 P(\epsilon_2 - \epsilon_3)]} E_0 = f(\omega_{sp}) E_0 \quad [6-42]$$

The complex dielectric function of the Ag cluster at the surface-plasmon resonance was obtained from the reference [154] which take into account the mean-free-path effect. Only metallic permittivity is considered as a complex function in the calculations.

The dielectric permittivity and the nonlinear polarization of the inhomogeneous composites are related through

$$D = \tilde{\epsilon}(E)E = \epsilon_0 E + P(E) \quad [6-43]$$

$$P(E) = \epsilon_0 \chi^1 E + \epsilon_0 \chi^2 E^2 + \epsilon_0 \chi^3 E^3 \quad [6-44]$$

$$\tilde{\epsilon}(E) = \epsilon_0 + \epsilon_0 \chi^1 + \epsilon_0 \chi^2 E + \epsilon_0 \chi^3 E^2 \quad [6-45]$$

In which the $\chi^{(1)}$ represent the effective linear susceptibility and $\chi^{(2)}$ and $\chi^{(3)}$ represent nonlinear susceptibilities of the inhomogeneous system. The polarization and the permittivity can be further expressed in terms of their linear and nonlinear parts by,

$$P_{NL} = \delta \tilde{\epsilon}(E)E \quad [6-46]$$

$$\delta \tilde{\epsilon}(E) = \epsilon_0 \chi^2 E + \epsilon_0 \chi^3 E^2 \quad [6-47]$$

where P_{NL} is the nonlinear polarization and $\delta \tilde{\epsilon}(E)$ represent the field-dependent perturbation of permittivity in the homogeneous continuum. For centro-symmetric materials $\chi^2=0$. If the $\delta \tilde{\epsilon}(E)$ is now considered as a function of the material composition

variables, where the subscripts $q = 1, 2, 3$ refer to the core, shell, and medium regions, respectively, of the composite, then

$$\delta\bar{\epsilon}(E) = \sum_q \frac{\partial\bar{\epsilon}}{\partial\epsilon_q} \delta\epsilon_q \quad [6-48]$$

and

$$\delta\epsilon_q = \epsilon_0 \chi_q^{(3)} E_q^2 \quad [6-49]$$

where the $\chi_q^{(3)}$ and the E_q are, respectively, the nonlinear susceptibility and localized fields. The equations [6-46], [6-48], and [6-49] are combined to give

$$P_{NL} = \epsilon_0 \sum_q \bar{f}_{1q}^2 \bar{f}_3 f_{2q} \chi_q^{(3)} E_0^3 \quad [6-50]$$

where the local-field factors f_{1q} , the three concentration-dependent partial derivative factors f_{2q} , and the factor \bar{f}_3 used to define the equivalent homogeneous field \bar{E} are given relative to E_0 far from the particle by

$$E_q = f_{1q}(r) E_0 \quad [6-51]$$

$$f_{2q} = \frac{\partial\bar{\epsilon}}{\partial\epsilon_q} \quad [6-52]$$

$$\bar{E} = \bar{f}_3 E_0 \quad [6-53]$$

The nonlinear polarization can be further expressed as

$$P_{NL} = \epsilon_0 \sum_q \bar{f}_{1q}^2 \bar{f}_3 f_{2q} \chi_q^{(3)} E_f E_b E_p^* \quad [6-54]$$

$$P_{NL} = \epsilon_0 \chi_{eff}^{(3)} E_f E_b E_p^* \quad [6-55]$$

$$f_{4q} = \bar{f}_{1q}^2 f_{2q} \bar{f}_3 \chi_q^3 \quad [6-56]$$

$$\chi_{eff}^{(3)} = \sum_q f_{4q} \chi_q^{(3)} \quad [6-57]$$

The $\chi_{Ag}^{(3)}$ is obtained from Hache's work [146].

In the electrostrictive mechanism (ESM) a microparticle suspension subjected to a gradient in the electromagnetic field and develops an electrostrictive forces, given by [30]

$$\chi_{eff}^{(3)} = \frac{12\pi\epsilon_3}{k_b T} \rho r_2^3 \left(\frac{\epsilon_2\epsilon_a - \epsilon_3\epsilon_b}{\epsilon_2\epsilon_a + \epsilon_3\epsilon_b} \right)^2 \quad [6-32]$$

where ρ is the volume fraction of nano-composite particles. Thus the increase in the polarizability of the composite particle at the surface-plasmon resonance will result in a substantial increase in the $\chi_{eff}^{(3)}$. The calculations according to the electron mechanism and electrostrictive mechanism are listed in the Table 6-1.

Table 6-1. Comparison of the experimental results with the theoretical calculations.

Sample	$r1/r2$	$f(\omega_{sp})$	$\chi_c^{(3)}(\text{esu})$	$\chi_{eff}^{(3)}(\text{ESM})$	$\chi_{eff}^{(3)}(\text{EM})$	$\chi_{Ag}^{(3)}(\text{Ag})$ [146]
a($r_1 \approx 9$ nm)	0.8	1.067	1.15×10^{-6}	3.35×10^{-6}	5.4×10^{-7}	3.0×10^{-8}
b($r_1 \approx 9$ nm)	0.37	1.146	3.26×10^{-6}	5.98×10^{-6}	7.8×10^{-7}	3.0×10^{-8}
c($r_1 \approx 9$ nm)	0.28	1.769	5.73×10^{-6}	7.63×10^{-6}	9×10^{-7}	3.0×10^{-8}

In comparison with that of the pure metal colloids the large enhanced $\chi_c^{(3)}$ has been experimentally observed, specially in the case of fine-grating configuration where the flocculation of the particles density due to thermal gradient and Browning motion is minimized. It is believed that the large nonlinear response of the nano-composites is attributed to the local field enhancement as a result of the composite structure. It was found that the $\chi_c^{(3)}$ increase slightly as the layer thickness increases with the surface-plasmon resonance frequency also increasing slightly.

6.5. Conclusions

Optical characterization and theoretical calculations were conducted on the nano-composite particle having a metallic core and dielectric shell. Two essential features of the nano-composites have been revealed. First of all, in comparison with Ag colloid the two order of magnitude increase of the conjugate signals have been observed because the electric-field can be concentrated in the interior of the particle and further magnified at the surface-plasmon resonance. Secondly, for the nano-composite structure with metallic core, a limited range of resonance tunability has been observed. The experimental results provide support of the theoretical prediction proposed by Neeves and Birnboim [30]. These composite materials have potential applications to phase-conjugate mirrors, thresholding devices, and nonlinear waveguides.

CHAPTER 7 CONCLUSIONS AND SUGGESTIONS FOR FUTURE WORK

7.1. Overall Conclusions

A novel method using lamellar bilayer structures to synthesize nanometer-size, anisotropic particles has been developed in the current research. Rather than anisotropic growth by inhibition or promotion of a specific crystal plane, growth of anisotropic particles occurs in lamellar bilayer phase constructed by alternating layers of aqueous and amphiphilic molecules which provide an anisotropic microreaction chamber which confine the particle growth in the specific directions. From this method various anisotropic particles including metal oxide and semiconductor have been synthesized to evaluate the feasibility of lamellar bilayer structures as a new route for preparation of anisotropic particles. For example, nanometer-size anisotropic CdS particles have been prepared at ambient temperatures. SEM and TEM characterization shows that the resulting particles have a large aspect ratios, well-defined hexagonal geometry, and narrow size distribution.

The anisotropic growth is further ensured by selecting the organic ligand which has a strong chemical affinity with reagent species. The experimental results indicate that the reagent species (ions) chemically or physically bound onto the layer of hydrophilic groups of amphiphilic molecules provide a nucleation plane, which is essential to promote the anisotropic growth. The selection of amphiphilic systems, reagents, and preparation sequences have also a great influence on the resulting particles yield, and reproducibility.

A novel method to fabricate nanometer-sized composite particles constructed with semiconductor or metal/oxide, core-shell structure, has been developed in the current research. Based on the microemulsion technique, organometallic precursors were hydrolyzed in a microemulsion matrix. Due to low electronegativity of the metal ions of

organometallic molecules the metal alkoxide precursors initially distributed in an apolar phase of the microemulsion are subjected to a hydrolysis reaction with free water inside a reverse micelle and coated onto the surface of the core particles, followed by condensation to form the composite structure. Various materials including semiconductor (CdS) and metals (Ag, Cu) and different metal alkoxide (tetraethoxysilane, titanium isopropoxide) precursors have been used to demonstrate the feasibility of this novel method. The nano-composite particles derived from this technique have a well-defined core-shell structure and a narrow size distribution.

The mechanism of the nano-composite formation has been proposed. Among various experimental parameters the ratio of water to surfactant, R , has the most significant influence on the size and size distribution of the resulting nano-composites by governing the size distribution and stability of the micelles and kinetics of the reactions. In the low R region, the microemulsion has high stability and micelles have a small size and a narrow size distribution. The more water bound to the hydrophilic head of amphiphilic molecules inside reverse micelles, the smaller the hydrolysis rate of the metal alkoxide due to less available free water. The kinetics of the micellar interaction in the low R region is governed by inter-micellar interactions. The growth of the oxide layer is proceeded by monomer addition. As a result, near monodispersed nano-composites have been obtained in the case of low R . As R increases, the hydrolysis rate increases due to more free water available inside the reverse micelles with the rate of hydrolysis governed by intra-micellar exchange. The stability of the microemulsion decreases and the size distribution broadens. In this region the growth of the oxide favors intra-micellar aggregation. Consequently, the resulting nano-composite particles show a large size distribution.

Strong excitonic transitions of CdS clusters have been revealed from the absorption spectra as a result of quantum confinement. The energy of the first excitonic transition shifts to a high energy region as the cluster size decreases. Utilizing the temporal nucleation and growth method developed during the course of this work allows one to

precipitate CdS quantum dots with well defined crystallinity, which is essential for optical characterizations and device applications. Photoluminescence spectra of the clusters give a further evidence of the discrete energy state of the clusters, resulting from the size-quantization effects. The comparison of the experimental results of the blue shift as a function of the cluster size with the theoretical calculations of effective-mass approximation and tight-binding approximation demonstrate both the advantages and limitations of each theory. In the strong confinement region with a small cluster size, results from the tight-binding approximation are in fairly good agreement with the experimental results. On the other hand, the effective-mass approximation shows it is effective in the weak confinement region at larger cluster sizes. In addition, increasing intensity of the absorption spectra and photoluminescence spectra of the nano-composites indicate that the oxide (SiO_2) passivate the surface states of the clusters and prevent electron tunneling from the surface by a high potential barrier.

Linear optical absorption spectra of Ag/ SiO_2 nano-composites show the surface-plasmon resonance damping and red shift due to chemical absorption of the oxide onto the metal clusters, which have been addressed by several other authors. Nonlinear optical characterization of the enhanced third-order optical susceptibility of the nano-composites was conducted by degenerate-four-wave mixing (DFWM). It is believed that there is only few experimental effort in our knowledge to develop this new composite structure having been predicted by the theory and the experimentally compared with the theoretical prediction. In comparison with metal clusters, the experimental results extracted from the conjugate beam show a large increase of the third-order nonlinear susceptibility of the nano-composites due to both the local field enhancement and the quantum size effect.

7.2 Future Work

In the currently developed synthesis procedure, it is believed that the anisotropic growth in the lamellar bilayer phase is mainly due to both geometrical constraint and the

chemical affinity between the hydrophilic groups of amphiphilic molecules and reagent ions. However, to support this hypothesis and provide a general understanding of the formation mechanism, the exact chemical behavior throughout anisotropic formation should be carefully examined. First of all, the structure of the lamellar bilayer and its stability in the presence of a variety of ionic species should be examined by small-angle X-ray or nuclei-magnetic resonance spectroscopy (NMR). In particular, the interaction between organic ligand and ionic species must be evaluated by using NMR. The question as to how the interaction strength and the concentrations of individual reagent affect the lamellar phase stability needs to be addressed in future studies. Secondly, it is necessary to determine the growth mechanism inside the lamellar bilayer structure and thus, to achieve anisotropic growth in a more controllable manner.

Regarding the current success for making nanometer-size composite particles, full understanding of the exact mechanism is just beginning. In order to control the hydrolysis and condensation of organometallic precursors, the influence of the local chemical environment inside micelles must be investigated. Currently, there is no techniques available to give reliable results. Absorption spectroscopy can be used to monitor the reaction processes, but a new technique which can give quantitative results must be developed in order to examine the exact chemical behavior of the precursors inside micelles.

Currently, nano-composites of several different materials have been synthesized including CdS/SiO₂, Ag/SiO₂, and Cu/SiO₂. To fully exploit this new synthesis technique in practical applications, synthesis of new materials (other semiconductors and metals) and new composite structures (i.e. semiconductor/metal or semiconductor/insulator/metal nano-composites) should be conducted and the sintering behavior of the nano-composite particles and films should be examined. The results obtained in microemulsion synthesis of nano-composites with other oxide surface modification such as titanium isopropoxide by hydrolysis of alkoxide have shown that the control of particle size, size distribution and

especially particle aggregation is much more difficult than with the slow-reacting silicon alkoxide. Thus, of special interest is unraveling the mechanistic details of how hydrolysis and condensation reactions of metal alkoxides proceed in these media in order to have condensation and particle growth in a controlled manner, and furthermore, to have different final products such as organic-inorganic hybrid gel which may be applied to the biomedical and photochemical applications.

Size-quantization effects on optical properties should be further examined with new materials and new composite structures in order to evaluate the practical importance of these nano-composites and to verify theoretical predictions. Of special interest is investigating the electronic transportation properties of these three-dimensional quantum-wells and the influence of the interfacial state existed between each layer on optical properties. Ultrafast optical spectroscopy is a powerful tool for examining these quantum-size effects. With limited experiments, current results show enhanced nonlinear optical susceptibilities of the nano-composites due to local-field enhancement at the surface-plasmon resonance of nano-composites and quantum size effects of nanometer-size particle. However, some of the features associated with these nano-composite structures have not been revealed. Tuning the surface-plasmon resonance by changing the oxide layer thickness needs to be examined, which has very important practical applications in the area of optical communications.

LIST OF REFERENCES

1. George M. Whitesides, John P. Mathias and Christopher T. Seto, Science, **254**, 1312 (1991).
2. A. Mews, A. Eychmuller, M. Giersig, D. Schooss and H. Weller, J. Phys. Chem., **98**, 934 (1994)
3. M. F. Jarrold, and E. C. Honea, Phys. Rev. Lett., **69**, 1823 (1992)
4. Y. M. Tricot and J. H. Fendler, J. Phys. Chem., **90**, 3369 (1986)
5. T. Vossmeier, L. Katsikas, M. Giersig, I. G. Popovic, K. Diesner, A. Chemseddine, A. Eychmuller and H. Weller, J. Phys. Chem., **98**, 7665 (1994)
6. C. H. Fisher, H. Weller, L. Katsikas, and A. Henglein, Langmuir, **5**, 429 (1993).
7. A. Eychmuller, L. Katsikas, and L. Weller, Langmuir, **6**, 1605 (1990)
8. A. Cheseddline, and H. Weller, Bert. Bunsen-Ges. Phys. Chem., **97**, 636 (1993)
9. Gerald Bastard, Wave Mechanics Applied to Semiconductor Heterostructures, John Wiley & Sons, Inc., New York, 1988.
10. D. S. Chemla, Physics Today, June 1993.
11. R. F. Milligan and G. A. Thomas, The Metal-Insulator Transition, Ann. Rev. Phys. Chem., **36**, 139 (1985).
12. Wang Ying, J. Phys. Chem., **95**[3], 1119 (1991).
13. S. Schmitt-Rink, D. A. B. Miller and D. S. Chemla, The American Physical Society, **35**[15], 8113 (1987).
14. A. D. Yoffe, Advances in Physics, **42**[2], 173-266 (1993).
15. Tim Appenzeller, Science, **254**, 1300(1991).
16. Y. Kayanum, Solid State Comm., **59**, 405 (1988).
17. J. B. Xia, Phys. Rev. B., **40**, 8500 (1989).
18. Rama Krishna, and R. A. Frisener, J. Chem. Phys., **95**, 8309 (1991).
19. C. Weisbuch, and B. Vinter, Quantum Semiconductor structures, Academic Press, Inc., New York, NY, 1991.

20. J. Faist, F. Capasso, D. L. Sivco, C. Sirtori, A. L. Hutchinson and A. Y. Cho, Science, **264**, 1553 (1994).
21. V. W. S. Chan, All-optical Neetworks, Scientific American, September 1995.
22. K. Hess and G. J. Iatrate, Advanced Technology/Devices, July, 44 (1992).
23. B. G. Potter Jr., and J. H. Simmons, Phys. Rev. B., **37**, 10838 (1988).
24. D. S. Chemla, Highlights in Condensed Matter Physics and Future Prospects, Plenum Press, New York, 293 (1991).
25. A. Yariv, Introduction to Optical Electronics, Holt, Rinehardt, Winston series, 1976.
26. B. E. A. Salech, and M. C. Teich, Fundamentals of Photonics, John Wiley & Sons, Inc., New York, 1991.
27. Shaul Mukamel, Principle of Nonlinear Optical Spectroscopy, Oxford University Press, New York, Oxford, 1995.
28. D. Ricard, Ph. Roussignol, and Chr. Flytzanis, Optics Letters, **10**[10], 511(1985).
29. A. P. van Gelder, J. Holvast, J. H. Stoelinga and P. Wyder, J. Phys., **5**, 2757 (1906).
30. A. E. Neeves and Meyer H. Birnboim, Optics Letters, **13**[12], 1087 (1988).
31. J. W. Haus, H. S. Zhou, S. Takami, M. Hirasawa, I. Honma, and H. Komiyama, J. Appl. Phys., **73**, 1043 (1993).
32. G. D. Stucky and J. E. Mac Dougall, Science, **24**, 669 (1990).
33. H. Haug and S. Schmitt-Rink, J. Opt. Soc. Am. B., **2**[7], 1135 (1985).
34. Eiichi Hanamura, Scientific American, 203 (1993).
35. M. A. Reed, Quantum Dots, Scientific American, January, 118,(1993).
36. J. Caro, G. Finger, J. Kornatowski, J. R. Mendau, L. Werner, B. Zibrowius, Adv. Mater., **4**, 273 (1992).
37. M. L. Steigerwald, and L. E. Brus, Acc. Chem. Res., **23**, 183 (1990).
38. Y. Sasaki, and C. Horie, Phys. Rev. B., **47**, 3811 (1993).
39. V. S. Gurin, and M. V. Artemyev, J. Crystal Growth, **138**, 993 (1994).
40. T. Tokizaki, H. Akiyama, M. Takaya, and A Nakamura, J. Cryst. Growth, **117**, 603 (1992).
41. G. A. Ozin, and S. Ozkar, Chem. Mater., **4**, 551 (1992).
42. Hyeong-Chan Youn, Subhash Baral, and J. H. Fendler, J. Phys. Chem., **92**, 6320 (1988).

43. D. J. Schoberg, F. Grieser, D. N. Furlong, J. Chem. Soc., Chem. Commun., 515 (1991).
44. Geoffrey A. Ozin, Adv. Mater., 4[10], 612 (1992).
45. G. D. Stucky, and J. E. MacDougall, Science, **247**, 669 (1987).
46. A. Eychmuller, and H. Weller, Langmuir, **6**, 1605 (1990).
47. Y. Kobayashi, S. Yamazawa, T. Miyakawa and H. Kawaguchi, J. Sci. Mater. Electron., **3**, 20 (1992)
48. Y. Maeda, N. Tausamoto, Y. Yazawa, Y. Kanemitsu and Y. Masumoto, Appl. Phys. Lett., **59**, 3168 (1989).
49. S. Xu, X. K. Zhao, and J. H. Fendler, J. Phys. Chem., **94**, 2043 (1990).
50. I. Moriguchi, I. Tanaka, Y. Teraoka, and S. Kagawa, J. Chem. Soc. Chem. Commun., 1401 (1991).
51. X. K. Zhao, and J. H. Fendler, Chem. Mater., **3**, 168 (1991).
52. T. Li, T. Kido, and J. H. Adair, submitte to Nature.
53. G. M. Chow, M. A. Markowitz and A. Singh, IOM, Nov. 62 (1993).
54. J. H. Fendler, Chem. Rev., **87**, 877 (1987).
55. M. P. Pileni, J. Phys. Chem., **97**, 6961 (1993).
56. K. Osseo-Asare and F. J. Arriagada, Ceram. Trans., **12**, 3 (1990).
57. M. Haruta and B. Delmon, J. Chimie Physique, **83**, 859 (1989).
58. Takayuki Hirai, Hiroshi Sato, and Isao Komasaawa, Ind. Eng. Res., **32**, 3014 (1993).
59. B. H. Robinson, Nature, **320**, 309 (1986).
60. M. Meyer, C. Wallberg, and J. H. Fendler, Chem. Soc. Chem. Commun., 90 (1984).
61. E. W. Kaler, Langmuir, 4[4], 806 (1988).
62. M. L. Steigerwald, A. P. Alivisatos, J. M. Gibson, T. D. Harris, and L. E. Brus, J. Am. Chem. Soc., **110**, 3046 (1988).
63. Song-yuan Chang, Lei Liu, and Sanford A. Asher, J. Am. Chem. Soc., **116**, 739 (1994).
64. A. R. Kortan, R. Hull, R. L. Opilia, M. G. Bawendi, M. L. Steigerwald, P. J. Carroll, and L. E. Brus, J. Am. Chem. Soc., **112**, 327-1332 (1990).
65. R. P. Giannelis, J. Mater., March, 28 (1991).

66. H. Nakabayashi, M. Doi, M. Matsui, and M. Doyama, **286**, p. 227, in Nanophases and Nanocomposite Materials, eds. Sridhar Komarneini, J. C. Parker, G. J. Thomas, Materials Research Society, Pittsburgh, PA, 1993.
67. T. Li, T. Kido, and J. H. Adair, p. 791, in Proceeding of the Ninth IEEE, ISAF, University Park, PA, 1994.
68. Egon Matijevic, **60**, 1479, in Pure & Appl. Chem., Printed in Great Britain, 1988.
69. Egon Matijevic, Ann. Res. Mater. Sci., **15**, 483 (1985).
70. S. Hamada, E. Matijevic, J. Colloid Interface Sci., **84**, 274 (1981).
71. T. Sugimoto, Adv. Colloid Interface Sci., **28**, 65 (1987).
72. D. Langevin, Micelles and Microemulsions, Annu. Res. Phys. Chem., **43**, 341 (1992).
73. J. N. Israelachvili, Intermolecular and Surface Forces, Academic Press, London, 1992.
74. D. F. Evans, Langmuir, **4**, 3 (1988).
75. K. D. Daskalakis and George R. Heiz, Environ. Sci. Technol., **26**, 2462 (1992).
76. K. R. Wormuth and E. W. Kaler, J. Am. Chem. Soc., **91**, 611 (1987).
77. P. Ekwall, Advances in Liquid Crystal, **1**, 136 (1975).
78. Di Biasio, C. Cametti, P. Codastefano, P. Tartaglia, J. Rouch, and S.H. Chen in: Progr Colloid Polym Sci , **93**, 190 (1993)
79. Th. van den Boomgaard, Sh. M. Zourab, and J. Lyklema, Progr. Colloid & Polymer Sci., **68**, 25 (1983).
80. K. Shinoda, Progr. Colloid & Polymer Sci., **68**, 1 (1983).
81. Sidhar Komarneni, J. C. Parker, G. J. Thomas, Nanophase and Nanocomposite Materials, Materials Research Society Symposium Proceedings Vol **286**, 1992.
82. J G. Darab, D. M. Pfund, J. L. Fulton, and J. C. Linehan, Langmuir, **10**, 135 (1994).
83. C. Oldfield, J. Chem. Soc. Faraday Trans., **87**[16], 2607 (1991).
84. H. Hauser, p. 37, in Reverse Micelles, eds. P. L. Luisi, and B. E. Straub 1984.
85. F. Candau, Z. Zekhnini, and J. P. Durand, J. Colloid Interface Sci., **114**, 398 (1986).
86. N. Tushima, T. Takahasshi, and H. Hirai, Chem. Lett., 35 (1986).
87. Suhas, Bhandarkar and Arijit Bose, J. Colloid and Interface Sci., **135**, 531 (1990).

88. H. Yamauchi, T. Ishikawa and S. Kondo, Colloids and Surfaces, **37**, 71 (1989).
89. K. Osseo-Asare, and F. J. Arriagada, J. Colloids and Surface Sci., **50**, 321 (1990).
90. T. Hirai, H. Sato, and I. Komasaawa, Ind. Eng. Chem. Res., **33**, 3262 (1994).
91. C. B. Murray, D. J. Norris, and M. G. Bawendi, J. Am. Chem. Soc., **115**, 8706 (1993).
92. H. Weller, H. M. Schmidt, U. Koch, A. Fojtik, S. Baral, A. Henglein, W. Kunath, K. Weiss, and E. Dieman, Chem. Phys. Lett., **124**[6], 557 (1986).
93. N. Herron, and Y. Wang, and H. Eckert, J. Am. Chem. Soc., **112**, 1322 (1990).
94. R. C. Sharma, and Y. A. Chang, J. Electrochem. Soc., **136**, 1536 (1998).
95. W. Stober, and A. Fink, J. Colloid and Interface Sci., **26**, 62 (1968).
96. P. D. I. Fletcher, A. M. Howe and B. H. Robinson, J. Chem. Soc., Faraday Trans., **83**, 985 (1987).
97. John Burgess, Ions in Solution: Basic Principles of Chemical Interactions, John Wiley & Sons, New York, 1988.
98. J. Livage, M. Henry and C. Sanchez, Prog. Solid St. Chem., **18**, 256 (1988).
99. D. C. Bradley, R. C. Mehrotra and D. P. Gaur, Metal Alkoxides, Academic Press, London (1978).
100. J. Livage, Better Ceramic Through Chemistry, eds. C. J. Brinker, D. E. Clark, and D. R. Ulrich, Mater. Res. Soc. Symp. Proc. , 73, M. R. S. , Pittsburg (1986).
101. C. Sanchez, J. Livage, M. Henry, and F. Babonneau, J. Non-Cryat. Solids, **100**, 65 (1988).
102. Al. L. Efros, and A. L. Efros, Soviet Phys. Semicon., **16**, 772 (1982).
103. L. E. Brus, Appl. Phys. A., **53**, 465 (1991).
104. J. M. Luttinger, Phys. Rev. B., **102**, 1030 (1956).
105. P. E. Lippens and M. Lannoo, Phys. Rev. B., **39**, 10935 (1989).
106. Y. Kayanuma, Phys. Rev. B., **38**, 9797 (1988).
107. P. E. Lippens and M. Lannoo, Semicond. Sci. Technol., **6**, A157 (1991).
108. Fhenneberger, J Puls, Ch. Spiegelberg, A. Schulzgen, H. Rossman, V. Jungnickel and A. I. Ekimov, Semicond. Sci. Technol., **6**, A41 (1991).
109. N. F. Borrelli, D. W. Hall, H. J. Holland, and D. W. Smith, J. Appl. Phys., **61**, 15 (1987).

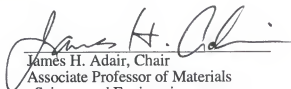
110. T. Rajh, M. I. Vucemilovic, N. M. Dimitrijevic, I. O. Micic, A. J. Nozik, J. Chem. Phys. Lett., **143**, 305 (1988).
111. A. E. Hughes, Advances in Physics, **28**[6], 717 (1979).
112. W. P. Halperin, Reviews of Modern Physics, **58**[3], 533 (1986).
113. K. P. Charle, W. Schulze, Ber. Bunsenges. Phys. Chem., **88**, 350 (1984).
114. U. Kreibig, J. Phys. F: Metal Phys., **4**, 999 (1974).
115. J. W. Haus and N. Kalyaniwalla, J. Appl. Phys., **65**[4], 1420 (1989).
116. A. E. Neeves and M. H. Birnboim, J. Opt. Soc. Am. B., **6**[4], 787 (1989).
117. J. W. Haus, H. S. Zhou, S. Takami, M. Hirasawa, I. Honma, and H. Komiyama, J. Appl. Phys., **73**, 1043 (1993).
118. G. Frens and J. Th. G. Overbeek, Z. Z. Polm., **233**, 922 (1969).
119. R. Zsibmondy, Z. Phys. Chem., **56**, 65 (1906).
120. R. M. Wilenzick, D. C. Russell, R. H. Morriss, and S. W. Marshall, J. Chem. Phys., **47**, 533 (1967).
121. T. Uchijima, M. Herrman, Y. Inoue, R. L. Burwell, Jr., J. B. Butt, and J. B. Cohen, J. Catal., **50**, 464 (1977).
122. S. Ladas, R. A. Dalla Betta, and M. Boudart, J. Catal., **53**, 356 (1978).
123. C. Petit, P. Lixon, and M. P. Pileni, J. Phys. Chem., **97**, 12974 (1993).
124. K. Shinoda, and B. Lindman, Langmuir, **3**[2], 135 (1987).
125. K. Shinaoda, Progr. Colloid & Polymer Sci., **68**, 8 (1983).
126. R. L. Scheaffer and J. T. McClave, Proability and Statistics for Engineer, PWS-KENT, Boston, MA, 1990
127. G. B. Alexander and R. K. Iler, The Chemistry of Silica, Wiley, New York, 1979.
128. I. L. Aksay, Ceramic Powder Science II, Vol. 1. part B, American Ceramic Society, 633 (1988).
129. C. Guizard, M. Stitou, A. Larbot, L. Cot, and J. Bouviere, Better Ceramics Through Chemistry, eds. C. J. Brinker, D. E. Clark, and D. R. Ulrich, Mater. Res. Soc. Symp. Proc., **121**, 317(1988).
130. S. Schmitt-Rink, D. A. B. Miller and D. S. Chemla, Phys. Rev. B., **35**[15], 8113 (1987).
131. R. W. Boyd, Nonlinear Optics, Academic Press, New York, 1982.
132. Y. R. Shen, Principle of Nonlinear Optics, John Wiley & Sons, New York, 1984.

133. H. M. Gibbs, Optical Bistability, Academic Press, New York, 1987.
134. P. N. Prasad, and D. J. Wallams, Introduction to Nonlinear Optical Effects in Molecules and Polymers, John Wiley & Sons, New York, 1991.
135. V. S. Willams, J. Mod. Optics, **35**, 1979 (1988).
136. G. Mie, Ann. Phys, **25**, 377 (1908).
137. M. A. Smithhard, Solid State Commun., **14**, 411 (1974).
138. A. Kawabata, R. Kubo, J. Phys. Soc. Jap., **25**, 1679 (1968).
139. K. P. Charle, F. Frank and W. Schulze, Ber. Bunsenges. Phys. Chem., **88**, 350 (1984).
140. J. A. A. J. Perenboom and P. Wyder, Physics Reports, **78**[2], 175 (1981).
141. M. A. Smithhard, and A. W. Tran, Solid State Commun., **14**, 407 (1974).
142. J. D. Ganiere, R. Rechsteiner and M. A. Smithhard, Solid State Commun., **16**, 133 (1975).
143. L. Genzel, T. P. Martin, and U. Kreibig, Z. Phys. B., **21**, 339 (1975).
144. F. Hache, D. Ricard, C. Flytzanis and U. Kreibig, Appl. Phys. A., **47**, 347 (1988).
145. A. Henglein, J. Phys. Chem., **97**, 5457 (1993).
146. P. Mulvaney, Langmuir, **12**, 788 (1996).
147. P. Mulvaney, T. Linnert, and A. Henglein, J. Phys. Chem., **95**, 7843 (1991).
148. F. Hache, D. Ricard, and C. Flytzanis, J. Opt. Soc. Am. B., **3**[12], 1674 (1988).
149. L. Genzel, and T. P. Martin, Surface Science, **34**, 33 (1973).
150. R. W. Schoenlein, W. Z. Lin, J. G. Fujimoto, and G. L. Eesley, Phys. Rev. Lett., **58**, 1680 (1987).
151. D. M. Pepper and A. Yariv, p. 36, in Optical Phase Conjugation, ed. R. A. Fisher, Academic Press, New York, 1983.
152. W. Kaiser, Ultrashort Laser Pulses and Applications, Springer-Verlag, Topics in Applied Physics, New York, 60, 1988.
153. J. L. Oudar, and Y. R. Shen, Phys. Rev., **22**, 1141 (1980).
154. P. Ye, and Y. R. Shen, Phys. Rev., **25**, 2183 (1982).
155. R. K. Jain, and R. C. Lind, J. Opt. Soc. Am., **73**, 647 (1983).
156. U. Kreibig, Z. Phys., **234**, 307 (1970).

BIOGRAPHICAL SKETCH


Tuo Li is the youngest son of Shi-Jian Li and Yiming Guo, born in August 9, 1959 in Peking, China. He attended Jilin University in Chang Chun. In May of 1982, the author graduated with a Bachelor of Science in physics from Jilin University. After graduation, he joined the Institute of Applied Physics and Chemistry in Dalian as a research assistant. In the fall of 1990, he received a Master of Science in physics at Virginia Polytechnic Institute and State University. He then began his pursuit of a doctoral degree in the Department of Materials Science and Engineering at the University of Florida in the spring of 1991. He is currently a member of American Physical Society and American Ceramic Society.

I certify that I have read this study and that in my opinion it conforms to acceptable standards of scholarly presentation and is fully adequate, in scope and quality, as a dissertation for the degree of Doctor of Philosophy.



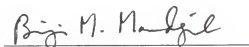
James H. Adair, Chair
Associate Professor of Materials
Science and Engineering

I certify that I have read this study and that in my opinion it conforms to acceptable standards of scholarly presentation and is fully adequate, in scope and quality, as a dissertation for the degree of Doctor of Philosophy.




Rolf E. Hummel
Professor of Materials Science and
Engineering

I certify that I have read this study and that in my opinion it conforms to acceptable standards of scholarly presentation and is fully adequate, in scope and quality, as a dissertation for the degree of Doctor of Philosophy.




Brij M. Moudgil
Professor of Materials Science and
Engineering

I certify that I have read this study and that in my opinion it conforms to acceptable standards of scholarly presentation and is fully adequate, in scope and quality, as a dissertation for the degree of Doctor of Philosophy.



Stephen Pearton
Professor of Materials Science and
Engineering

I certify that I have read this study and that in my opinion it conforms to acceptable standards of scholarly presentation and is fully adequate, in scope and quality, as a dissertation for the degree of Doctor of Philosophy.



David Reitze
Assistant Professor of Physics

This dissertation was submitted to the Graduate Faculty of the College of Engineering and to the Graduate School and was accepted as partial fulfillment of the requirements for the degree of Doctor of Philosophy.

December, 1996



Winfred M. Phillips
Dean, College of Engineering

Karen A. Holbrook
Dean, Graduate School